University of St Andrews

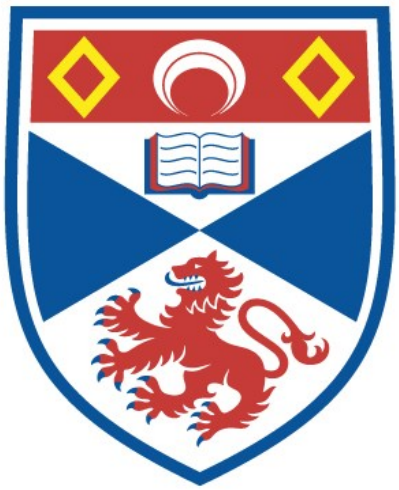

Full metadata for this thesis is available in
St Andrews Research Repository
at:
http://research-repository.st-andrews.ac.uk/

This thesis is protected by original copyright

The Fabrication of Microstructures for Ultrashort Pulse Generation in Monolithic Modelocked Semiconductor Lasers

William Whelan-Curtin
(also known as Liam O'Faolain)

Thesis submitted for the degree of Doctor of Philosophy

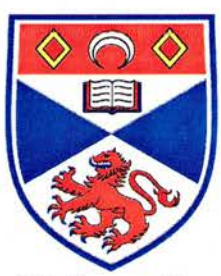

University
of
St Andrews

Th F79

for Maria

DECLARATIONS

I, William Whelan-Curtin, hereby certify that this thesis, which is approximately 50 000 words in length, has been written by me, that is the record of work carried out by me and that it has not been submitted in any previous application for a higher degree.

date 16.08.05 signature of candidate..

I was admitted as a research student in September, 2001 and as a candidate for the degree of Doctor of Philosophy in September, 2001; the higher study for which this is a record was carried out in the University of St Andrews between 2001 and 2005.

date 16.08.05 signature of candidate..

I hereby certify that the candidate has fulfilled the conditions of the Resolution and Regulations appropriate for the degree of Doctor of Philosophy in the University of St Andrews and that the candidate is ~~qualified to submit~~ this thesis in application for that degree.

date 16.08.05 signature of supervisor.

In submitting this thesis to the University of St Andrews I understand that I am giving permission for it to be made available for use in accordance with the regulations of the University Library for the time being in force, subject to any copyright vested in the work not being affected thereby. I also understand that the title and abstract will be published, and that a copy of the work may be made and supplied to any bona fide library or research worker.

date 16.08.05 signature of candidate.

ACKNOWLEDGMENTS

TO BEGIN with I would like to thank all people whose direct or/and indirect involvement helped this thesis to take place.

First of all, I am grateful to the excellent lectures of University College Cork (Ireland) for the solid base of knowledge I received during my four years of undergraduate studies there. In particular, I would like to thank Dr. Tony Deeney for setting my feet on this road.

I would like to say special and many thanks to my supervisor Prof. Thomas F. Krauss, whose ideas and useful discussions guided me through this project.

I would like to especially thank the following people, who made essential contributions to this work:

Maria Kotlyar,
Donald Brown,
Michael Flynn,
Maria Ana Cataluna,
and Rab Wilson.

I would also like to thank Lijun Wu, Simon Cran-McGreehin, Stephen Moore, Iain Cormack, Ben Agate, Andreas Vasdekis and Steve Neale for their help, assistance and suggestions.

Prof. Wilson Sibbett and Dr. Edik Rafailov helped me more than once with their useful discussions -thank you very much for your participation.

My special gratitude goes to Mr George Robb whose excellent hard-working hands kept all equipment in good working order (not to mention building a lot of it) and whose friendly company I enjoyed not once during my stay in St Andrews.

I am very grateful to my colleague Maria Kotlyar who became my wife during my time at St Andrews and whose love and care inspired along the way to this PhD degree.

Finally, I would like to say thanks to my two examiners Dr Graham Turnbull (University of St. Andrews) and Professor Richard Penty (Cambridge) for their time and effort in reading and improving this thesis.

ABSTRACT

IN RECENT YEARS much time and effort has been spent in the search for a monolithic femtosecond semiconductor laser. Such a device is very attractive for applications in telecommunications, particularly as a source for Wavelength Division Multiplexing, by virtue of its small size, compactness and ability to be electrically pumped. This thesis looks at the creation of such a device through the use of photonic crystals and microstructures.

As a prerequisite for this, Chemically Assisted Ion Beam Etching was studied and a new regime of operation developed. This allows the creation of high quality photonic crystals with low sidewall roughness. A new technique for creating silica masks was also developed. This has the advantage of being simpler, less expensive and less damaging to the material surface than previous methods.

A numerical model was developed to describe these lasers. This was then used to study Q-switched modelocking in semiconductor lasers. Guidelines were formulated to allow this regime of operation to be obtained or avoided as required.

A new type of pulsed Quantum Well laser was developed. This used sidewall recombination as the recovery mechanism for the saturable absorber. This technique is promising as this may be a quick recovery mechanism and also as the need for a second electical contact is removed.

The use of narrow deeply etched waveguides in quantum dot material was demonstrated to be practical. By virtue of their low sidewall recombination velocity, it is possible to etch through the active layer with little penalty. This allows the creation of narrow 2-3μm waveguides with high refractive index contrasts. Not only does this provide highly efficient current injection (threshold current densities were only 10 percent higher than broad area devices), the range of allowed device geometries is expanded (curved and photonic crystal waveguides).

The obstacles preventing the production of ultrashort pulses were studied with aid of this model. They were found to, chiefly, be the absence of intracavity dispersion compensation and the low pulse shortening rate of the saturable absorber.

A method of providing chirp compensation was proposed and shown to be feasible to fabricate. This feature was included into the model and shown to produce a significant pulse shortening (from 2.5ps to 1ps).

A design for a new method of modelocking was also proposed. This involved the creation of a nonlinear photonic crystal mirror through the incorporation of a nonlinear polymer. A technique was developed by which photonic crystals may be filled with polymer. This method was theoretically shown to be have very good potential for the production of ultrashort pulses.

PUBLICATIONS ARISING FROM THIS WORK

Journal Papers

1. Liam O'Faolain, Maria V. Kotlyar, Neeraj Tripathi, Rab Wilson and Thomas F. Krauss,"Fabrication of Photonic Crystals using a spin coated Hydrogen Silsesquioxane (HSQ) mask,"submitted *J. Vac. Sci. Tech. B.*

2. Liam O'Faolain, Michael Brian Flynn, Rab Wilson and Thomas F. Krauss,"A Kerr Modelocked Semiconductor Laser: Design and Theory,"*IEEE J. Select. Topics. Quant. Electron.*, vol. 10, pp.1063-1069, 2004

3. Michael B. Flynn, Liam O'Faolain and T. F. Krauss,"Chirp Compensation with FPI,"*App. Phys. Lett.*, vol. 86, pp. 221104, 2005.

4. Maria V. Kotlyar, Liam O'Faolain, A. Krysa and Thomas F. Krauss,"Electrically tunable multiquantum-well InGaAsP/InGaAsP microphotonic filter,"*IEEE Photon. Tech. Lett.*, vol. 17, pp. 837-839, (2005).

5. Michael B. Flynn, Liam O'Faolain, Rab Wilson and Thomas F. Krauss,"Kerr induced passive Q-switching of a semiconductor diode laser,"*J. Opt. Soc. Am. B*, vol. 22 ,pp. 792-795, 2005.

6. Stephen A. Moore, Liam O'Faolain, Maria Ana Cataluna, J. S. Roberts, Maria V. Kotlyar and Thomas F. Krauss,"Reduced Surface Sidewall Recombination and Diffusion in Quantum Dot Lasers,"submitted *App. Phys. Lett.*.

7. Michael B. Flynn, Liam O'Faolain and Thomas F. Krauss,"An Experimental and Numerical Study of Q-Switched Mode-Locking in Monolithic Semiconductor Diode Lasers,"*IEEE J. Quant. Electron.*, vol. 40, pp. 1008-1014, August 2004.

8. Maria V. Kotlyar, Liam O'Faolain, Rab Wilson, Thomas F. Krauss,"High aspect ratio chemically assisted ion beam etching (CAIBE) for photonic crystals using a high beam voltage-current ratio,"*J. Vac. Sci. Tech. B*, vol. 22, pp. 1788-1791 , 2004.

9. Maria V. Kotlyar, Liam O'Faolain, A. Krsa and Thomas F. Krauss,"Electro-optic tuning of InP-based microphotonic Fabry-Perot Filters,"*IEEE J. Light. Technol.*, vol. 23, pp.2169-21717, 2005.

10. Maria V. Kotlyar, Lorenzo Bolla, Michele Midrio, Liam OFaolain and Thomas F Krauss, "Compact photonic crystal polarisation rotator in InP- based material,"submitted *Opt. Expr.*.

11. Donald H. Brown, Michael B. Flynn, Liam O'Faolain and Thomas F. Krauss,"Coupled Cavity Tunable Semiconductor Diode Lasers Incorporating Multi-Layer Mirrors,"submitted*IEEE Photon. Tech. Lett.*.

12. Maria V. Kotlyar, Tim J Karle, Michael D. Settle, Liam O'Faolain and Thomas F. Krauss,"Low loss photonic crystal defect waveguides in InP," *App. Phys. Lett*, vol. 84, pp. 3588-3590, 2004.

13. Thomas F. Krauss, Maria V. Kotlyar, Liam O'Faolain and Rab Wilson,"Photonic crystal Channel Waveguides in InP," *Proc. SPIE*, Paper 5360-24, Photonics West, 2004.

Conference Papers

1. L. O' Faolain, X. Xhu and T. F. Krauss, "Lithography Limits of Photonic Crystals", presented at PEVS-VI, Crete, June 2005.

2. L. O' Faolain, S. A. Moore, Maria Ana Cataluna, J. S. Roberts, Maria V. Kotlyar, R Wilson and T. F. Krauss, "Fabrication Techniques for active Photonic Crystal devices ", presented at PEVS-VI, Crete, June 2005.

3. M. V. Kotlyar, L. O'Faolain, A. Krysa and T. F. Krauss, "Compact Multiquantum-well tunable filters in InP ", presented at PEVS-VI, Crete, June 2005.

4. S. S. Oh, M. Mazilu, L. O'Faolain, H. Y. Park and T. F. Krauss, "Efficient coupling to photonic crystal waveguides using surface plasmon waveguides", presented at PEVS-VI, Crete, June 2005.

5. M. B. Flynn, L. OFaolain and T. F. Krauss, "Passively Mode-Locked Monolithic Semiconductor Diode Lasers Incorporating Dispersion Compensation,"presented at the 17th Annual Meeting of the IEEE Lasers and Electro-Optics Society, Puerto Rico, November 2004.

6. M. B. Flynn, D. H. Brown, and T. F. Krauss, "Coupled Cavity Tunable Semiconductor Diode Lasers Incorporating Multi-Layer Mirrors,"presented at the 17th Annual Meeting of the IEEE Lasers and Electro-Optics Society, Puerto Rico, 2004.

7. Liam O'Faolain, Michael B. Flynn, Rab Wilson and Thomas F. Krauss, "A Kerr Modelocked Semiconductor Laser: Design and Theory,"presented ETOS'04, Cork, Rep of Ireland, July 2004.

8. Liam O'Faolain, Michael B. Flynn, Donald Brown and Thomas F. Krauss, "Q-Switched Modelocking of Semiconductor lasers,"presented at SIOE'04, Cardiff, Wales April 2004.

9. Thomas F. Krauss, Maria V. Kotlyar, Liam O' Faolain, Rab Wilson, Michael Settle, Tim J. Karle, Alan Bristow, A. Tahraoui, M. Fox and M. Skolnick, "Functional Photonic Crystal Waveguides and Lattices,"presented at PECS5, Tokyo, Japan 2004.

10. Donald H. Brown, Michael B. Flynn, Liam O' Faolain, Wilson Sibbett and Thomas F. Krauss, "Coupled Cavity Lasers Incorporating Bragg Mirrors,"presented at LEOS'03 Annual Meeting, Tucson Arizona, paper WL6, 2003.

THESIS OUTLINE

THIS THESIS is divided into two parts. In part one, we describe the basic theory of semiconductor lasers and of modelocking. We then go on to describe some of the basic techniques for modelling modelocked lasers and of fabricating photonic crystals and semiconductor lasers.

In the second part, new developments resulting from the work carried out in this thesis are presented. The first chapter discusses three new or advanced fabrication techniques- high beam voltage low beam current Chemically Assisted Ion Beam Etching, Hydrogen Silsesquioxane masking and polymer infilling of photonic crystals. Next, we describe the modelocking of semiconductor lasers and their characterisation. The obstacles preventing the generation of ultrashort pulses and some possible solutions are also described. We then to go on to examine Q-switched Modelocking of semiconductor lasers and advance the understanding of this behaviour.

We also look at some aspects of sidewall recombination and its importance to lasers. We use it in a new type of pulsed laser and look at its influence on quantum dot lasers. In the final chapter, we demonstrate the advantages of incorporating a nonlinear polymer into a semiconductor laser and show how this may be used to generate ultrashort pulses.

CONTENTS

1. INTRODUCTION

1.1 Goals

FEMTOSECOND laser systems have proven themselves to be very important tools in modern science, medicine and industry. They are ideally suited for time resolved measurements (Pump-probe experiments) which allow the characterisation of semiconductors and the examination of very fast chemical processes such as bond breakage and formation. Using nonlinear crystals, light in the visible and UV regions may be created. The high peak intensities resulting from the short pulses can excite many important nonlinearities allowing the charaterisation of samples in medical diagnostics . The degree of control has been useful to medicine for improved laser ablation during drilling and for high precision photopolymerisation in manufacturing. A sample femtosecond laser system is shown in figure 1.1.

1.1.1 The future

OVER THE years, not only has the number of applications grown, but the general quality of ultrashort lasers has considerably improved. The first sub 100fs pulses were produced using Colliding Pulse Modelocking in dye lasers in by Fork *et al.* [2] in 1981. The introduction of Kerr lens modelocking in solid state lasers resulted in some of the shortest pulses at the time [3]. The development of Saturable Bragg Reflectors (SBR) solved many of the stability problems associated with Kerr lens modelocking with little increase in pulse durations. A careful study of SBR modelocking led to an understanding of Q-switching instabilities thus allowing its prevention [4]. The use of high power laser diodes as the pump source led to a step forward in simplicity and efficiency.

The introduction of these features has led to a slow but steady reduction in size and complexity of this systems, culminating in a 4GHz Cr:LiSaf laser[5]. However, this appears to be very close to the ultimate limit of miniaturisation in these systems. The need for cooling of the laser diode pump systems and sometimes of the gain crystal, as well as a laser cavity with the necessary components for dispersion compensation and modelocking restricts the minimum size. Furthermore, the low gain per unit length of the crystal places a fundamental limitation on these systems.

The replacement of the current macroscopic solid state and fibre laser systems by monolithic semiconductor lasers is likely to be a very long term project. Semiconductor materials have inherently a very broad gain bandwidth, which can under some circumstances be made as broad as that of Titanium Sapphire [6]. The high Self Phase Modulation (SPM) present in semiconductors, (unavoidable, so far, in practice, despite much effort) need not

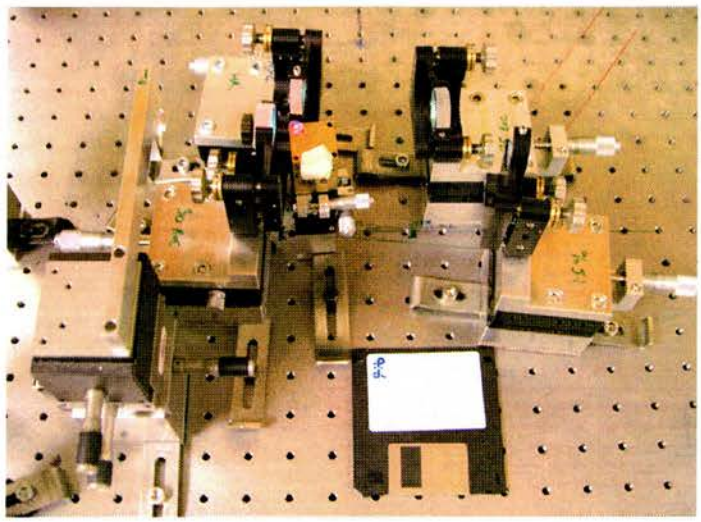

Fig. 1.1: A femtosecond Cr:LiSaf laser. A floppy disk has been included in the picture to give a sense of scale. Courtesy of Dr. Ben Agate [1].

be disadvantageous, as SPM broadens the spectral width of the pulse potentially allowing shorter pulses. The successful integration of chirp compensation and improved methods of modelocking would overcome the pulse lengthening due to SPM. In fact, careful analysis has shown that the shortest pulses occur when there is SPM in the cavity [7]. If SPM occurs, the shortest pulses can be over a factor of two shorter than a cavity in which no SPM is present.

Semiconductor lasers may be directly pumped electrically, which allows a considerable simplification relative to solid state lasers. The removal of this pumping stage between the electrical power supply and the optical output also promises improvements in efficiency and size. The cavity, by virtue of its monolithic structure, is also mechanically very stable, widening the range of potential applications.

Using Quantum dots as a gain media has additional advantages. It has been theoretically predicted that Quantum dot lasers may show temperature independent operation [8]. This is yet to be achieved, but devices exist already that show improvements relative to standard quantum well devices [9]. Also, quantum dot lasers have been shown to be more resistant to optical feedback than Quantum well devices (and much more so than macroscopic lasers) [10]. Thus, operation without either cooling or optical isolation may become possible.

The technique of Quantum well intermixing allows the creation of monolithic long (millimetres) extended passive cavities[11]. This reduces the usually high repetition rate of diode lasers with a consequent increase in pulse energy.

The accomplishment of these goals would have a considerable impact on the world of lasers. Amongst other possibilities, it could allow the creation of a femtosecond laser with a size similar to that shown in figure 1.2.

On the basis of their CW performance, monolithic semiconductor lasers are perhaps the most common and useful laser type. For instance, it was reported recently that industry may soon be be able to offer high power broad area semiconductor laser arrays at prices on

Fig. 1.2: A commericial diode laser in a 9.2mm transistor can.

the order of £1 per watt [12]. As a source of pulses, though, their potential of monolithic SC lasers is yet to be fully realised.

Ultrafast semiconductor lasers have not yet been developed to the same level of cost effectiveness and usefulness as CW semiconductor lasers. If the fantastic performance of high power semiconductor lasers can be transferred to world of ultrashort pulses without significant increase in cost, then this low price may put, for example, a femtosecond laser in every ambulance or doctor's bag.

1.1.2 Applications

ON A more down to earth level, ultrafast semiconductor lasers would find immediate application in the field of optical telecommunications [13].

The requirement by industry, commerce and the world in general, to be able to pass large amounts of information rapidly from point to point (both voice and data traffic) is leading to an increasing demand for network bandwidth. Fibre optic cables are the main method of carrying this. However, laying a fibre optic cable link is an expensive and complicated task. As a result, the telecommunications industry naturally prefers the approach of increasing the capacity of existing cable.

Time division multiplexing (TDM) has been one of the techniques employed to increase the bandwidth of a fibre optic link and has enjoyed considerable success TDM combines a number of slower signals into one fast signal. The bits of each slower signal are assigned a time slot in the faster signal.

However, the increasing speed of TDM requires faster and faster electronics (though optical means may also be employed). These, invariably, are expensive which, needless to say, is undesirable especially in the current economic climate. TDM has another disadvantage

in that it does not scale easily. The capacity increases in by a multiple (typically, a factor of four). As a result, a network can make a transition from having fractionally too little bandwidth to over just under four times more than necessary. This is inefficient and a smoothly scalable system would result in savings. Thus, it would be preferable to send a number of different, relatively slow, signals down a single fibre.

An optical fibre may carry a number of different wavelengths at one time without them interfering with another. Rather than multiplexing different signals together in the time domain, each signal is assigned an individual wavelength and transmitted down the fibre independently. This technique is known as wavelength division multiplexing (WDM) [14].

In a simple WDM system, each wavelength is provided by a different laser. Modulators then impose the desired signal and the light from each laser is combined and transmitted down the fibre. At the other end, the various wavelengths are separated and the information recovered [15].

The limitation on the bandwidth then becomes the number of different channels which fit in the low loss window of the fibre, which in turn depends on the spacing between each channel. In practice, the low loss window is large (15000 GHz) and the spacing can be made small (50 GHz), and thus the limiting factor is often the number of sources. A number of techniques may used to solve this, such as spectral slicing of a broad bandwidth source (a Light Emitting Diode, for instance). Another method is to use TDM on each wavelength.

1.1.3 Monolithic Modelocked semiconductor lasers

SEMICONDUCTOR lasers have been very attractive to the telecommunications industry for a number of reasons. Their small size, low power consumption, ease of coupling to fibre and low cost has led to their extensive use in today's telecommunication systems, usually in the form of directly modulated Distributed Feedback Reflector/Distributed Bragg Reflector lasers.

Monolithic Modelocked (MML) devices have all the above advantages with some important additions. Due to the small cavity size (typically 1mm, though sizes widely vary) high repetition rates (40 GHz[1]) are readily available without external electronics[2]. This, in fact, is sometimes a disadvantage as the electronics needed to work with the pulse train is expensive. However, through the use of longer cavities (Quantum dot devices, Quantum Well intermixing), the repetition rate may be pushed low enough to make cheaper electronic modulators, etc. practical.

For TDM systems, short pulses from the laser are very desirable allowing the use of smaller switching windows and thus a greater ultimate bit rate. This speed rapidly leaves electronics behind, requiring optical means of manipulating the signal. Thus, Monolithic Modelocked semiconductor lasers are an ideal candidate as a source for Optical Time Division Multiplexing (OTDM), in which the high repetition rate could be used to great advantage [17].

Ultrashort (subpicosecond) pulses naturally have a broad spectrum (a prerequisite, in

[1] Devices exist which can operate as fast as 2.1 THz [16].

[2] We only consider passive modelocking in this thesis, as for monolithic devices very fast modulation (at the cavity roundtrip time) is necessary for active modelocking.

fact). This naturally leads to their consideration as a multiwavelength source for WDM. A typical MML device may easily have a spectral width of 3-4nm allowing 7-10 channels at a 50 GHz spacing. However, the currently available pulse duration from such a device is longer (2-3ps) than one would expect from the simple Fourier transform relationship meaning that the pulse is highly chirped. In order for these devices to become genuinely useful, much shorter pulses are required. Furthermore, even shorter pulses have a broader spectrum increasing the number of potential channels.

The goal of this project is, therefore, to attempt to produce ultrashort pulses from a monolithic device. Economics being the chief concern in telecommunication industry today, this would make this MML semiconductor lasers, prospectively, extremely useful as a cheap source for WDM[3].

Important questions, such as temperature behaviour and jitter characteristics, would still remain, however this is beyond the scope of this thesis.

1.2 Overview

IN THE development of dye and solid state laser systems, it proved possible to incorporate advanced optical components such as dispersion compensating prisms, Gires-Tournois interferometers and saturable Bragg reflectors at a relatively early stage. This is largely a result of the macroscopic scale of their cavities. To date, as a result of its microscopic scale cavity, a monolithic semiconductor laser cavity is rarely more than a simple Fabry-Perot resonator[4]. Ultrashort pulse production in semiconductor lasers has lagged far behind, however, despite having a history comparable to that of those lasers just mentioned. The use of external cavity semiconductor laser systems has resulted in pulses comparable to other systems. However, their complexity sacrifices many of the hoped for advantages. Furthermore in terms of peak power output, it is unlikely that they will be able to compete with solid state lasers.

Figure 1.3 shows a graph of the best pulse widths achieved over time. The macroscopic laser systems all show a steady decrease with time as new techniques have been developed. Semiconductor lasers have shown an initial rapid decrease to the picosecond scale, however after this, despite a number of innovations, the rate of decrease has been painfully slow. The new techniques that brought success to dye and solid state lasers invariably involved the manipulation of and addition of elements to the laser cavity. This degree of control had been absent in monolithic semiconductor lasers until the development of Photonic Crystals over the last decade and a half. The first such use of photonic crystals was employed by Yansson *et al.* in the generation of a 2.1THz pulse train. This thesis looks further into this idea, and investigates the various possibilities and advantages of Photonic Crystal components[5]and microstructures produced by related methods.

[3] Their potential for the complementary technique of OTDM also means that their desirability will remain, should the financial climate cease to be so restrictive in the future.

[4] DBR lasers are still essentially a Fabry-Perot resonator, just with a more sophisticated mirror.

[5] A body of opinion does not consider one dimensional photonic crystals to be true photonic crystals. Strictly speaking, a 1-D Phc is of course a photonic crystal, however dielectric bragg stacks fall into this class, and it seems incorrect to consider them as such. The 1-D PhCs considered here are deeply etched semiconductor-air structures. These involve most of the fabrication and characterisation difficulties inherent

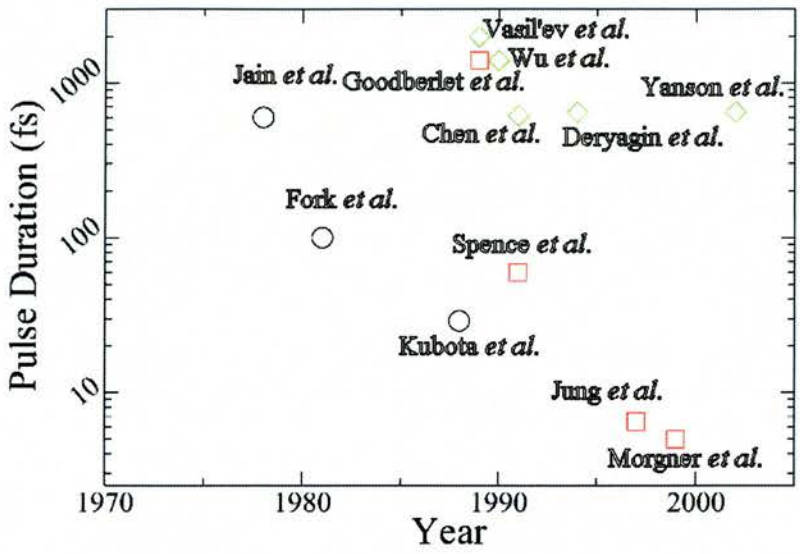

Fig. 1.3: Pulse durations of different lasers acheived using passive modelocking over time- black circles indicate dye lasers, red squares Ti:Saf and green diamonds semiconductor lasers. Note that the progress of monolithic semiconductor lasers has slowed after initial success, [18] [2] [19] [20] [3] [21] [22] [23] [24] [25] [26] and [16].

1.2.1 State of the art

IN RECENT years, much time and effort has been spent in the search for a monolithic femtosecond diode laser. Typical devices produce pulses with picosecond durations. There have been a small number of devices which have produced subpicosecond pulses, 620 fs [25] using MCPM and 650 fs [26] and 730fs [27] using hybrid modelocking.

By using external compression techniques or external cavities with intracavity chirp compensation, much shorter pulses have been demonstrated. Ludwig *et al.* have used the elegant technique of compressing pulses from a hybridly modelocked external cavity laser with dispersion compensating fibre, producing 180 fs pulses[28]. In general, pulses from a semiconductor laser are not linearly chirped and more complicated dispersion compensating techniques are necessary to approach the transform limit [29]. 200 fs pulses have been achieved using intracavity chirp compensation [30]. By using additional intracavity elements to shape the pulse spectrum, Delyfett *et al.* produced 160fs pulses [6].

The current record is held by Matsui *et al.*, who use a very complicated multi-element dispersion compensation and amplification scheme to compress pulses from a gain switched laser down to 20 fs [31].

This brief examination of ultrashort pulse production in semiconductor lasers demonstrates that there is no fundamental limit to the monolithic prodution of 100 fs pulse. The

in the classic 2-D crystal. Furthermore, for use in a single mode laser, which is one dimensional almost by definition, a 2-D PhC component offers no advantage over the 1-D case. Thus, throughout this thesis, 1-D deep etched structures are described as photonic crystals.

obstacle is simply incorporating sufficiently advanced optical elements.

1.2.2 The Problems

THE PULSE width produced by a laser is determined by the interplay between the pulse shortening mechanism and pulse lengthening effects due to group velocity dispersion and self-phase modulation (SPM) [32].

Self Phase Modulation

IN QUANTUM WELLS, the refractive index and the gain are very strongly dependent on the carrier density. Thus the refractive index and gain are very strongly coupled (described through the linewidth enhancement factor). The passage of a pulse depletes the gain and carrier density. This increases the refractive index and phase modulates the optical pulse resulting in a drop in the instantaneous frequency over the pulse. The trailing edge of the pulse thus travels at a much slower velocity stretching the pulse in time. This causes highly chirped pulses which can be many times (often 10+) the transform limit.

Also, due to intraband transitions, the gain acts like a homogeneously broadened medium which narrows the available gain bandwidth. Quantum wells have typically a gain width on the order of 20 nm (this may be extended by using a material with a range of different sized quantum well [33] and [6]. However, as a gain material for a laser this 20 nm gain width reduces to a practical gain witdh of only a few nanometers. This is due to the homogeneous nature of semiconductor gain. The 20 nm gain occurs when the bands are fully occupied and spontaneous emission takes place over the full energy range spanned by the bands. When lasing is taking place, the carriers with energies corresponding to the lasing wavelength are constantly being depleted at a high rate. On a 100 fs timescale- the intraband relaxation time, higher energy carriers in the band relax to fill the vacancies caused by this stimulated emission, attempting to restore the thermal equilibrium. This process collapses the initially broad gain width. Thus, on a timescale greater than the intraband relaxation time, a quantum well behaves as a homogeneously broadened gain medium. Interestingly, this raises the possibility that to sub-100 fs pulses a quantum well may be inhomogeneous.

As the pulse circulating in the cavity gets shorter, the effects of carrier heating and other effects such as gain dispersion become important, resulting in highly nonlinear chirping. For example, the breakup of a 650 fs pulse propagating in an SOA has been observed [34]. This indicates that the monolithic production of pulses shorter than 600-700 fs will be difficult. Azouz *et al* suggest that keeping the pulse relatively long (with a corresponding low peak intensity) in the gain medium offers advantages as this prevents intensity induced nonlinear effects. An external compressor can then be used to compress the relatively simply chirped pulses [35].

These problems have stimulated interest in Quantum Dots as a replacement for QWs in modelocked semiconductor lasers. QDs naturally have a very broad inhomogeneous gain-width as a result of the large spread of dot sizes, strains and shapes. (In fact, considerable effort has been expended in trying to reduce this spread as it is unfavourable for CW lasers). This has excited interest as an inhomogeneous broadened material is preferable for ultra-

short pulse production. Theory also suggests that QDs should have a very small line-width enhancement factor compared to quantum wells as a result of the symmetry of the gain bandwidth. Values as low as 0.5 and 0.1 have been reported, [36] [37], though values around 2 are more common.

Then again, SPM is very important to ultrafast lasers as it broadens the spectrum of the propagating pulse. Thus, in the absence of SPM, transform limited pulses with very narrow spectral width might be expected. In fact, long transform limited pulses have been observed in a quantum dot laser by Thompson *et al.*, [38]).

Furthermore, nonlinear gain dynamics are still complicated [39] which makes QDs little more favourable than QWs to subpicosecond pulses.

Despite the fact that an inhomogeneous gain medium is very attractive, the gainwidth (useful or otherwise) does not appear to be the reason behind the current difficulties in producing subpicosecond pulses. Experimental devices typically produce pulses which have time-bandwidth products many times the transform limit. Even the current homogeneously broadened quantum well devices have gain widths capable of supporting 200fs pulses, demonstrated by Futami *et al.* [40]. In fact, many of the early models of modelocked semiconductor lasers implicitly assumed an infinite gain bandwidth. In spite of this (apparently) extremely unreasonable assumption, these models have enjoyed considerable sucess in predicting and modeling the results of experimental devices.

The preferred solution is, thus, to retain the high SPM that broadens the pulse in the spectral domain but include chirp compensating elements that compress it in the time domain.

The Saturable absorber

ONE OF THE fundamental requirements for slow saturable absorber modelocking is that the absorber saturates stronger than the gain. For example, in dye lasers, this is accomplished by using a tighter focus in saturable absorber dye stream than in the gain dye [7]. At first glance, this appears impossible in monolithic semiconductor lasers. Fortunately, due to the logarithmic shape of the QW gain curve, the differential gain in a semiconductor is different above and below threshold, allowing the fulfillment of this condition. Nonetheless, this similarity causes a loss of performance in monolithic modelocked lasers.

In standard semiconductor lasers, the pulse shortening rate is limited by the recovery time of the saturable absorber, which is of the order of 5-50 ps when the recovery mechanism is an applied reverse bias [41] and 2 ps in the case of saturable absorption by ion implantation [42]. The most commonly used technique is that of the reverse biased section, however this has some additional complications. When light is absorbed in the saturable absorber generating carriers, they are swept out by the reverse bias. However, if these then remain in the vicinity of the quantum well (or dot), they screen the reverse bias reducing the effective applied voltage and increase the absorber recovery time [43]. This effect is proportional to the amount of carriers generated which will depend on the pulse energy and may increase the recovery time from 20ps to 60ps. A recent theoretical work [44] has suggested a new stepped quantum well design that greatly reduces the recovery time through an increase in the ability of carriers to escape the quantum well and active layer.

Tropper *et al* have demonstrated subpicosecond pulses in an external cavity surface emitting system [45]. This system uses the AC Stark effect in a semiconductor saturable absorber mirror (SESAM) to provide a stronger[6]than usual form of mode-locking giving the capability to produce transform-limited 620 fs pulses (shorter pulses were also produced but were not transform limited). This system, as a result of its surfacing emitting nature, avoids most of the large self-phase modulation inherent in stripe-geometry lasers, but it does indicate the possibility of overcoming the complex chirping due to carrier heating, see section 1.2.2, (at least for pulses greater than 500 fs).

Thus, increasing the effectiveness of the modelocking element seems to be a promising option in the quest for shorter pulses. If the chirping is held constant, a greater pulse shortening rate per pass will produce shorter pulses. Additionally, overcoming the very complex chirping that will occur when subpicosecond pulses propagate in the cavity is unlikely to be possible using the chirp compensating elements that may be monolithically integrated (they will not be able to match in complexity the methods possible externally, see section 1.2.1). The "brute force"approach is perhaps the only option in this situation.

1.2.3 A comparison with Macroscopic Ultrashort Lasers

A REPEATED theme in this thesis is the comparison of semiconductor lasers and solid state systems, and the attempt to use techniques which proved sucessful in solid state laser systems. We study the occurrence of Q-switched modelocking in semiconductor lasers and attempt to integrate chirp compensation elements and saturable bragg reflectors (SBR). We also investigate the possibility of introducing Kerr Modelocking to semiconductor lasers, determining the requirements necessary for a viable system.

Colliding Pulse Modelocking

THERE HAS already been considerable success in following the example of solid state and dye lasers. In 1981, the first colliding pulse modelocked laser was built by Fork *et al.* [2]. This was a dye laser with a ring cavity and produced at the time the shortest ever pulses (sub 100 fs). In the early 1990s, colliding pulse modelocking (CPM) was introduced to semiconductor lasers by Ironside *et al.* in Glasgow.

CPM has a stronger mode-locking effect than a simple two-section device due to the higher pulse intensity in the saturable absorber which increases the absorption cross section, see figure 1.4. Furthermore, as the number of pulses in the cavity has increased, particularly for the case of Multiple Colliding Pulse Modelocking (MCPM), the carrier density has less time to recover in between the passage of pulses and thus less SPM occurs. The introduction of CPM has resulted in the shortest pulses to date from a monolithic diode laser. Wu *et al* have demonstrated transform limited 1.4 ps pulses from a CPM diode[24] and Martins-Filho *et al* 1.3 ps pulses using multiple colliding pulse modelocking [46]. The shortest pulses, 620fs, from a monolithic device were produced using this method [25]. Yanson *et al* have extended this idea to very high harmonic mode-locking, demonstrating subpicosecond pulses at very

[6] Here, and later, I make use of the intuitive idea of the "strength"of the modelocking element. This may be rigorously defined as the pulse shortening rate per pass.

high repetition rates [16]. However, the extremely high repetition rate and corresponding low peak powers limit the usefulness of higher harmonic modelocking.

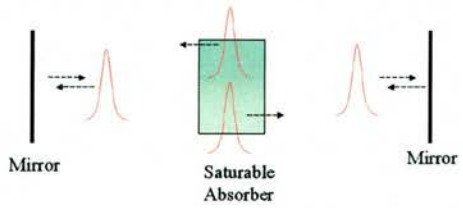

Fig. 1.4: In colliding pulse modelocking, two pulses oscillate in the cavity at the same time so as to collide in the saturable absorber. This results in twice the light intensity which strongly bleaches the absorber.

Using very high harmonic modelocking (repetition rates on the order of 1THz), a number of researchers have reported pulse durations of approximately 200-300 fs. I have excluded these results from the above discussions on the grounds that these devices are very much special cases of modelocking and pulse production[7]. Due to the high repetition rate, the pulse train usually becomes little more than a sine wave often with poor extinction between "pulses". Also, it may be considered that it is unnatural for a semiconductor laser to operate in this regime and very sophisticated techniques are required to achieve this. Thus, I feel that there are few lessons to be learned from terahertz modelocking for the ultrashort pulse production in which we are interested and justify the exclusion of these pulses from figure 1.3 etc.

Chirp Compensation

IT HAS BEEN shown that a "real" ultrafast laser (where SPM is non-zero) produces the shortest possible pulses when the net cavity dispersion is slightly negative [7]. In fact, this situation produces shorter pulses than one in which there is no SPM. Intuitively, self phase modulation broadens the spectral width of the pulse allowing shorter pulses but requiring a negative net cavity dispersion to counteract the lengthening due to the SPM induced chirp.

In order to compensate for Self Phase modulation and positive material dispersions in macroscopic lasers, various methods such as sets of prisms, see figure 1.5 [47], grating pairs [48], chirped dielectric mirrors[49] and dielectric Gires-Tournois interferometers, [50], were developed. Virtually all modern ultrafast lasers make use of one or more of these techniques in order to produce the shortest possible pulses.

These have also been applied sucessfully to external cavity semiconductor lasers [51]. Delyfett *et al.* have used a four prism chirp compensating set to produce 200 fs pulses [30].

The monolithic integation of such systems is difficult. De la Rue *et al.* have proposed a shallow etched chirped DBR to compress pulses. However, in an active device, this would entail large amount of loss through absorption.

[7] This, of course, is somewhat unfair and ignores some remarkable results in this field.

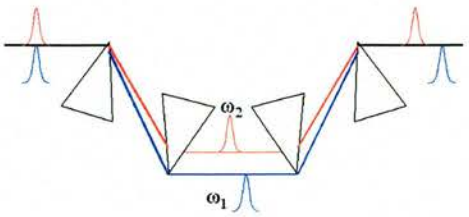

Fig. 1.5: Four prisms may be aligned to produce negative group delay dispersion.

Kerr Modelocking

THE DRAMATIC reductions in pulse duration in dye lasers illustrated in figure 1.3, came as a result of initially CPM and then intracavity chirp compensation. In Ti:Sapphire lasers, increasing the effectiveness of the modelocking element also enjoyed success, though in a different form.

In the 90s, Spence *et al.* developed Kerr Lens Modelocking in solid state lasers, see figure 1.6. This method rapidly gained the interest of many other research groups. In conjunction with other advances, such as SESAMs, these systems went on to produce the shortest pulses to date- 5fs.

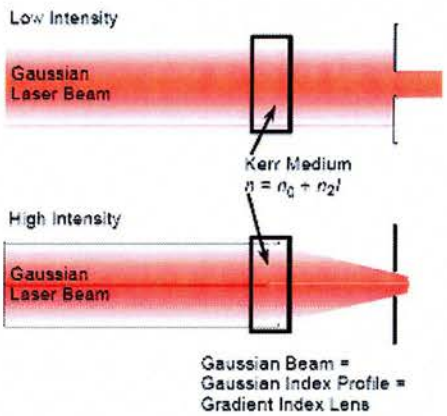

Fig. 1.6: In Kerr lens modelocking, a high energy experiences self focusing in the nonlinear material. This causes it to experience less loss on passing through an aperture. Reproduced from [52].

Solid state Ti:Sapphire lasers were a much more attractive source of ultrashort pulses than dye laser systems, both for the high output powers possible and its more friendly nature (a crystal as opposed to a stream of carcinogenic dye). With the advent of diode lasers as the pump source, these systems became very practical and are commercially available as products such as the Spectra Physics Mai Tai.

The potential of semiconductor media as a medium for ultrafast lasers is probably not less than that of Ti:Sapphire. Clearly the introduction of modelocking as effective as Kerr Lensing may trigger a similar revolution.

1.3 Summary

THE CURRENT stage of development in monolithic semiconductors is something of a "catch-22"situation. One approach is to make the gain medium more favourable to pulses using Quantum Dots. This may prevent chirping through a low linewidth enhancement. Without SPM, however, the pulse fails to engage enough of the gain bandwidth to support ultrashort pulses. Therefore another component is necessary.

It should be noted that while CPM in macroscopic lasers has largely been superseded by other methods, it still holds the record for ultrashort pulse production in monolithic semiconductor lasers [46] and [25]. The majority of modern solid state lasers are now modelocked through a SESAM/SBR.

In this chapter, we have highlighted two different avenues of research- introducing monolithic chirp compensation and strengthening the modelocking element. The realisation of these would promise to produce an ultrafast monolithic semiconductor laser. These two ideas are examined in detail in this thesis and, despite their difficulties, are shown to be possible means of achieving genuinely ultrashort pulses from a semiconductor laser.

Part I

FABRICATION AND FUNDAMENTAL TECHNIQUES

2. BASIC THEORY AND MODELING

IN this chapter, we first describe the main methods of pulse production in semiconductor lasers. We then discuss some of the basic theory and modeling techniques used to study semiconductor lasers. We start from the basic equations describing modelocking and determine some of the requirements and limitations. Then, using a phenomenological approach, we derive a set of rate equations that describe the working of a semiconductor laser. We then solve these analytically for a static device and briefly look at some of basics features of a laser. This model may be used to model the dynamics of semiconductor laser without making any assumptions as to the cavity geometry and dispersion.

2.1 Pulse Generation in semiconductor lasers

THERE ARE a number of ways of producing short pulses from a monolithic semiconductor laser. Gain switching, Q-switching and modelocking are those most commonly used in monolithic devices.

2.1.1 Gain-Switching

SEMICONDUCTOR lasers are unique in that their output may be modulated through the diode current. This leads to the simplest method of producing pulses- gain switching. The device is biased below threshold and a pulsed current (50-1000ps) superimposed. As a result of the electrical pulse the carrier density increases from below the lasing threshold to above. The device then starts to lase, rapidly depleting the carrier density. Due to the short cavity length and high cavity loss, the photon lifetime is low allowing the production of optical pulses which are shorter than the drive current pulses. As the optical pulse train is sychronised off the electrical signal, the resulting timing jitter can be very low [13].

2.1.2 Q-Switching

IN Q-SWITCHING, a multisection device is used. One section provides gain while the other is use to modulate the cavity Q-factor. It is initially in a high loss state preventing lasing from occurring. As the other section is still being pumped, its carrier density builds up to a level which can be much higher the normal threshold carrier density. The high loss section is been changed a low loss state (either actively with current pulses etc. or passively when a noise spike saturates the absorption). This leads to the release of a very high intensity optical pulse. Due to spontaneously emitted photons during the build up phase, the timing jitter is high in these devices [13].

2.1.3 Modelocking

IN MODELOCKING, a large number of longitudinal modes are phaselocked together through the action of the modelocking element- gain/loss modulation in the active case, saturable absorber in the passive, or both for hybrid. The physical principles behind the operation of modelocking will be given in the next section.

Passive

The pulse shortening effect of a saturable absorber is, in general, the most effective method in producing ultrashort pulses.The repetition rate is determined only by the cavity length and can be be very high (100+GHz). Average powers are typically in the range 5-20mW, resulting in low peak powers due the high repetition when compared with the above methods. Due to the lack of an external driving signal timing jitter is poorer than that of gain switched devices, though better than Q-switched devices.

Active

ACTIVE modelocking is achieved by modulating the gain or loss of the laser at the cavity roundtrip frequency. However, due to the short length of a monolithic semiconductor laser cavity, very high frequencies are required, making it somewhat impractical. The required modulation frequency may be reduced by anti-reflection coating one facet of the device and placing in an external resonator. Pulses, as short as 2-3ps may be generated with high peak powers (1W) and low jitter [13]. The macroscopic scale of the cavity also allows the possibility of adding additional components, such as Gires-Tournois Interferometers [51]. However, performance is limited by the quality of the anti-reflection coating. Additionally, the external cavity is not mechanically stable.

Hybrid modelocking uses an actively modelocked device which also has a saturable absorber section. The combination of these two effects can give an enhanced pulse shortening rate. This been used to produce 1ps pulses [13].

Table 2.1 shows the relative performance of the the various monolithic options.

Type	Pulse Energy	Pulse Duration	Jitter	Repetition Rate
Gain Switching	Medium (1W)	10ps	Good	10GHz
Q-Switching	High (10W)	30ps	Poor	10GHz
Passive Modelocking	Low (100mW)	1ps	Fair	100+GHz

Tab. 2.1: A comparison of the main methods of producing short pulses in monolithic semiconductor lasers.

2.2 Theory of Modelocking

IF THERE are N modes oscillating in the cavity, then the total electric field is given by:

$$E(t) = \sum_{j=0}^{N-1} A_j cos(\omega_j t + \phi_j), \tag{2.1}$$

where A_i is the amplitude of the ith mode, ω_i is its frequency and ϕ_i is its phase.

In general, when the electric field builds up from noise, both the amplitude and phase have random values resulting in a very noisy signal, see figure 2.1. The values of ω_i are fixed by the longitudinal mode spacing, giving $\omega_i = \omega_0 + j\Delta\omega = \omega_0 + j\frac{\pi c}{L}$ where ω_0 is the frequency of the first mode and L is the length of the cavity.

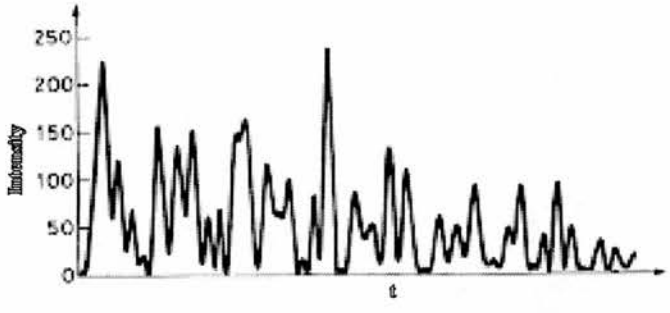

Fig. 2.1: When there is no phase relationship between modes, the output of the laser consists of a series of noise spikes. Reproduced from [53].

If the phases, ϕ_i, can somehow be made constant, (i.e. if the phases can be "locked"together), then equation 2.1 becomes:

$$E(t) = A \sum_{j=0}^{N-1} e^{i[(\omega_0 + j\Delta\omega)t + \phi]}, \tag{2.2}$$

where, for simplicity, we assume that the amplitude of each mode is equal. This now has the form of a geometric progression, and following some rearrangement, may be written as:

$$I(t) = E^*(t)E(t) = A^2 \frac{sin^2\left(\frac{1}{2}N\Delta\omega t\right)}{sin^2\left(\frac{1}{2}\Delta\omega t\right)}, \tag{2.3}$$

This expression, interestingly, has the same form as that of the diffraction grating equation [54]. This is plotted in figure 2.2. The resolution of a diffraction grating depends on the number of lines, similarly the "resolution"of a laser (i.e. the pulse duration) depends on N, the number of cavity modes locked together. This is perhaps one of the most intuitive explanations of the origin of the transform limit.

Thus, if one desires short pulses, a large spectral bandwidth is required. An examination of equations 2.2 and 2.3 gives this quantitative relationship between the spectral bandwidth

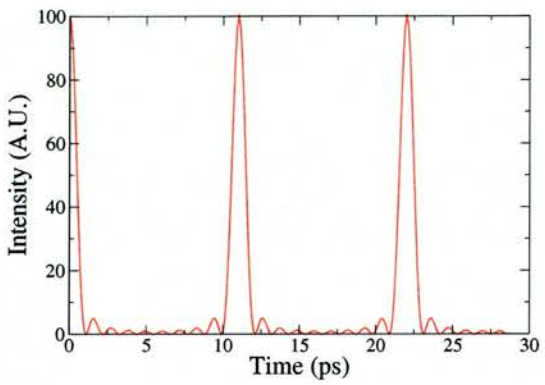

Fig. 2.2: The equations governing the modelocked output are, in fact, very similar to those describing light diffracting from a diffraction grating.

and pulse duration for gaussian shaped pulses:

$$\Delta t_p \Delta \nu = 0.44, \tag{2.4}$$

where Δt_p is the pulse duration, $\Delta \nu$ is the bandwidth of the pulse. This is plotted in figure 2.3.

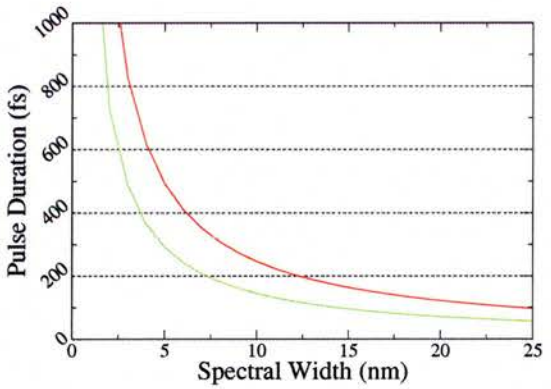

Fig. 2.3: The dependence of the pulse duration on the spectral width (for transform limited pulses). The centre wavelength of the pulse is also important. The green curve is for a centre wavelength of 1000 nm and the red for 1300 nm.

A way of achieving this phase locking is then required. One of the simplest methods is to place an amplitude modulator in the cavity and drive it at a frequency ω_m. The longitudinal modes oscillating in the cavity, ω_j, then acquire sidebands at $\omega_j \pm n \times \omega_m$, where n is an integer, see figure 2.4a. If this modulation frequency is equal to the longitudinal modespacing, then the sidebands tend to lock each mode to its neighbours, see figure 2.4b [55].

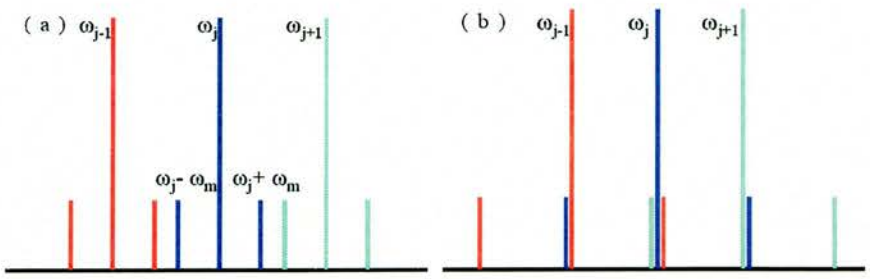

Fig. 2.4: When one of the cavity modes, ω_j is modulated at a frequency ω_m, sidebands are generated. If this modulation frequency matches the mode spacing, then the modes become coupled, locking their phases.

This mechanism is the one used in active modelocking, where either the gain itself or a loss element is modulated at the cavity repetition frequency. Alternatively, passive modelocking may be used whereby no external modulation is provided, instead the pulse modulates itself in a saturable absorber.

The mechanism by which passive modelocking occurs is relatively easy to understand when considered in the time domain. A high energy pulse may saturate the absorber and experience a lower loss. Pulsing is then the energetically most efficient mode of operation and is preferred, see figure 2.5.

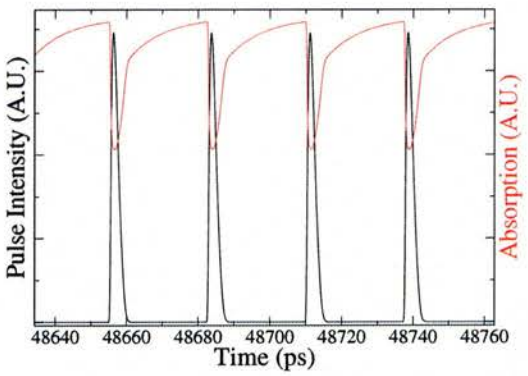

Fig. 2.5: Passive modelocking of a two section device. A high energy pulse may saturate the absorber and experience a lower loss. The black line shows the pulse, the red curve is the loss. A high energy pulse saturates the absorber reducing the loss. This creates a window in which the gain exceeds the loss.

The leading edge of the pulse is shortened and shaped by the absorber. If the pulse is long relative to the recovery time of the absorber (a fast saturable absorber) then the absorber may also shape the trailing edge of the pulse. Kerr lens modelocking is an example of this. The Kerr effect has a near instantaneous response and in the correct cavity configuration, it behaves as a fast saturable absorber (this technique has been used to produce the shortest pulses to date- $4-5$ fs) . In contrast, if the pulse is much shorter than the recovery time

(a slow saturable absorber), then the absorber remains fully saturated as the trailing edge passes and little or no shortening occurs. Nonetheless, the trailing edge may be shortened as a result of saturation in the gain section. This second mechanism imposes the condition on the device that the gain must recover slower than the absorber so that this window opens up. After passage of the leading edge the gain is depleted and consequently the trailing edge may experience a net loss [7]. Semiconductor Saturable Absorber Mirrors (SESAM) usually operate in the slow modelocking regime. These may produce pulses up to thirty times shorter than the recovery time of the absorber [56]. This is, also, the regime typically encountered in semiconductor lasers.

A consideration of the assumptions made in the derivation of equation 2.3 suggests some of the problems which occur in practice. Firstly, the amplitude of the modes typically varies over the pulse spectrum. If the method of modelocking is of insufficient strength, then the modes will not be fully locked and the assumption of identical phase breaks down. Similarly, if dispersion is high, then we cannot assume that each mode has an identical spacing. Therefore, in reality, only when the net cavity dispersion is low and modelocking works effectively will transform limited pulses be obtained. Furthermore, the equations assume that the saturable absorber simply couples the modes and ignores the effects of the saturable absorption itself.

2.3 Rate equations

IN A semiconductor material, electrons and holes may be excited to higher energy states and recombine to release light. This may occur spontaneously, with the emission of incoherent light in all directions, or after stimulation by another photon, after which the emitted photon is an exact copy of the original. This results in highly directional, coherent light. When there are more electrons and holes in (suitable) excited states than in the ground state, known as a population inversion, the light is amplified, and when this overcomes the various cavity losses, lasing is achieved.

In a modern semiconductor laser, a *pin* diode junction injects electrons and holes (charge carriers) into the active region[1], shown schematically in figure 2.6 [57]. This consists of a layer of undoped material sandwiched between layers of heavily N- doped and P- doped material, (10^{18}atoms cm^{-3}). As the doping is high, at the equilibrium condition, the Fermi level of the p-doped material lies in the valence band and that of the n-doped material lies in the conduction band, figure 2.6a and both have the same energy When a forward bias is applied, the two levels become separated, figure 2.6b, where the amount of separation is approximately given by:

$$\Delta F \approx eV, \tag{2.5}$$

where V is the applied voltage and e is the electron charge. When $\Delta F \cong E_g$, where E_g is the bandgap of the material, carriers are injected into the undoped i-region and current starts to flow [58]. In a well designed device, most of these injected carriers relax into the quantum well(s)[2], where they may create the population inversion necessary for lasing.

[1] The active region is defined as the region in which recombining carriers contribute to useful gain and photon emission [59].

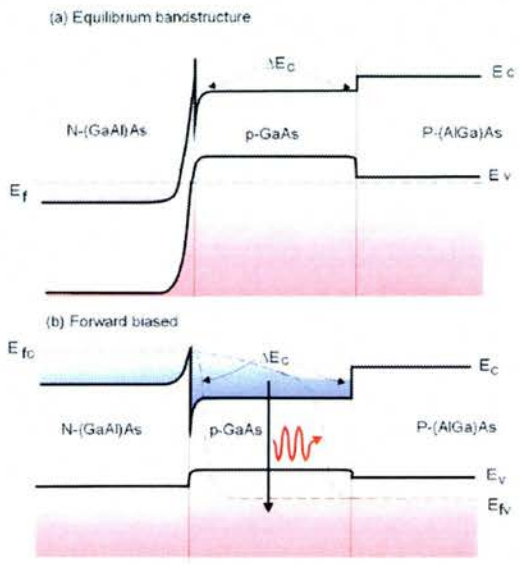

Fig. 2.6: A schematic of how carriers are injected into the active layer. A double heterostructure is illustrated here. A quantum well device has a similar structure and once carriers are injected into it, they relax into the quantum well(s), which are usually situate centrally in the double heterostructure. (Reproduced from [60].)

2.3.1 Carrier Dynamics

IN A typical device under normal operating conditions, charge neutrality ensures that the number of electrons and holes is equal. This allows us to consider only the electron density N.

We may consider the carriers in the active region as a "reservoir", to which carriers are added by certain processes and removed by others, figure 2.7:

$$\frac{dN}{dt} = G_{generation} - R_{recombination}, \tag{2.6}$$

where $G_{generation}$ are the processes which create carriers and $R_{recombination}$ the recombination processes which deplete carriers. Carriers are injected by the current:

$$G_{generation} = \frac{\eta_i I}{eV}, \tag{2.7}$$

where I is total current, e is the charge on the electron and V is the volume of the active area. $R_{recombination}$is due to spontaneous and stimulated emission and nonradiatve recombination:

$$R_{recombination} = R_{radiative} + R_{nonradiative}, \tag{2.8}$$

$$= (R_{sp} + R_{st}) + (BN^2 + CN^3), \tag{2.9}$$

[2] The internal quantum efficiency η_i is defined as the fraction of the terminal current which generates carriers in the active region.

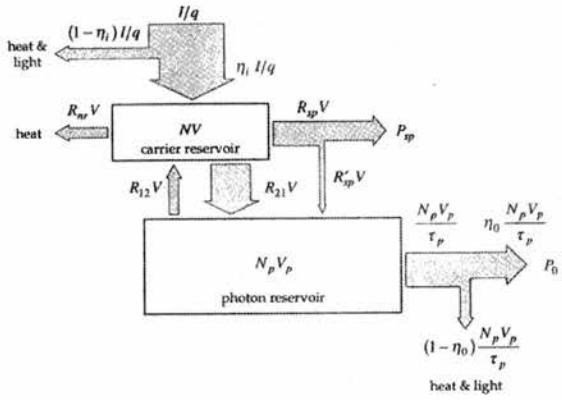

Fig. 2.7: Schematic of the carrier and photon density reservoirs, showing the various processes which create and deplete carriers/photons. We define the net stimulated emission rate, $R_{st} = R_{21} - R_{12}$, where R_{21} and R_{12} are the stimulated emission and absorption respectively. The arrows correspond to carrier/photon *number* flowing per unit time, ensuring carrier conservation. n_0 is the optical efficiency of the device and describes the number of photons escaping from the cavity. [61]).

where B and C are the bimolecular and Auger recombination rates respectively, R_{sp} is the spontaneous emission rate and R_{st} is the stimulated emission rate[3].

2.3.2 Gain

Quantum Wells

THE development of the quantum well led to a revolution in the world of semiconductor lasers. It allowed a sufficient reduction in the threshold currents, see figure 2.8, such that semiconductor lasers could be operated without considerable cooling apparatus. Coupled with the ability to produce output powers of up to and beyond a watt (with cooling), they are the dominant type of semiconductor laser currently in use (and in fact, compete with and often surpass other types of lasers in many areas).

The introduction of Quantum dots was expected to produce a similar revolution. The lowest threshold current densities to date have been demonstrated using Quantum dots, however the considerable expansion in usefulness and application that occurred with Quantum wells is yet to be seen. The Quantum well revolution occurred because Quantum Wells considerably reduced the gain volume relative to bulk to devices. This lowered the number of states which had to be inverted before lasing could take place, thus reducing the threshold currents to that which may achieved without extensive cooling. Quantum dots reduce the gain volume further with a corresponding reduction in threshold currents. However, this time, the gain volume is small enough that gain saturation may occur before a useful level of output is attained[4]. In many of the Quantum Dot materials used in this thesis, multiple layers of Quantum Dots (up to 10) were used to achieve the necessary gain, returning

[3] Under certain conditions (i.e. in a saturable absorber section), the opposite of stimulated emission occurs- absorption. This creates carriers and is represented here by here by R_{st} going negative.

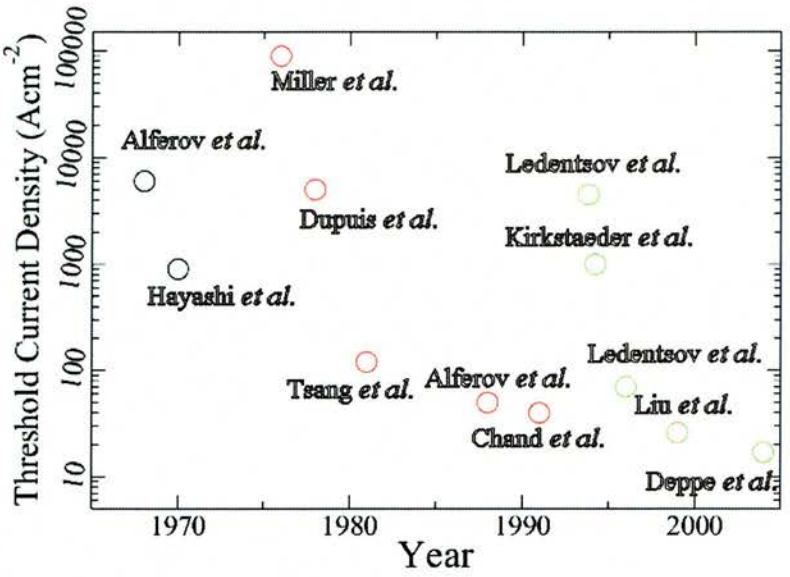

Fig. 2.8: The reduction in the lasing threshold of semiconductor lasers over time. The introduction of quantum well caused a considerable improvement in the usefulness of semiconductor lasers. Quantum dots have shown the lowest threshold current densities so far, however, they are yet to trigger a revolution similar to that due to quantum wells as they sacrifice gain for threshold. (Double heterostructure lasers are shown in black, quantum well lasers in red and quantum dots in green) [62].

the threshold currents to levels only slightly better than Quantum Wells. It is, therefore, unlikely that Quantum Dots will fully replace Quantum Wells, at least on the basis of a threshold current argument. Nonetheless, in many niche applications, the other features of Quantum Dots offer considerable advantages.

A Quantum Well occurs when the active region is reduced to a thickness, L_z, on the order of the de Broglie wavelength of the carriers. Following from the quantum mechanical problem of a particle in a one-dimensional potential well, the allowed energy levels of the carrier then become quantised in the direction perpendicular to the plane of the quantum well (a continuum of energies exist in the plane). Relative to the double heterostructure design (see figure 2.6, for an example), which has a continuum of energy levels, much less pumping is then required to invert a sufficiency of states to achieve the population inversion necessary for lasing[5].

In order to calculate the quantisation energy, the Schroedinger equations for a one dimensional potential well must be solved. In the z direction, this is:

$$E\phi = -\frac{\hbar^2}{2m}\frac{d^2\Psi}{dz^2}, \tag{2.10}$$

[4] This side effect is also present in Quantum Wells though to a lesser degree. In some exceptionally high power applications, bulk semiconductor devices are favoured.

[5] Nevertheless, in a quantum well laser, a double heterostructure like structure is still retained for carrier injection and optical confinement (usually know as a separate confinement heterostructure- SCH).

for $0 \leq z \leq L_z$, (inside the well), and

$$E\phi = -\frac{\hbar^2}{2m}\frac{d^2\Psi}{dz^2} + V\Psi, \tag{2.11}$$

for $z \geq L_z$; $z \leq 0$, (outside the well), where Ψ is the wave function and V is the depth of the well, following [63].

The solutions are:

$$\Psi = \begin{cases} Ae^{k_1 z} & : \quad z \leq 0 \\ Bsin(k_2 z + \delta) & : \quad 0 \leq z \leq L_z \\ Ce^{-k_1 z} & : \quad z \geq L_z \end{cases} \tag{2.12}$$

where $k_1 = \left[\frac{2m(V-E}{\hbar^2}\right]^{\frac{1}{2}}$, $k_2 = \left(\frac{2mE}{\hbar^2}\right)^{\frac{1}{2}}$ and A, B, C and δ are constants. Applying the boundary conditions (continuity of Ψ and $\frac{d\Psi}{dz}$ at the interfaces) gives the eigenvalue equation:

$$tan(k_2 L_z) = \frac{k_1}{k_2}, \tag{2.13}$$

which must be solved numerically. The resulting energy levels are shown in figure 2.9.

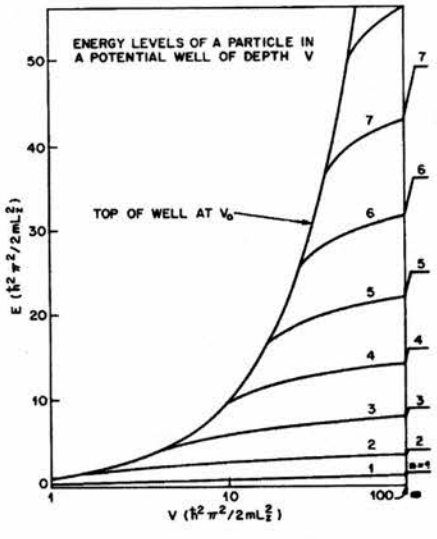

Fig. 2.9: The energy levels in a finite potential well. The levels corresponding to an infinite well are shown on the righthand axis. The emission energy, E, is shown on the y-axis and and the well depth , V, is on the x-axis. For clarity both are given in reduced units $\frac{\hbar^2\pi^2}{2mL_z^2}$. The curve represents the top of the well, $E = V_0$, no quantised states exist with energies above this. Reproduced from [63].

Clearly from the schematic of figure 2.10, in order to calculate the energy of the emitted light, the energy levels of the electrons in the conduction band and the holes in the valence band must be known. The values of E_{xc} are found by solving equation 2.13 for the potential formed in the conduction band, and similarly for E_{xhh} in the valence band[6]. The values of ΔE_c and ΔE_v are found in the literature from experimental measurements [64].

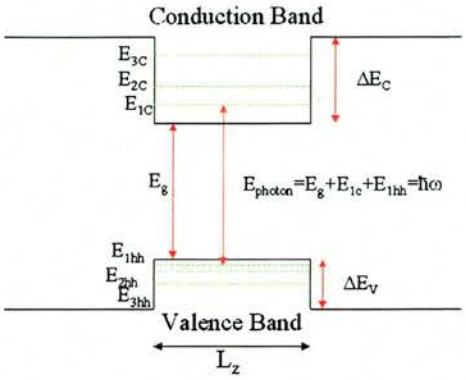

Fig. 2.10: A schematic showing the position of the energy levels of the electrons and the heavy holes. Light is emitted from transitions between levels in the conduction and valence bands. Thus, the photon energy, $\hbar\omega$, always exceeds the band gap energy, E_g. ΔE_c and ΔE_v are the conduction and valence band offsets and E_{xc} and E_{xhh} are the allowed energy levels in the conduction and valence band respectively.

Thus, for a particle confined in a quantum well, the energy eigenvalues are given by:

$$E(n, k_x, k_y) = E_n + \frac{\hbar^2}{2m_n^*}(k_x^2 + k_y^2), \tag{2.14}$$

where E_n is the nth energy level for motion perpendicular to the well, m_n^* is the effective mass of the carrier in the relevant level and k_x and k_y are the wave vector components in the plane of the well.

By solving equation 2.13, the quantised energy levels may be obtained for a given well width and depth. Figure 2.11a shows the dependence of the energy of the lowest state as function of the well width, for a $In_{0.18}GaAs$ well with GaAs barriers. The equivalent graph for varying indium fraction and constant well width is shown in figure 2.11b.

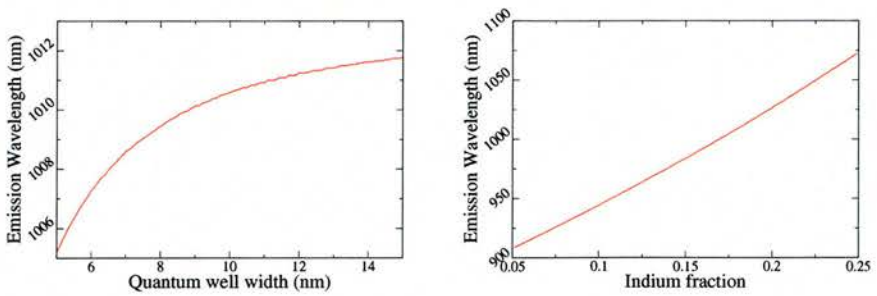

Fig. 2.11: a) The emission wavelength of a InGaAs Quantum well as a function of well width. The indium fraction was held at 0.18. Values for the conduction and valence band discontinuities were taken from [63]. b) The dependence of the emission wavelength on the Indium fraction. The well width was 7.5nm.

[6] For simplicity, we consider only the heavy holes in the valence band. Light holes may be included by using a different effective mass.

Gain as a function of Carrier Density

WHEN more light is amplified than absorbed the material is said to have a gain greater than unity. There is, in general, a nonlinear dependence of this gain on the carrier density. Broadly speaking, the gain is proportional to the population inversion, see figure 2.12, the amount of which depends on the pumping. This can be calculated through a consideration of the Fermi factor and the quasi-Fermi levels, the values of which depend on the number of carriers which are injected, see figure 2.6. It is also necessary to calculate the density of states with energy (a step-like dependence rather than the parabolic dependence of bulk material) and consider the momentum selection rules.

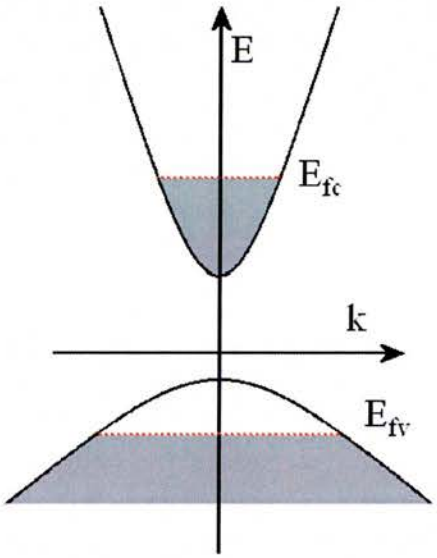

Fig. 2.12: Schematic of a population inversion. There is a population of electrons (grey) in the conduction band, while there is a popluation of holes in valence band (indicated by an absence of electrons). The size of these populations are governed by the position of the quasi-fermi energies, E_{fc} and E_{fv}.

It can be shown, [64] and [65], that the gain has a logarithmic dependence on the carrier density. For the gain calculation necessary for our rate equations, we approximate this logarithmic curve as two linear curves:

$$g = g_n(N - N_{tr}), \tag{2.15}$$

where N_{tr} is the carrier density at transparency and g_n is the differential gain $\frac{dg}{dN}$ (with different values above and below N_{tr}, see figure 2.13.

The gain also has a spectral dependence. As carriers are injected into the well, the lower energy states fill up, forcing carriers to higher energy states with a consequent expansion of the gain spectrum to shorter wavelengths, see figure 2.14. This can be calculated following [65].

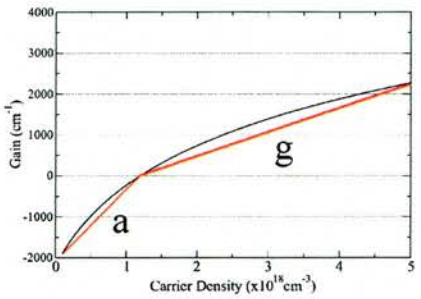

Fig. 2.13: The gain of a quantum well as a function of carrier density.

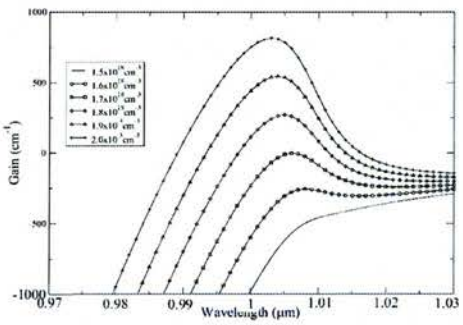

Fig. 2.14: The dependence of the gain spectrum on the carrier density. Courtesy of Michael Flynn [66].

2.3.3 Photons

SIMILAR to above, we can consider the photons in the active region as a reservoir. Thus, we have the following rate equation:

$$\frac{dP}{dt} = \Gamma R_{st} + \Gamma \beta_{sp} R_{sp} - \frac{P}{t_p}, \tag{2.16}$$

where t_p is the photon lifetime.

When a photon stimulates an electron and hole to recombine, another identical photon is emitted adding to the number of photons in the cavity. This rate of generation, R_{st}, is the main term contributing to the photon density. However, as we are considering the photon density, we must remember that the volume occupied by the photons is usually much larger than that occupied by the carriers. Thus, we must include the confinement factor of light to the quantum well, Γ, in equation 2.16, see figure 2.15. This is defined as $\frac{V}{V_p}$, where V is the volume occupied by the carriers, i.e. the volume of the quantum well, and V_p is the volume occupied by the photons.

In passing through an infinitesimally small length of the device, Δz, the photon number grows according to:

$$P + \Delta P = P e^{g \Delta z}, \tag{2.17}$$

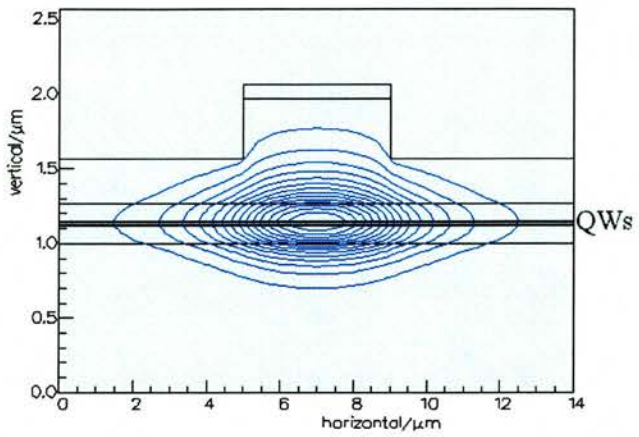

Fig. 2.15: Only a small fraction (3-5 %) of the optical mode interacts with the Quantum wells.

As $e^{g\Delta z} \approx 1 + g\Delta z$ and $\Delta z = \nu_g \Delta t$, where ν_g is the group velocity, we can rearrange and write R_{st}, the rate at which photons are generated, as follows:

$$R_{st} = \frac{dP}{dt} = \frac{\Delta P}{\Delta t} = \nu_g g P, \tag{2.18}$$

When a photon is released through spontaneous emission, this photon will not necessarily contribute to the useful output from the laser. It may be emitted into any one of the many modes present in the cavity (typically thousands in an edge emitting diode) of which only one (in a single mode device) will be of interest, see 2.16. The factor β_{sp} takes this is into account and is the reciprocal of the total number of modes [59], given by:

$$\beta = \frac{\Delta\Omega_{cav}}{8\pi} \frac{4}{1-R}, \tag{2.19}$$

where $\Delta\Omega_{cav}$ is the solid angle subtended by the cavity mode and R is the mirror reflectivity, following [67]. The spontaneous emission rate is given by:

$$R_{sp} = \frac{N}{t_{sp}}, \tag{2.20}$$

where t_{sp} is the spontaneous emission lifetime, (usually on the order of a nanosecond).

The photon lifetime is introduced to account for the cavity loss, which encompasses scattering losses and the escape of photons through the mirrors to give an output. To determine this parameter, we consider the gain at the lasing threshold.

By definition, at threshold, the gain, $g_t h$ is equal to overcome all the cavity losses. Considering one pass through a device at threshold then gives:

$$I_0 e^{(g_{th} - \kappa_i)2L} r_1 r_2 = I_0, \tag{2.21}$$

where I_0 is the initial light intensity, κ_i is the internal loss, L is the device length and r_1 and r_2 are the intensity facet reflectivities, see figure 2.17. Taking the natural logarithm

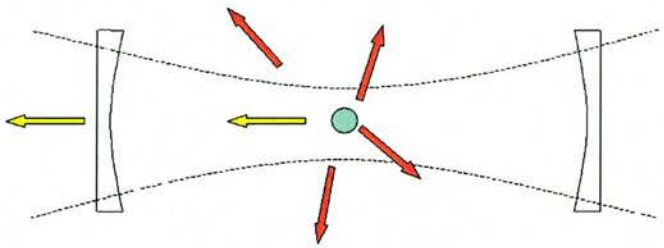

Fig. 2.16: The origin of the beta parameter. When photons are emitted spontaneously, most (red) do not enter the mode to give a useful output (shown by the dotted lines). Typically only a small fraction (yellow) enter the mode.

and rearranging leaves:

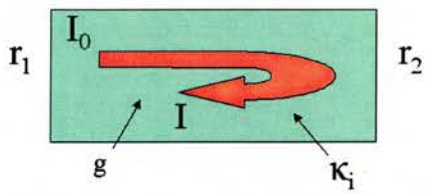

Fig. 2.17: As the optical mode, of initial intensity I_0, propagates, it experiences an effective gain $(g - \kappa)$. At each facet a fraction is lost to the outside world. At threshold, the increase in intensity due to gain exactly balances the losses (both internal and mirror).

$$\Gamma g_{th} = \langle \kappa_i \rangle + \frac{1}{L} ln \left(\frac{1}{R} \right), \tag{2.22}$$

where $R = \sqrt{r_1 r_2}$.

Exactly at threshold, the nett rate of photon generation $\frac{dP}{dt}$ is zero, thus combining equations 2.16, 2.18, 2.20, and 2.22 gives an expression for t_p:

$$\frac{1}{t_p} = \nu_g \left[\langle \kappa_i \rangle + \frac{1}{L} ln \left(\frac{1}{2R} \right) \right], \tag{2.23}$$

This then allows us to state the two rate equations in their final forms:

$$\frac{dP}{dt} = \Gamma \nu_g g P + \beta_{sp} \Gamma \frac{N}{t_{sp}} - \frac{P}{t_p}, \tag{2.24}$$

and

$$\frac{dN}{dt} = \eta_i \frac{I}{eV} - \frac{N}{\tau_n} - BN^2 - CN^3 - (\nu_g g) P. \tag{2.25}$$

This model may be used to examine the dynamic behaviour, in particular modelocking,

of semiconductor lasers. The phase-locking of modes arises naturally without any need to artificially assume a phase relation such as that of equation 2.2. Similarly, a fixed mode spacing is not assumed. Dispersive effects, such as Self Phase Modulations, automatically occur[7]. Thus, almost arbitrary designs and cavity qeometries may be considered using this model.

2.4 Analytical Modeling

BY SOLVING the coupled differential equations 2.24 and 2.25 using a simple numerical algorithm, we may obtain the most fundamental feature of diode lasers: the Power-Current curve (P-I curve), shown in figure 2.18.

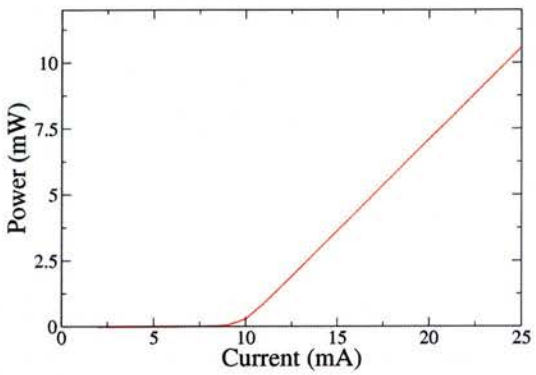

Fig. 2.18: Modelled output power versus current for a diode laser. We calculate the power from $p = \nu_g \frac{1}{L} ln(\frac{1}{R}) PhfV_p$. The slow increase in output while below threshold is a result of spontaneous emission. The device had a length of 1mm, a width of 5 μm and facet reflectivities of 0.3.

We consider a 1 mm long, 5 μm wide device with cleaved facets. These have a reflectivity of 0.3 (standard Gallium Arsenide- Air interface). The threshold current determined from this curve is approximately 10mA. This corresponds to a threshold current density of 200 Acm^{-2}. Below this current, light is emitted spontaneously and only slowly increases with pumping. Above threshold, the slope is linear. From this curve, important device characteristics such as the differential quantum efficiency may be determined. Figure 2.19 shows the corresponding carrier density with current. Initially, this increases with current. Once threshold is reached, the carrier density "clamps"and remains constant regardless of any further increase in current.

This model may be extended to deal with simple dynamic effects, such as the relaxation response, provided the deviations from the steady state are relatively small, see [59].

[7] We do not include material dispersion in our equations and model, as we judge its effects to small relative to SPM. However, it may be added relatively easily.

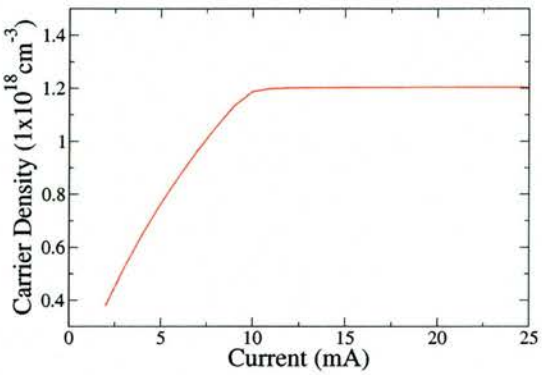

Fig. 2.19: The dependence of the carrier density on current for the device shown in figure 2.18. When the laser reaches threshold the carrier density "clamps".

2.5 Numerical Modeling

THIS WORK was carried out in conjunction with Michael Flynn. A more detailed description of the model may be found in his thesis, along a detailed discussion of its accuracy and validity.

Analytical expressions have been very successful in describing the static and simple dynamic properties of semiconductor lasers. The examination of a dynamic multi-section device such as modelocked semiconductor lasers, however, requires a numerical approach[8].

Our model is based on that reported by Schell *et al.* [69]. We have extended this model through the additional of extra terms, discussed below. A detailed discussion of our model was published in [70] and also in [66].

The initial assumption of our model is that the laser is inherently a one dimensional problem. This is accurate, so long as the laser operates in a single transverse mode, see section 4.3. In fact, in most applications of laser diodes, output in a single mode is a fundamental requirement. Thus, this assumption does not imply any loss of generality.

To model the laser, we break it up into a number of small segments. Each segment is assigned an identifying number and the values of carrier density, N, the gain g, forward traveling and backward traveling waves, E^+ and E^- are recorded for each segment[9], see figure 2.20. While the transverse components of the solution are taken as constants and do not appear in the following equations- they are included the calculation via the confinement factor of light to the quantum wells, Γ, and play an important role in the behaviour of the device. As our pulses are long compared with the underlying carrier wave, we can make the slowly varying envelope approximation which considerably simplifies our task. In section 2.3, we derived rate equations governing the photon density. This is incorporated into the wave equation to give the following equation, which governs the propagation of light through our device:

[8] Such dynamic properties may still be described analytically, however many such models require very sophisticated techniques [68].

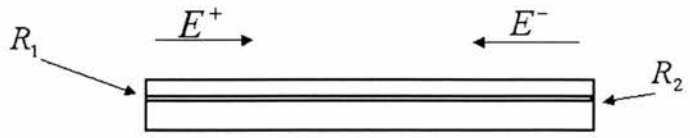

Fig. 2.20: We model the device by breaking it up into segments. The carrier rate equations and the wave equation are then solved in each segment.

$$\left(\frac{\partial}{\partial t} \pm \nu_g \frac{\partial}{\partial z}\right) E^{\pm} = \frac{(\nu_g \Gamma g - \kappa)}{2} E^{\pm}(z,t). \tag{2.26}$$

where ν_g is the group velocity and κ is internal dissipative loss.

We model the instantaneous gain g_0 with:

$$g_0 = g_n \frac{(N - N_0)(1 + i\alpha)}{1 + \epsilon S}, \tag{2.27}$$

where S is the photon density[10]($|E^+|^2 + |E^-|^2$), g_n is the differential gain, N_0 is the carrier density at transparency, α is the line-width enhancement factor and ϵ is the gain compression factor.

The simple gain equation of section 2.3.2 has been expanded to account for two additional phenomena. The effects of the carrier dependence of the refractive index (Self Phase Modulation) are included through the linewidth enhancement factor in the term $i\alpha$. Spectral hole burning in the gain and absorber absorber appears as $1 + \epsilon S$. This, in practice means that very high intensity light experiences a reduced gain. The true gain, g, lags behind g_0 as a result of the finite gain relaxation time, t_{nl}, through:

$$\frac{\partial g}{\partial t} = \frac{g_0 - g}{t_{nl}}, \tag{2.28}$$

following [71].

The carrier density rate equations were derived in section 2.3.1 and are represented in the model by:

$$\frac{\partial N}{\partial t} = \eta_i \frac{J}{ed} - \frac{N}{\tau_n} - BN^2 - CN^3 - \nu_g \Re(g) S, \tag{2.29}$$

where J is the current density, d is the active region thickness[11], τ_n is the carrier lifetime, $\Re(g)$ is the real part of the gain, B and C are the bimolecular and Auger recombination rates respectively[12]. To account for the finite spectral gain bandwidth of the device an infinite impulse response filter was implemented in the model [72] [73].

When light travelling to the right is incident on the end mirror (usually the facet) a

[9] E^+, E^- and g are complex enabling us to keep track of the phase.

[10] Note the change from P to S in equations 2.18 and 2.27.

[12] For simplicity, we usually assume in the numerical model that η_i, the internal quantum efficiency, is 100%.

[12] Γ does not appear in equation 2.29 while appearing in equation 2.26, because these are photon and carrier *density* rate equations. If we had chosen to use photon and carrier *number* rate equations, the resulting equations would be symmetric [61].

fraction R_1 is reflected becoming light that travels to the left (and similarly at the other mirror). Thus the boundary conditions are applied using:

$$E^+(z=0,t) = \sqrt{R_1}E^-(z=0,t) \tag{2.30}$$

$$E^-(z=L,t) = \sqrt{R_2}E^+(z=L,t) \tag{2.31}$$

where L is the length of the device and R_1 and R_2 are the amplitude reflectivities of the facets.

Two numerical algorithms are then implemented to solve the equations, a time domain finite difference method for equation 2.26 and Euler's method for equation 2.29, e.g.

$$E^{\pm}(z \pm \Delta z, t+\Delta t) - E^{\pm}(z,t) \approx \left(\frac{1}{v_g}\frac{\delta E^{\pm}}{\delta t}\Delta t \pm \frac{\delta E^{\pm}}{\delta z}\right) v_g \Delta t, \tag{2.32}$$

and

$$\frac{\delta N}{\delta t}\,|_{z_i} = \frac{N(z_i, t+\Delta t) - N(z_i,t)}{\Delta t}, \tag{2.33}$$

see [66] for more details. Parameter values for the simulations were selected based on an InGaAs QW based device, lasing at a wavelength of 1 μm, see table 2.2.

Symbol	Description	Value
ν_g	Group velocity of light	0.857×10^{10} cm/s
Γ	Confinement factor	0.03
κ	Internal dissipative loss	5 cm^{-1}
N_0	Carrier density at transparency	1.2×10^{18} cm^{-3}
$g_{n,g}$	Differential gain at transparency (gain)	4×10^{-16} cm^2
$g_{n,a}$	Differential gain at transparency (abs.)	$1.2\times10^{-15}cm^2$
ϵ_g	Gain compression factor (gain)	$3.0\times10^{-17}cm^3$
ϵ_a	Gain compression factor (abs.)	$7.7\times10^{-17}cm^3$
α_g	Linewidth enhancement factor (gain)	3.2
α_a	Linewidth enhancement factor (abs.)	1.24
d	Active layer thickness	0.01 μm
τ_g	Nonradiative recombination rate (gain)	2 ns
τ_a	Absorber recovery time	5-50ps
$\tau_n l$	gain relaxation time	0.5 ps
R_1	Reflection at gain facet	0.3
R_2	Reflection at absorber facet	0.3
Δz	Length of spatial integration step	2 μm
B	Bimolecular recombination constant	$2.5\times10^{-10}cm^3/s$
C	Auger recombination rate	$5\times10^{-29}cm^6/s$

Tab. 2.2: Parameter values used in the model

In reality, pulses coalesce out of noise spikes in the spontaneous emission. In our model, spontaneous emissions was included through adding a complex Gaussian excitation term to the traveling wave equations, equation 2.26. Interestingly, in early versions of our model which did not include a spontaneous emission term, pulsing still occured. This started from numerical noise due to roundoff, i.e. if 1.5 is rounded to one decimal place, one may obtain 1 or 2 depending on whether the original number was 1.49999 or 1.50001.

The details of the model are discussed in greater detail in [66] where the validity of

the numerical method is demonstrated. The transients and turn on dynamics are also considered and the correct behaviour is observed. We have also compared the results of this model with of those of similar models in the literature. Reasonable agreement was observed. Exact agreement is unlikely, as different numerical algorithms were used (the exact details of which are usually difficult to find). Furthermore, the various terms included and methods for each vary from model to model.

2.6 Summary

IN THIS chapter, we have described the basic theory of semiconductor lasers and discussed some modeling techniques for such devices. We started off with a description of the basic (and ideal) theory of modelocking and illustrated some important features with a numerical model. As this relatively simple model of modelocking, leading to equation 2.3, is valid subject only to some broad assumptions, we then considered a more advanced model. We described a numerical traveling wave rate equation model that may be used to model real modelocked semiconductor lasers.

As should be apparent from the equations and assumptions, achieving the necessary conditions for modelocking is non trivial and, in practice, there are a number of physical effects which can interfere with and degrade the phase locking of modes.

3. PHOTONIC CRYSTAL FABRICATION

PHOTONIC CRYSTALS allow the control and manipulation of light on a wavelength scale. They consist of a periodic ($\approx \lambda$) strong modulation of the refractive index material (usually semiconductor to air). This periodicity may be in either one, two or three dimensions. Due to this strong refractive index contrast, light is scattered very strongly at each interference strongly modifying its propagation. This scattered light will then interfere with light scattered from other interfaces. The situation in which all light is reflected for a given wavelength range (in one or more directions) is known as a *photonic bandgap*. This allows the confinement of light to very small waveguides or cavities and the creation of very high reflectivity mirrors [74].

However, due to this requirement of wavelength scale periodicities, very demanding fabrication is required. This makes the fabrication of three dimensional photonic crystals to sufficiently high standards very difficult [75]. Furthermore, the integration of such structures into a semiconductor lasers poses even more difficulties. Two dimensional photonic crystals are a more promising alternative and very high precision fabrication is now possible [76] [77]. The incorporation of these and similar one dimensional crystals presents into semiconductor lasers presents little difficulty [78].

3.1 Overview

THE FABRICATION of two dimensional photonic crystals requires, as a first step, extremely accurate pattern definition. In order to satisfy this, it is necessary to use electron beam lithography as the required level of accuracy is, currently, beyond the resolution that can be achieved by straightforward optical lithographic methods. Recently, as an alternative, there has been a lot of progress in the fields of deep UV lithography and extreme UV lithography, which is making the use of optical lithography for Photonic Crystal definition practical [79]. However, the expense and complexity of these methods make them unsuitable for the small scale production typical in research.

Following lithography, the pattern must be transferred into a suitable mask (certain electron beam resists can themselves act as the etch mask[1]). Using high aspect ratio etching, the photonic crystal (one or two dimensional) pattern is then transferred into the semiconductor. This is probably the most critical step as failures at this stage, insufficient depth or high sidewall roughness for example, translate directly into poorer performance of the final device. Figure 3.1 shows an overview of the fabrication process.

[1] Though, most are too soft, especially if deep etching is required.

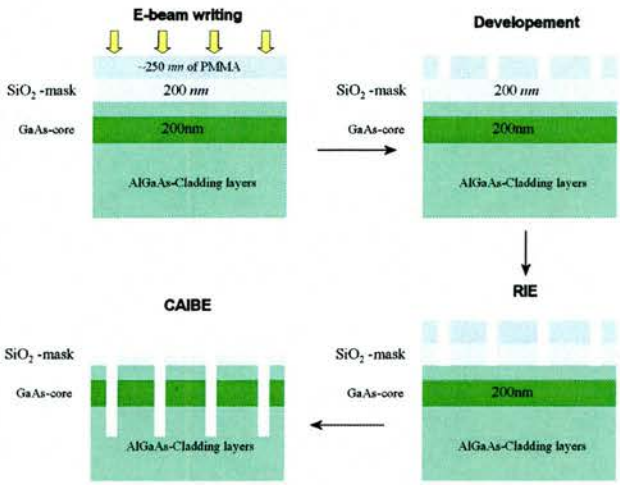

Fig. 3.1: An overview of the fabrication of photonic crystals. The desired pattern is initially created in electron beam resist using high resolution electron beam lithography. After development, this pattern is transferred into a silica hard mask using Reactive Ion Etching. Finally, the photonic crystal is deep etched using Chemically Assisted Ion Beam Etching.

3.2 Design Considerations for one dimensional photonic crystals

IN THIS section we look at maximising the performance of a one dimensional photonic crystal[2]. Light may be lost from the guided mode through a number of mechanisms. The etching of holes through a waveguide causes scattering as the hole has no vertical guiding. This usually couples light to radiation modes in the cladding resulting in loss. [80]. This problem may only be fully avoided if a Bloch mode may be excited (these cannot couple to radiation modes). However, this requires the use of a waveguide with a high refractive index contrast which can only be realised in membranes or with oxide claddings. Clearly, the integration of such features into an active device such as a laser would be very challenging.

In the more practical low contrast slab waveguides, achieving low-loss propagation remains a serious problem. Benisty *et al.* have shown that the loss, in fact, scales with the contrast (in apparent contradiction to the above[3]). Intuitively, the higher the contrast the tighter the confinement of the beam. Thus, it is more divergent and in the air sections it diffracts further experiencing a higher loss. Quantitatively, the loss is proportional to $\Delta\epsilon^2$, where $\Delta\epsilon = n_{core}^2 - n_{clad}^2$ with n_{core} and n_{clad} the refractive indices of the slab waveguide core and cladding respectively, [81]. Consequently, one method of reducing loss is to use a weak contrast waveguide. However, this has the disadvantage in that the mode has a very large vertical extent, placing additional requirements on the depth to which the holes

[2] In the literature, these one-dimensional photonic crystals are often described as Distributed Bragg Reflectors (DBRs). Strictly, this is correct, however it can be very misleading as DBR most often refers to the low contrast structures, created using a regrowth step, used in narrow linewidth lasers. These features are typically hundreds of periods long. Thus, in this context, it becomes difficult to describe our structures as "distributed". Therefore, throughout this thesis, we reserve the term DBR for such narrow linewidth lasers. We describe our own deeply etched high contrast structures as Bragg Reflectors, Bragg mirrors, or one-dimensional photonic crystals.

Order	Period (nm)	Air Section (nm)	Reflection at 1000nm	Loss
1st	300	250	Yes	0.41
	300	200	Yes	0.31
	300	150	No	
2nd	400	150	Yes	0.28
	400	100	No	
3rd	500	100	Yes	0.12

Tab. 3.1: A comparison between a number of potential mirrors, showing the order, period, air slot width and whether the mirror shows reflection at the desired wavelength. The loss is taken to be (1-R-T).

should be etched. A weak contrast waveguide with very deeply etched holes has been used by Kotlyar *et al.* to demonstrate record low loss in photonic crystal waveguides [77].

Another method of reducing this loss is to minimise the amount of air in the structure. In general, due to the very large contrast, incident light at the bandgap wavelengths is reflected very quickly, i.e. over very few periods. Thus, even non-ideal mirror designs may have high reflectivities, as light simply does not have the opportunity to scatter out of the waveguide. However, some of the later designs discussed in this thesis require light to penetrate well into the mirror, thus it is wise (as well as elegant) to design as low a loss mirror as possible.

Typically, in a multilayer Bragg stack, each layer is chosen to have an optical thickness of $\frac{\lambda}{4}$. This results in stopbands with the maximum width. However, one-dimensional photonic crystal mirrors, due to the refractive index contrast between the air and the semiconductor, have a stopband width of several hundred nanometres at a wavelength of 1000nm, well in excess of that required. Thus, one may depart from the perfect $\frac{\lambda}{4}$ condition without losing performance. In table 3.1, we look at a number of potential mirrors.[4]

A second loss mechanism is the coupling of light to substrate modes. The creation of air slots/holes removes material from the waveguide and cladding layers thereby reducing the effective refractive index in this region. As light naturally travels in the highest index region, the guided mode may couple to modes in the high index region below the crystal, see figure 3.2. In order to prevent this source of loss, the reduced index region due to the slots must be extended to a sufficient depth such that the guided mode does not feel the high index area, see figure 3.3 for a sample calculation. The only solution to this is to use etching techniques of a very high standard i.e. capable of etching high quality holes to large depths. This goal has led to the developement of Chemically Assisted Ion Beam Etching (CAIBE), see section 3.5 and Inductively Coupled Plasma (ICP) etching [82].

A final loss mechanism is sidewall roughness. This is a less complicated problem than those already mentioned but is still vitally important. If any of the steps in the fabrication process result in rough edges or sides, these will act as additional scattering centres in the finished device.

[3] This ΔN^2 dependence only applies for small Δn. It breaks down for larger Δn, see [80].

[4] Strictly speaking, a second order Bragg stack should not show reflection at the design wavelength. However, this is for the $\frac{\lambda}{4}$ condition. If one deviates from this, then a gap opens up at this wavelength.

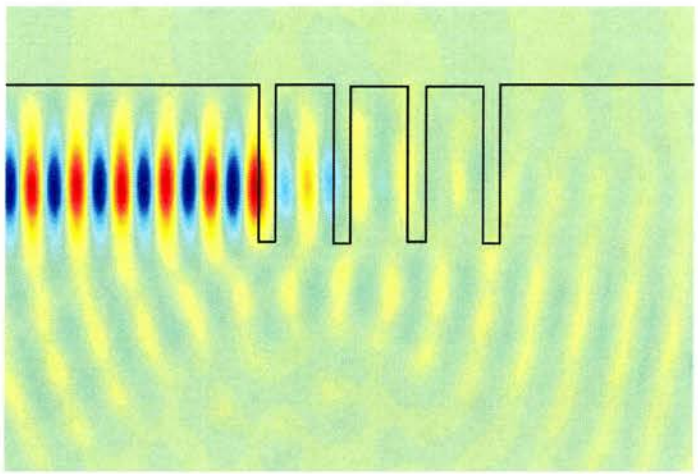

Fig. 3.2: An FDTD simulation of light reflecting from a one dimensional photonic crystal. If features are not etched to a sufficient depth, light may couple to substrate modes thereby dramatically increasing the loss. This effect is clearly visible in the figure.

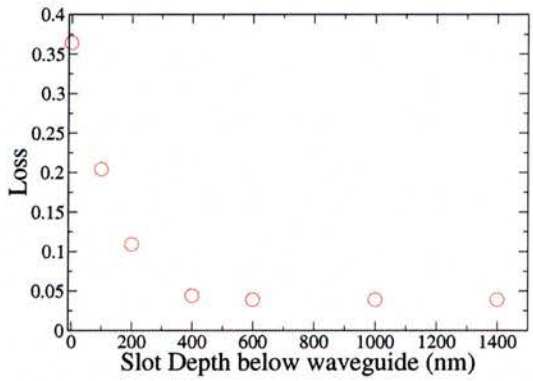

Fig. 3.3: The dependence of the loss on the depth to which the slots are etched below the waveguide. The loss is defined as (1-T-R, where T is the transmitted light and R the reflected). For this simulation, (FDTD), a 4 period grating with 100 nm wide slots and 500 nm period was used at a wavelength of 1000nm. The remaining loss is due to diffraction. (The waveguide consisted of a 200nm GaAs core with 400nm of $Al_{0.6}GaAs$ top cladding and 1.5μm $Al_{0.6}GaAs$ bottom cladding.)

3.3 Electron Beam Writing

ELECTRON beam lithography was developed in the 1960s. Early machines were conversions from Scanning Electron Microscopes. At the simplest level, the electron beam is created and controlled in the column and directly underneath, in the main chamber, the sample is mounted on a laser controlled translation stage, see figure 3.4. A complex set of control electronics is then used to focus, align and blank the beam, as well as move the stage.

The quest for high resolution and high throughput has led to the development of expensive and extremely complex purpose built systems such as the LEICA EBPG-5 and EBPG-6

(costing in the region of £2-3,000,000). However, for typical small scale research requirements, the converted SEM design of old is often more appropriate. Most of the work for this thesis was carried out using a hybrid LEO 1530 SEM/ RAITH Elphy Plus Nanolithography system, (while occasional use was made of the specialised LEICA EBPG-5 system at the University of Glasgow).

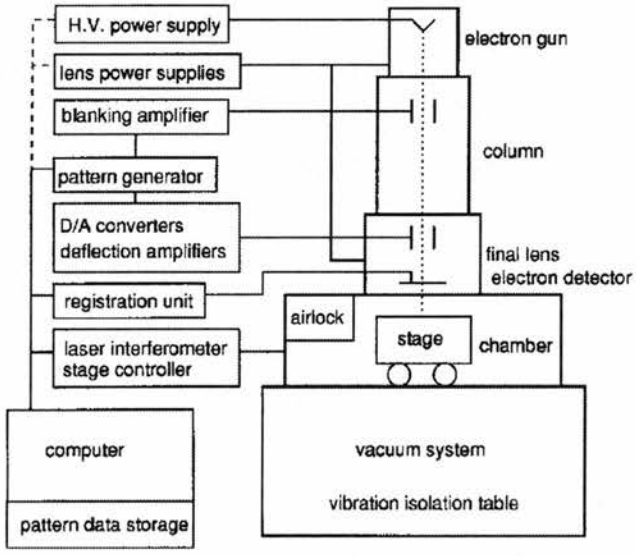

Fig. 3.4: The major components of a electron beam lithography system. The electron beam is generated in the column. It then passes through a series of magnetic lenses which focus and steer the beam. The sample stage is controlled by a laser interferometer which facilitates positioning with an error of approx 40nm.

3.3.1 Electron Beam Resists

FIGURE 3.5 shows the operation of positive and negative resists. For a high resolution resist it is desirable that its thickness should change abruptly for a certain applied dose. Also, as in electron beam lithography, it is desirable to minimise the area that must be exposed in order to minimise the writing time, it is, therefore, preferable to create holes using a positive resist and pillars with negative resists.

Shortly after its development, Polymethyl Methacrylate (PMMA) became the workhorse of electron beam lithography and has remained the most commonly used resist ever since. It is a positive resist with excellent resolution properties, down to 10 nm, [83][5]. Its primary drawback is poor etch resistance. This necessitates the use of a secondary mask for the creation of Photonic crystals.

The polymer SU-8 may also be used as an electron beam resist. It acts negatively, see figure 3.5b. At St. Andrews, it is being used as a mask to create Photonic crystals of the "peg"type. These consist of high index columns in an air background rather than

[5] In my experience, it has possible to create 40 nm wide lines in PMMA, better is possible if metal films (usually Aluminium) are deposited on to the resist to promote charge dissipation. (The aluminium must be removed in Phosphoric acid prior to development.)

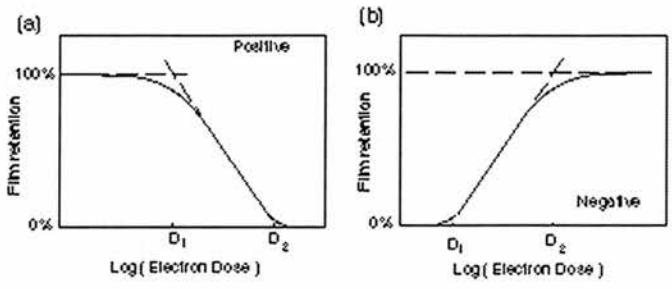

Fig. 3.5: This shows how the film thickness varies with exposure dose a) for a positive resist b) for a negative resist.. As large a slope as possible is desirable. Reproduced from [84].

the more common air holes in a high index background. It has a good etch resistance as well as excellent insulation properties. This thesis makes no use of it directly to produce Photonic crystal features as writing inverse patterns results in excessive write times (it also has poorer resolution compared to PMMA). However, it was on occasion used to define laser ridge waveguides and was extensively used for contact insulation.

At the time of writing, Hydrogen Silsesquioxane is the ultimate resist in terms of resolution (it also has excellent toughness). It has been used by Lister *et al.* to create the smallest grating yet- 12.5nm with a period of 25nm [85]. Like SU-8 it is a negative resist which results in excessively long write times to create the type of feature we work with in this thesis.

3.3.2 Pattern Definition

USING electron beam lithography, the pattern is written in a PMMA resist. Under the influence of the high energy electrons, the polymer chains of the PMMA are broken. Electrons interact with the resist in two chief mechanisms- forward scattering and backward scattering. Forward scattering is relatively inelastic and the course of the electron is changed by only a few degrees. Backward scattering occurs less frequently and the electron may be scattered through much larger angles (as the name suggests). For an acceleration voltage of 30 keV, a dose of electrons on the order of 120 μA cm^{-2} is required to completely remove the resist[6]. The exposed areas can then be dissolved in a suitable developer.

There are a number of possible methods of writing the desired features, see figure 3.6. The most straightforward method is to write the air-slots as they are desired, e.g. expose a discrete set of points which combine to form a 100nm wide box. However, in general, a process bias results in a box which is approximately 20-30nm larger than designed. If sub-100nm features are required, then single pixel lines are a more reliable method. All the energy is deposited in a single line which then overexposes to a 50-100nm width depending on the dose. We have found that under our conditions the box approach produces features only slightly less than 100 nm (using a box width of 70-80nm in the design) whereas single pixel lines can comfortably reach 70 nm, see table 3.2 and figure 3.7. Using more sophisticated techniques such as metal coatings for charge dissipation, better results can, of course, be

[6] It should be noted that this figure is for large features, for Photonic Crystals a larger dose is necessary as there is less additional exposure due to backscattered electrons.

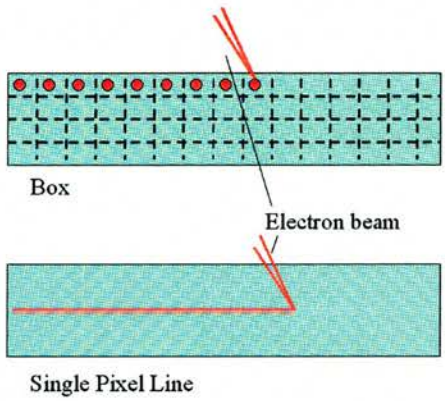

Fig. 3.6: The two approaches to writing a narrow line. The "box" method breaks the feature into a grid (with the spacing given by the step size). Each grid square is then given an individual exposure. With the "single pixel line" method, the feature is written as a single line of pixels.

Dose (μCm^{-2})	80nm Box	60nm Box	40nm Box
410	210	190	160
340	175	165	155
260	145	118	103
220	140	112	98
190	124	100	X
150	95	X	X

Tab. 3.2: This table shows how the actual line width (nm) varies with different doses and design widths. X indicates doses which are insufficient to cause full removal of the PMMA.

achieved. However, single pixel lines are incompatible with proximity correction software. For simple devices experience and comparison with similar box structures are sufficient, however more complicated designs require the box approach.

3.3.3 Pattern transfer

PMMA IS not very resistant physically, forcing the use of an additional step in order to transfer the photonic crystal pattern into the semiconductor, see figure 3.1. Therefore, first of all, a layer of silica (typically 200 nm thick) is sputtered on the sample using Plasma Enhanced Vapour Chemical Deposition (PECVD). A layer of PMMA is then spun on (typically 200-300 nm thick) and the pattern defined using an electron beam writer. The pattern must then be transferred into the silica mask using Reactive Ion Etching. The selectivity between the silica mask and the semiconductor is sufficiently high to allow the creation of the desired PhC feature, using either RIE or CAIBE.

RIE is, at this point in time, a very well understood process, and as a result is often overshadowed by the very involved pattern definition process and the exotic etching techniques (CAIBE, ICP). However, it continues to be of critical importance in the overall process and failures at this stage contribute to sidewall roughness and reduce the time for which a mask may be etched.

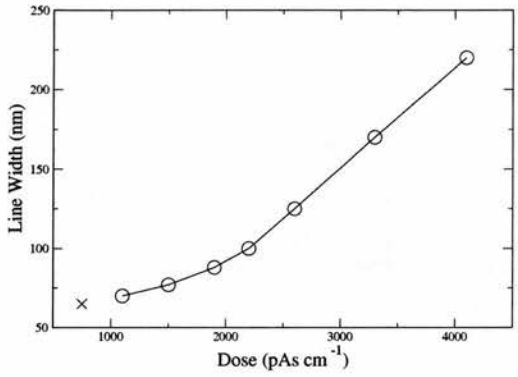

Fig. 3.7: The actual width of single pixel lines as a function of dose. This is the preferred method to create the desired air slots.

3.4 Proximity Correction

3.4.1 Causes

WHEN WRITING the desired pattern using the electron beam, areas of PMMA adjacent to the pattern may unavoidably receive a dose of electrons chiefly through backward scattered electrons (although forward scattering still has an effect).

In figure 3.8, we see a pattern in which the applied proximity effect is incorrect. The holes next to the input waveguides have become over-exposed and are on the verge of linking up, whereas the holes at the edges, particularly at the corners, have not received a sufficient dose. When the correction is right, the edge holes are given a higher dose and those adjacent to the waveguides receive less. [7]

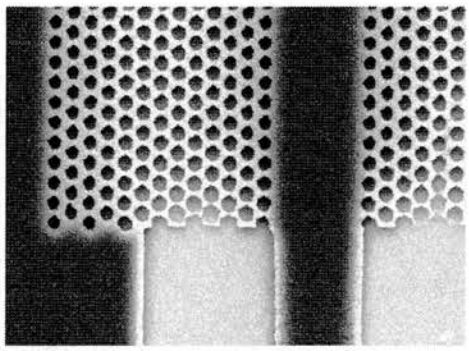

Fig. 3.8: The effects of proximity have not been correctly accounted for in this pattern. The holes beside the access waveguides have become enlarged. The doses for these holes should be reduced.

[7] The photonic crystals used in the thesis are one dimensional, unlike those shown in this section. The effects of proximity are more dramatic and critical in the case of two dimensional crystals, making it easier to determine whether the correction is working. For this reason, experimentally (and for demonstration purposes here) most of the trial proximity correction was done on 2-D PhCs.

The dose at a particular position is a combination of the dose at all positions, though of course, the further away the area, the smaller the contribution. This is known as the proximity effect, and, if left uncorrected, may seriously distort the pattern. To calculate the total dose at a given point i of the design, the pattern is broken into m areas and the contribution of each section to the dose at i is calculated. The absorbed dose at point r_i may be described by:

$$D(r_i) = \sum_{j=1}^{m} \int_A D_j.p(r_{ij}).dA_j, \tag{3.1}$$

where m is the number of contributing sections, A_j is the area of section j, D_j is the dose applied to section j, r_{ij} is the separation between point i and section j and p_{ij} is dose absorbed at i as a result of that applied to section j, see equation 3.2. To correct for this, the original pattern must be altered. The most commonly used method for this is to alter the dose applied to various portions of the pattern (another method is to the compensate by changing the shape of the pattern). In correcting for proximity, the difference between forward and backward scattering becomes important. The behaviour of electrons in the resist can be examined using Monte-Carlo simulations. At high beam energy, >10 KeV, backward scattering is the dominant process and electrons may be scattered over 1 μm and lead to exposure. The dose as a function of position can be described by the following equation:

$$p(r) = \frac{1}{\pi(1+\eta)} \left(\frac{1}{\alpha^2} e^{-\frac{r^2}{\alpha^2}} + \frac{\eta}{\beta^2} e^{-\frac{r^2}{\beta^2}} \right), \tag{3.2}$$

where α is the range of forward scattering, β is the range of backward scattering and η is ratio of the integrated proximity effect of forward scattered electrons to that of backward scattered electrons. The parameter η must be introduced as backward scattered electrons travel slower and interact stronger with the polymer.

However, α, β and η are somewhat idiosyncratic and can be different for each particular resist, developer, mask and semiconductor combination and must be determined for each particular situation.

3.4.2 Determination of Parameters

TO DETERMINE the correct parameters for our set of conditions, we use the doughnut method developed by Stevens *et al.* [86]. A set of rings with constant outer radius but with varying inner radii and dose are exposed. Clearly, the resist at the centre of the ring will only be influenced by the proximity effect from the exposure of nearby regions, see figure 3.9. A careful examination of the particular set of doses and inner radii for which the ring centre receives a clearing dose can allow the calculation of the required parameters, using:

$$D = \frac{D_0(1+\eta)}{e^{-\frac{R_1^2}{\alpha^2}} + \eta e^{-\frac{R_1^2}{\beta^2}}} \tag{3.3}$$

where D is the lowest dose at which the centre of the doughnut clears and R_1 is the corresponding design inner radius. D_0, α, β and η are used as fitting parameters. Typical values for GaAs are α = 10nm, β = 1768nm and η = 1.46. Figure 3.10 shows a photonic crystal

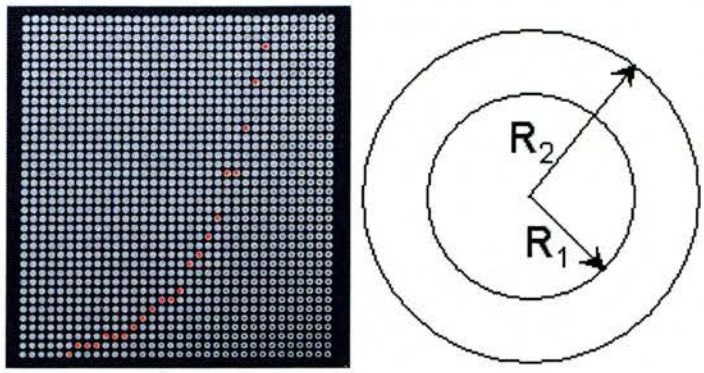

Fig. 3.9: The method used to determine the proximity correction parameters. The inner radius increases along the x-axis and the dose along the y. The particular values of dose and inner radius which just cause the centre of each doughnut to clear are noted (marked in red).

waveguide after proximity correction has been made. The software package modulates the dose across the design according to the inputted α, β and η parameters. It should be noted that increasing the dose applied to a design changes the behaviour of the proximity effect. The margin for error is largest for dose values immediately above the clearing dose.

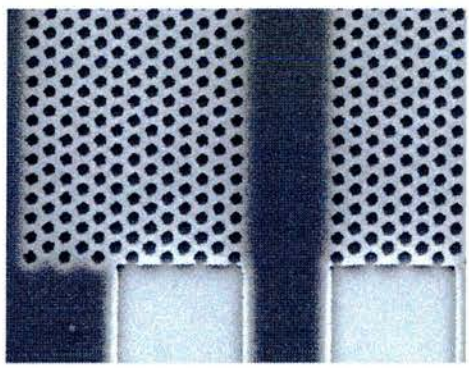

Fig. 3.10: A photonic crystal waveguide with good proximity correction. The critical area is the regions of holes adjacent the input waveguides.

3.5 Chemically Assisted Ion-Beam Etching

CHEMICALLY assisted ion beam etching (CAIBE) is rapidly proving itself to be one of the most successful methods of etching Photonic Crystals. In the early days of PhC fabrication, reactive ion etching was primarily used, however this is limited to producing etch depths on the order of 1 μm. CAIBE has the greater capability as the plasma generation and etching conditions can be varied independently, (in RIE the two are inherently linked). This allows much greater control, enabling etching to depths of approximately 2 μm in GaAs based material and approximately 5.5 μm in InP based [87]. Recently another technique, inductively coupling plasma etching (ICP), has started showing promising results, [82]. All

the photonic crystals used in this thesis were etched using CAIBE in St. Andrews.

3.5.1 Basics of CAIBE

Physical Description

CAIBE, as its name suggests, involves the combination of physical and chemical etching. The sample is placed into the vacuum chamber, and chlorine is pumped in. From above a beam of high energy Argon ions is accelerated toward it.

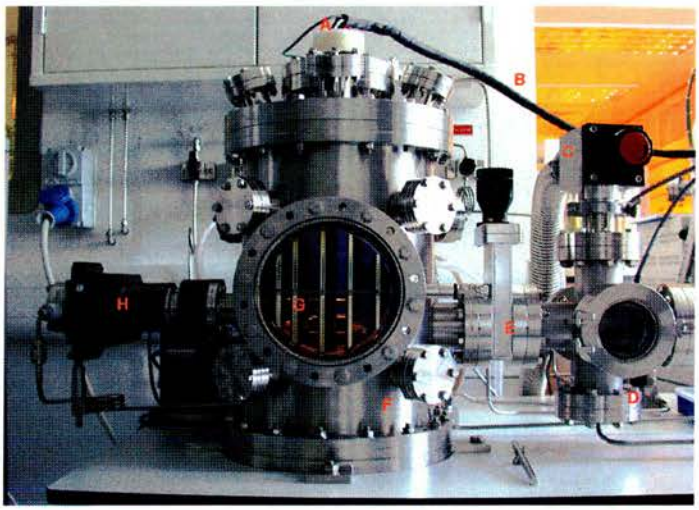

Fig. 3.11: The St. Andrews Chemically Assisted Ion Beam Etching system. A: Ion gun, B: Cable to Ion Beam Controller, C: Valve to Backing Pump, D: Exchange Chamber, E: Gate Valve, F: Main Chamber, G: Heater (inside Main Chamber) and H: Translation stage assembly for Chlorine Ring.

Figure 3.11 shows the CAIBE system used. Toward the top of the picture, at point A, the ion gun may be seen. Simply speaking, it consists of a discharge chamber in which the argon is ionised. The ions are then extracted from this chamber and accelerated through the beam voltage. A set of magnets collimates and focuses the beam. A neutralising filament is also present that may be used to inject electrons into the beam. Thus the sample is hit with a neutral beam, preventing charging, which may deflect ions reducing the incident ion intensity. This is connected to a ion beam controller through the cable at B. The main chamber (F) is kept under vacuum using a high speed turbopump. This must always be kept running requiring the use of a separate exchange chamber.

Samples are mounted on a sample holder and loaded into the exchange chamber (D) which is then evacuated independently by a backing pump (through the valve seen at point C). Just out of picture to the right is a loading arm which is used to the transfer the sample holder between the chambers. A gate valve (E) isolates the main chamber. At G, a heater is used to heat the sample holder to desired temperature. Just above, chlorine is injected through a ring (see figure 3.12 for a closer view). The position of the ring may be adjusted using the translation stage assembly at H.

Operation of CAIBE

THE REGIONS of GaAs exposed through the mask react with the chlorine according to the following equations [88]:

$$GaAs_{(s)} + 2Cl_{2(g)} \rightarrow GaCl_{2(s)} + AsCl_{2(s)} \tag{3.4}$$

$$GaCl_{2(s)} + AsCl_{2(s)} + Cl_2 \rightarrow AsCl_{s(g)} + GaCl_{3(s)} \tag{3.5}$$

$$GaCl_{3(s)} \rightarrow GaCl_{3(g)} + free \quad surface \quad site \tag{3.6}$$

In the absence of the ion beam this reaction takes place very slowly (nm/min). The ion flux supplies additional energy resulting in very rapid, very localised etching of the exposed regions (100s nm/min). This has the potential to create very high aspect ratio features as only the bottom of the hole is exposed to ions and, hence, the very high etch rate. Typically, the sample is also heated to a temperature of 100-150^{o}C. This increases the volatility of the produced species as well as accelerating the rate of reaction.

In order to achieve the holes with vertical sidewalls, the effects of the chemical and physical components must be careful balanced. If the chemical component (determined by the chlorine flow and sample temperature) is dominant, there is a strong anisotropic etch causing the sidewalls to bulge outwards, see figure 3.13. This is detrimental to the performance of the PhC, and may in extreme cases lead to the complete collapse of the PhC (very common when it occurs in combination with poor proximity correction). In the case of a dominant physical component (controlled by beam voltage and current) there is insufficient sideways etching and poor removal of sputtered material. This leads to a narrowing of the hole with increasing depth. While this is not as serious a fault as excessive chemical etching, it greatly reduces the etch rate. Figure 3.14 show etching with a good balance between the two. The resulting walls are almost vertical.

A tapering or narrowing is sometimes observed toward the bottom of the hole, even with

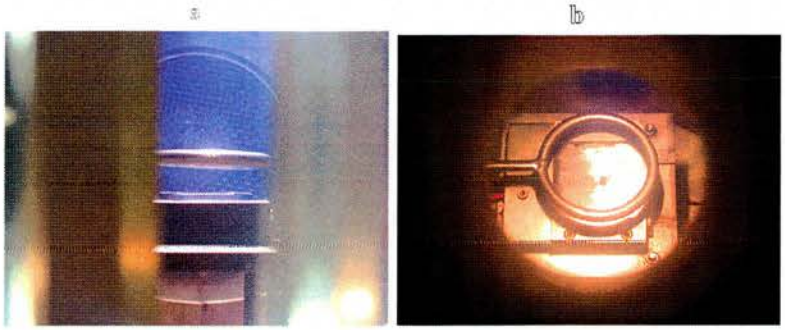

Fig. 3.12: a) A ring is used to inject the chlorine. This ensures that a uniform chlorine pressure is maintained over the sample, this shows up as a blue colour when illuminated by the ion beam. At the rear of the picture, the turbopump may be distinguished. (Bars may be seen in foreground- these form a screen that is usually closed to protect the glass window from corosion.) b) Topview of the chamber while etching. The stage and sample are being illuminated by the beam. Interesting, it is often possible to observe the SiO_2 mask on the sample being etched away as its colour changes with thickness.

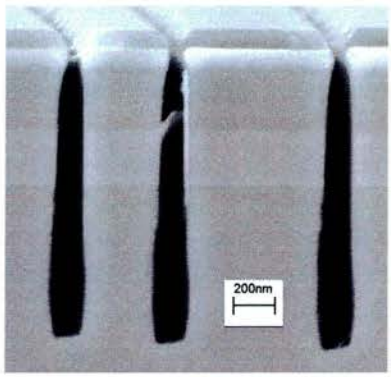

Fig. 3.13: Excessive chemical etching results in the bulging out of the sidewalls. Etched for 8 minutes under conditions of a beam voltage of 1300V, a beam current of 12mA, 4sccm Chlorine flow, 5sccm Argon flow and at a temperature of 150°C. The total etch depth is 1.4 μm. Out of the original 200nm of SiO_2 mask, 95nm remains.

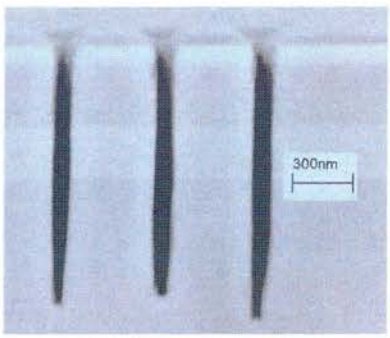

Fig. 3.14: A good balance between physical and chemical etching. The difference between this and figure 3.13 is a 25% reduction in the flow of chlorine.

a good balance, and particularly so when the etch depth is relatively deep (1μm and over). This may be associated with a poor chemical reaction in which the chlorine fails to react fully with sputtered GaAs forming volatile products. It has been found that increasing the sample temperature while reducing the chlorine flow (i.e. holding the net chemical etching constant) cures this problem. In general, a chemical reaction proceeds better at higher temperatures, i.e. it goes more fully to completion and occurs faster. This seems to prefer the formation of volatile products rather than the involatile products which settle at the hole bottoms resulting in narrowing/tapering.

We have attempted to extend this idea further and etch at even higher temperatures. However, it seems that at temperatures in the region of 150 °C, the reaction begins to lose its directionality and the sidewall quality becomes degraded.

3.6 Summary

IN THIS chapter, we have examined the design, definition and etching of one dimensional photonic crystals. We show how to optimise the structure so as to minimise losses. We

discuss the theory and practice of proximity correction and then describe the operation and fundamental techniques of CAIBE. [8]

[8] The FDTD simulations in this chapter were carried out using the model developed by Min Qiu *et al.* [89].

4. LASER FABRICATION

4.1 Overview

THE performance of the finished lasers is crucially dependent on the quality of the fabrication process. Therefore, exquisite care must be taken to ensure that each step of the process achieves the desired result and causes the minimum damage. A step by step description of the laser fabrication process is given in the appendix, see section 10.2. [1]

4.2 Lithography

PHOTOLITHOGRAPHY is one of the fundamental techniques in the fabrication of most semiconductor lasers. However, much experimental work on semiconductor lasers makes use of repeated e-beam writing steps, [90]. A conscious effort was made to minimise the amount of use that was made of the e-beam writer, in order to reduce the demand on our own machine and also with an eye to future mass production (know as "mix and match lithography"). Typically, initial work on new designs was e-beam written, once the design had "stabilised"and initial flaws corrected, a photomask was made up. Only where sub-micron alignment was required (rare in general) was the e-beam writer used as the mainstay.

4.2.1 Photolithography

PHOTOLITHOGRAPHY involves the use of a photosensitive resist. When light of the correct wavelength is incident, the physical properties of the resist changes, see figure 4.1. In the case of a positive resist becoming soluble in another chemical known as the developer. The opposite occurs for a negative resist, i.e. exposure makes it resistant to the developer. Clearly, the light source and resist must be carefully chosen so that there is sufficient intensity of light in the correct wavelength range to break chemical bonds in the resist.

In order to expose the desired pattern, a mask is used. This consists of a glass plate, one side of which is coated in metal (chrome in our case) into which the required pattern had previously between transferred using e-beam lithography and a wet or dry chemical etch. To prevent a loss of resolution due to diffraction, the metal mask must be placed in close proximity to the resist.

To define the waveguides, a single layer of resist is used that also serves as the etch mask. For the contact windows, a bilayer resist must be used. The first of the layers consists of a non photo-reactive resist that is spun on before the normal photoreactive polymer. During development, this resist develops quicker than the normal resist, creating an undercut, see

[1] The work described here was carried out in conjunction with Donald Brown and Simon-Cran McGreehin.

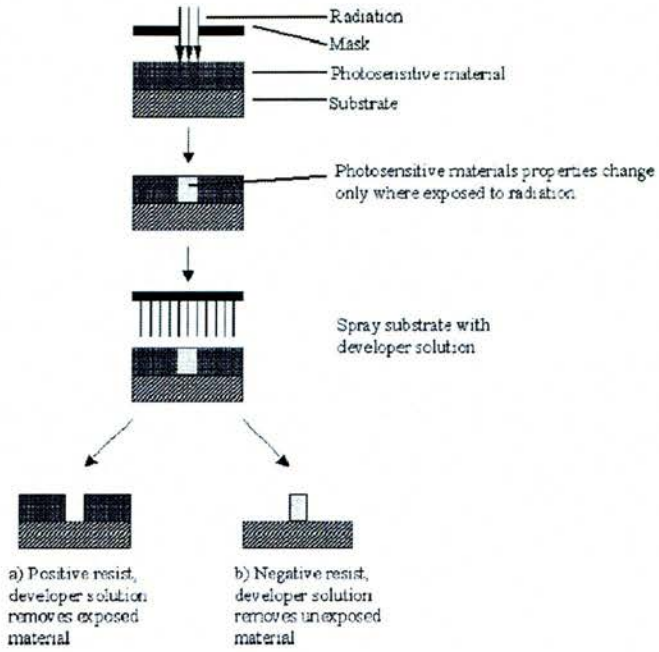

Fig. 4.1: The pattern is transferred from the mask to the photoresist by UV light, a) positive resist, b) negative resist.

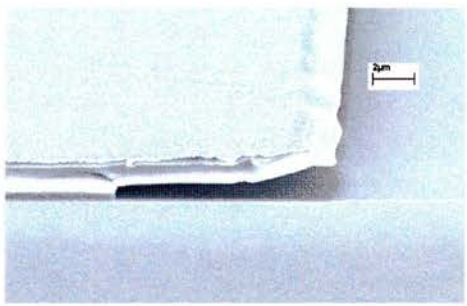

Fig. 4.2: An example of a bilayer resist for liftoff (somewhat extreme). The narrow dark layer near the substrate is the non-photoreactive resist. A 20nm Nickel layer was deposited in order to enhance the image quality through dissipation of charge. During the fabrication of lasers, a thicker metal contact layer is deposited than that shown here.

figure 4.2. After the contact deposition, this undercut allows the removal of metal from regions of the sample where it is not required.

4.2.2 Electron Beam Lithography

ELECTRON beam lithography is an ideal process for the creation of prototype (often one-off) devices. In our case, many of such devices required high precision alignment between processing steps. To facilitate accurate positioning, highly visible alignment marks are created in the first processing step. In subsequent steps, the nanolithography software defines the working area according to these marks. Figure 4.3 shows a possible alignment mark.

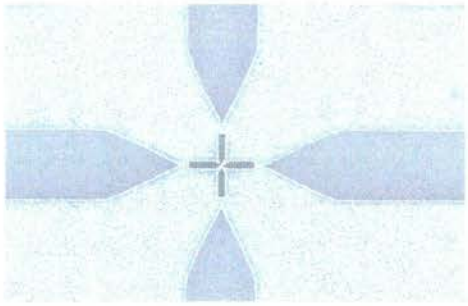

Fig. 4.3: An alignment mark suitable for multi-level alignment. There is a large cross to increase visibility and then a smaller cross for high precision alignment.

A number of considerations should be kept in mind when designing and using such marks. They should be highly visible, especially as contrast can be lost when viewing through a layer of resist, and have features which may be localised to a high degree, i.e. have very sharp points. There should be a number of copies as subsequent etching steps may destroy marks. When carrying out the alignment procedure, widely spaced marks should be used. Finally, when searching for the marks, care should be taken to expose only the region around the mark and not the areas on which the design is to be written.

4.3 Transverse Modes

A COMMON requirement for a laser is operation in a single transverse mode. This allows focusing to the minimum spotsize, and, critically for short pulse production, prevents any beating/interference effects between modes which could prevent modelocking.

The number and type of transverse modes supported by a waveguide is determined by the refractive index of the ridge relative to the the surrounding areas and by the ridge width. The number supported is, typically, proportional to the ridge width and the refractive index step.

Intuitively, a higher order mode requires more "room" than the fundamental mode. Therefore, it is "unhappy" in small waveguides and consequently requires a higher refractive index step to confine it. Therefore, by carefully choosing the ridge height and width, the refractive index step may be made insufficient to confine anything other than the fundamental mode.

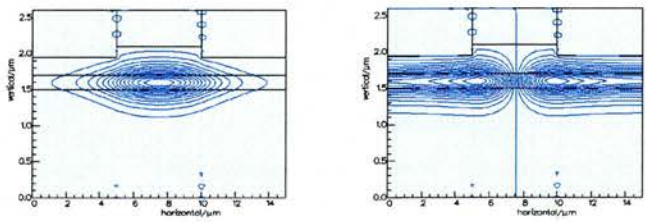

Fig. 4.4: The ridge has a height of 150nm. This is insufficient to confine anything more than the first-order mode. The modes shown in the feature on the right are artificial and confined by the sides of the computational window.

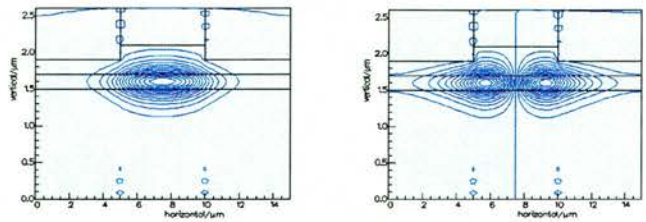

Fig. 4.5: If the ridge height is too large, higher order modes may be confined as the refractive index step is now sufficient to hold the mode in the ridge waveguide.

In figure 4.4 and figure 4.5, we show simulations of 5 μm wide waveguides using a commercial eigenmode solver (FIMMWAVE). In figure 4.4 the ridge height is 150nm and in figure 4.5 the height is 200nm. The fundamental mode is confined for both cases, however the step in figure 4.4 is insufficient to confine the next higher order mode, resulting in a single mode waveguide.

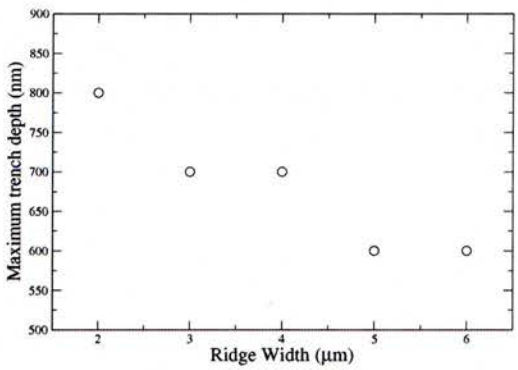

Fig. 4.6: The etch depth at which the device becomes multimoded. (This simulation was carried out with the parameters of the QT1841 material, see figure 4.2).

Figure 4.6 shows this relationship for a number of different ridge widths. As the ridge gets narrower, a greater refractive index contrast is needed to confine the mode. When current is injected into ridge waveguides, carriers may diffuse laterally. This is undesirable as these carriers do not contribute to the useful gain. Thus, in practice, it is preferable to etch as deep as possible (without confining higher order modes) so provide the maximum amount of carrier confinement.

The injection of carriers into the ridge reduces the refractive index somewhat [91]. This means that, in practice, the etched waveguide will be less likely to support higher order modes than the simple eigenmode solver would predict.

4.3.1 Shallow Etching

THE required ridges were created using CAIBE, see section 3.5 for a detailed description of

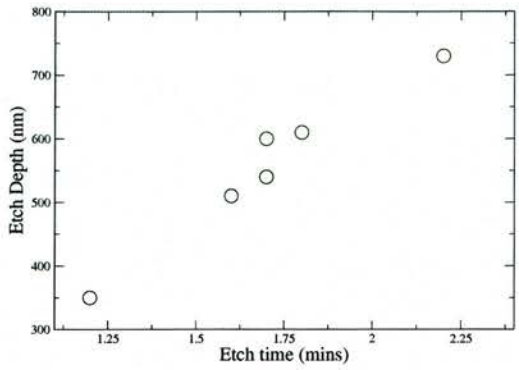

Fig. 4.7: Etching carried out with a beam voltage of 350V, a beam current of 10mA, substrate temperature of 119°C, a chlorine flow of 2 standard cubic centimetres per minute (SCCM) and a chamber pressure of 1.8×10^{-4} mB.

the CAIBE system. CAIBE was primarily designed to deep etch PhCs, and as it turned out, finding conditions which etch shallow depths controllably and repeatably was non-trivial. To controllably define waveguides, a relatively slow repeatable etch rate is desirable. However, two of the obvious means of reducing the etch rate, lower chlorine flow and lower temperature, are unsuitable. Very low chlorine flow rates have the drawback of poor removal of the volatile products and can result in redeposition of material in the form of "grass". Furthermore, under certain values of the chlorine flow and temperature the reaction rate appeared to be temperature limited, which makes for poor repeatability as this is the least controllable parameter.

After some trial and error, the parameters shown in figure 4.7 were chosen. These work well in practice with good repeatability. However, test samples are still needed prior to etching a real device, as the phenomenon of loading may cause irregularities- etching a large area may deplete the reactive gas and thus progress slower than a equivalent etch of a smaller area.

4.4 Contact Insulation

FOR efficient operation of a laser, it is required that the current is injected correctly into the waveguide. A number of different methods of achieving this were examined during this thesis- the use of an oxide aperture, $Ti0_2$ back filling, lithographically defined SU-8 and self aligned SU-8.

Oxide Aperture: To create an oxide aperture, a material which included a layer with a very high Aluminium concentration near the surface was used. When this is oxidised, it becomes insulating. After definition of the waveguide ridges/mesas, the sample is placed in a wet oxidation setup. The high Al percentage layer oxidises rapidly from both sides creating an aperture restricting the flow of carriers to a narrow region in the centre of the waveguide, see figures 4.8 and 4.9. This method suffers from poor repeatability.

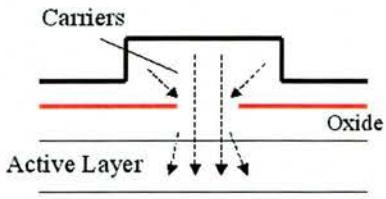

Fig. 4.8: A schematic of an oxide aperture. An insulating layer of oxide is formed at the edges of the ridge that allows carriers to be injected only into the centre of the ridge.

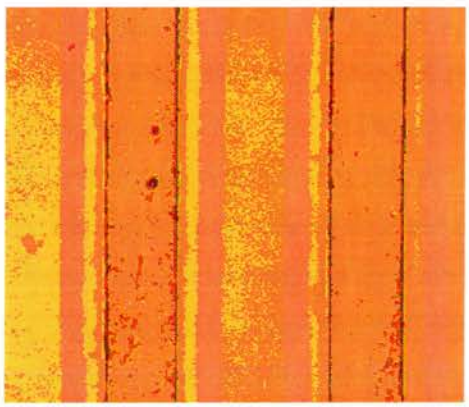

Fig. 4.9: Oxidation of 50 μm wide laser ridges. The dark orange coloured area is the oxide.

$Ti0_2$ back filling: When defining the ridges, a liftoff photoresist is used. After etching the waveguides, a layer of $Ti0_2$ is deposited using an electron beam evaporator, see figure 4.10. The sample is then washed in acetone and all the TiO_2 except that on the trench bottoms is removed. This then acts as insulation and current is injected only into the ridge. The TiO_2 layer is rarely perfect and often contains small holes which degrade its performance as an insulator.

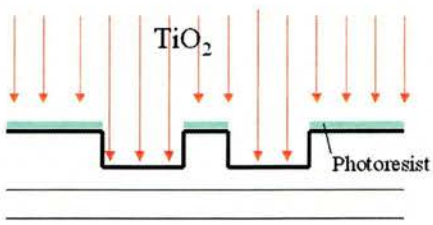

Fig. 4.10: After etching the ridges, Titanium dioxide is deposited using an electron beam evaporator. The sample is then washed in acetone removing all the TiO_2 except that at the bottom of the trenches.

Lithographically defined SU-8: A layer of SU-8 is spun on as normal. It is then

exposed using the same mask as at used to define the waveguides. As SU-8 is negative resist, the regions above the trenches cross-link becoming insulating. After development the sample is usually hard baked at 180^o ensuring that the cross-linking reaction goes to completion, resulting in a 200nm thick film. The only drawback of this method is that highly accurate second stage alignment is required (entailing the use of electron beam writing- SU-8 fortunately also acts as an electron beam resist).

Self-aligned SU-8: A layer of SU-8 is spun onto the sample and then baked at 140^o for 5 minutes. This causes the SU-8 to reflow slightly and surface tension draws most of the polymer off the ridge surface. The sample is then placed in the RIE, and etched slowly (approx. 50nm/min) in an oxygen plasma until the tops of the ridges are free from material. This method is unsuitable for material designs which require very shallow trenches ($\approx$ 200 nm)to define the waveguides as the ridges are not sufficiently prominent for the resist to clear during reflow. The sample may be etched in the oxygen plasma for longer but in this case the quality of the polymer film may be degraded.

The polymer will, of course, reduce the refractive index contrast of the ridge. The refractive index of SU-8 has been measured using ellipsometry to have a refractive index of 1.56 [92]. This helps in the creation of a single mode waveguide, though in general, its effect seems to be small.

The contact windows were defined in a bilayer resist, see figure 4.2. The contacts themselves are deposited using an electron beam evaporator. A complex set of metal layers are used to prevent the formation of rectifying rather than ohmic contact (this occurs naturally when a a simple metal contact is deposited on a semiconductor).

Figure 4.11 shows an SEM image of the end facet of a finished laser.

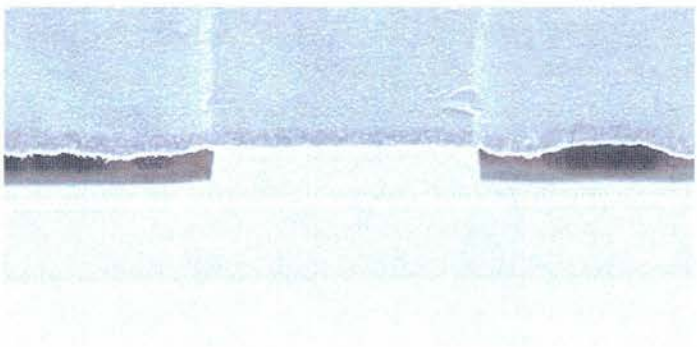

Fig. 4.11: A end view of facet of a finished laser. Note the metal contacts and self aligned insulation.

4.5 Current Spreading

AFTER injection, carriers can diffuse as a result of thermal effects. If the waveguide defining trenches are etched completely through the active layer, then this diffusion is minimised- though problems with sidewall recombination may occur. Clearly the closer the trenches are to the active layer the better, though this is always a problem (only fully solved in broad area lasers, where the current spreading is a negligible fraction of the total, and in buried

heterostructure, lasers where the ridge is etched through without loss of performance). In figure 4.12 we determine the amount of current spreading.

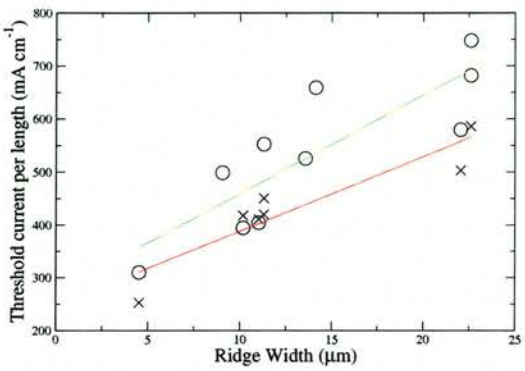

Fig. 4.12: A plot of threshold current per length against laser width. Circles correspond to a length of 740 μm and crosses to 1180 μm. In order to compare the two lasers, we plot the threshold current per length. Within the error, the two curves have the same intercept.

The threshold current density is proportional to the ridge width but due to current spreading, the curve does not go through the origin. By comparing the intercept with the threshold carrier density of a wide (50μm) device, the amount of current spreading may be determined. For the devices shown in figure 4.12, we estimate spreading of approximately 3-4 μm. [2]

4.6 Material Design and Characterisation

4.6.1 Design

A NUMBER of different laser materials were used to create the lasers used in our research. Most were grown at the University of Sheffield by J. S. Roberts using Metal Organic Vapour Phase Epitaxy (MOVPE). This is a technique by which semiconductor crystals are grown by depositing individual layers of atoms. The atoms are transported to the substrate using organic gases, which decompose onto the heated surface of the crystal. Sequences of different layers can be grown, by switching the gases sent to the reactor.

The quantum wells were composed of Indium Gallium Arsenide and situated in a GaAs waveguide. Layers of AlGaAs with high Aluminium content formed the cladding. The wafer was capped with a layer of GaAs which protects the AlGaAs from oxidation (the rate of which is proportional to the aluminium content [93]). A P-N junction is created by P-type doping of the cladding layers (in particular the cap layer to better facilitate current injection from the contacts) and N-type doping of the substrate layers, including the GaAs substrate on which all the epitaxial growth was carried out.

In a photonic crystal device, the etch depth of holes/slots must penetrate sufficiently into the substrate to prevent coupling of light to substrate modes which is one of the major

[2] The lengths of both lasers were chosen to be long enough such that mirror losses have a negligible effect on the current density, see figure 4.14.

sources of loss, [94]. With the finite etch depth achievable with RIE and CAIBE, this problem is minimised by placing the active layer close to the surface, see section 3.2. This idea was used in the design of QT1719 material shown in table 4.1.

Thickness (μm)	Description	Composition and doping
0.1	Cap	GaAs, p+
0.3	Top Cladding	$Al_{0.6}GaAs$, p=8×10^{17}
0.12	Barrier	GaAs
7.5nm	Quantum Well	$In_{0.18}GaAs$
10nm	Barrier	GaAs
7.5nm	Quantum Well	$In_{0.18}GaAs$
0.12	Barrier	GaAs
1	Lower Cladding	$Al_{0.6}GaAs$, n=8×10^{17}
	Substrate	GaAs, n+

Tab. 4.1: The composition of the QT1719 wafer. It consists of two quantum wells in a shallow waveguide (this faciliates the creation of photonic crystals.)

It did, however, have a drawback when used in a two-section configuration. A fundamental requirement of this is good electrical isolation between the two sections, which is usually created using an etched trench, the resistance of which is proportional to its depth. But due to the shallow waveguide design, the trench's depth is very limited. If etched too deep the waveguide is broken and the two sections become optically separate which is undesirable. As a result, two section lasers made from the QT1719 wafer had low isolation between the sections which, in addition, was difficult to repeat reliably.

With recent improvements in CAIBE [87] and the subsequent increase in etch depth, the requirement of a shallow waveguiding layer could be relaxed. In the QT1841 material, the active layer was pushed 400nm deeper, all else was kept the same, see table 4.2. This cleared up the frustrating isolation problem, as well widening the range of depths for which the lateral trenches gave a single mode waveguide. It also proved to be slightly more efficient and powerful than QT1719, presumably as the waveguide has a smaller interaction with any surface imperfections.

Thickness (μm)	Description	Composition and doping
0.1	Cap	GaAs, p+
0.7	Top Cladding	$Al_{0.6}GaAs$, p=8×10^{17}
0.12	Barrier	GaAs
7.5nm	Quantum Well	$In_{0.18}GaAs$
10nm	Barrier	GaAs
7.5nm	Quantum Well	$In_{0.18}GaAs$
0.12	Barrier	GaAs
1	Lower Cladding	$Al_{0.6}GaAs$, n=8×10^{17}
	Substrate	GaAs, n+

Tab. 4.2: The composition of the QT1841 wafer. The only difference between this and the QT1719 design is a deeper active layer.

The QT1041 material had a graded index separate confinement structure (GRINSCH), see table 4.3. We found that this material had performance comparable to the QT1841

material. It had higher gain, though a poorer $\eta_i - \alpha$ product.

Thickness (μm)	Description	Composition and doping
0.1	Cap	GaAs, p+ (Zn)
0.1	Top Cladding	GaAs graded to $Al_{0.41}$, p+ (Zn)
1.2	Top Cladding	$Al_{0.6}GaAs$, p=1.9×10^{18} (Zn)
0.1		graded to $Al_{0.2}GaAs$
0.1		$Al_{0.26}GaAs$
5nm		GaAs
6.5nm	Quantum	$In_{0.2}GaAs$
5nm	Barrier	GaAs
6.5nm	Quantum Well	$In_{0.2}GaAs$
5nm	Barrier	GaAs
0.1		$Al_{0.26}GaAs$
0.1		graded from $Al_{0.2}$ to $Al_{0.41}GaAs$, Si doped
1.5	Bottom Cladding	$Al_{0.41}GaAs$, n=1.4×10^{18} (Si)
0.1	Bottom Cladding	graded to GaAs, Si doped
0.5	Barrier	GaAs, n=1×10^{18} (Si)
	Substrate	GaAs, n+

Tab. 4.3: The composition of the QT1041 wafer. This had a graded index separate confinement heterostructure (GRINSCH).

Broad Gain Quantum Well material

WE ALSO examined the possibility of designing a wafer with a wide gain spectrum. The typical quantum well has a gain bandwidth of approximately 10-20nm. In order to widen this, it would be desirable to use a material incorporating a number of different QWs (each one emitting at a different energy). This is non-trivial, as one of the quantum wells can come to dominate with an ensuing narrow gain spectrum- when emission from one well is high, carriers can fill the resulting vacancies in preference to recombining in a different well.

In a time resolved photoluminescence experiment [95], Frojdh *et al.* show that, as might be expected, the number of wells between the examined well and the excited layer has a strong effect on the resultant photoluminescence (PL). Moreover, their analysis of the results shows that the influence of the various hole parameters dominated that of those of the electrons. Due to the greater effective mass of holes, they have a much shorter diffusion length than that of the electrons and thus hole diffusion becomes the limiting factor. This gives a mechanism to control the emission of one well over another, as holes and electrons are injected from different sides of the active layer. The wells nearest the surface (beside the p-doped layers) therefore see the highest hole concentration and get the "first opportunity" to deplete carriers.

To this end, we designed a material with $3 \times 3nm$ wide InGaAs QWs next to the p-doped material, a 4.5 nm wide well and a 10nm well next to the n-doped material, see table 4.4 for details.

Electroluminescence spectra from a device made from this material with anti-reflection coated facets are shown in figure 4.13. At low pumping wide wells are more effective at

Thickness (μm)	Description	Composition and doping
0.1	Cap	GaAs, p+
0.15	Top Cladding	$Al_{0.6}GaAs$, p=8×10^{17}
0.1	Oxide Aperture	$Al_{0.9}GaAs$, p=8×10^{17}
0.05	Top Cladding	$Al_{0.6}GaAs$, p=8×10^{17}
0.1	Barrier	GaAs
0.01	Strain Relaxation	$GaAsP_{0.06}$
3nm	Quantum Well	$In_{0.18}GaAs$
10nm	Barrier	GaAs
3nm	Quantum Well	$In_{0.18}GaAs$
10nm	Barrier	GaAs
3nm	Quantum Well	$In_{0.18}GaAs$
10nm	Barrier	GaAs
4.5nm	Quantum Well	$In_{0.18}GaAs$
10nm	Barrier	GaAs
10nm	Quantum Well	$In_{0.18}GaAs$
0.01	Strain Relaxation	$GaAsP_{0.06}$
0.1	Barrier	GaAs
0.5	Lower Cladding	$Al_{0.6}GaAs$, n=5×10^{17}
	Substrate	GaAs, n+

Tab. 4.4: The composition of the QT1600 material. This material was also used for oxide aperture experiments, see section 4.4.

capturing carriers than narrow wells (this results from the relative positions of Fermi levels) and only the 10nm well emits strongly at low current. As the current is increased, the narrow wells become active and eventually come to dominate as a result of their favourable positioning. Thus a gain width of approximately 70 nm may be achieved. Such a material is both inhomogeneously (due to the different well sizes) and homogeneously (due to the nature of each individual well) broadened. Quantum dots are broadened by much the same mechanism though on a much greater scale.

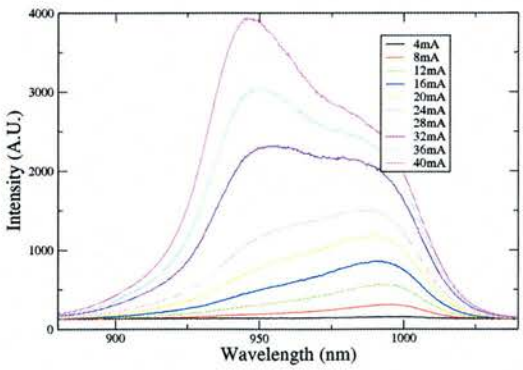

Fig. 4.13: Electroluminescence spectra of a device from the QT1600 wafer. Each curve is taken for different current flowing through the device.

Quantum Dot Materials

THE STRUCTURE of a 10 layer Quantum Dot material, DO451, is shown in table 4.5. In order to make up for the low gain of Quantum Dots, multiple layers are used.

Thickness (μm)	Repeats	Description	Composition and doping
0.1		Cap	GaAs, p=5 × 10^{20}
0.015		Top Cladding	$Al_{0.6}$GaAs, p=3 × 10^{18}
0.4			$Al_{0.6}$GaAs, p=1 × 10^{18}
0.5			$Al_{0.6}$GaAs, p=5 × 10^{17}
0.033	10	Waveguide	GaAs
0.005	10	Barrier	$In_{0.15}$GaAs
0.0008	10	Quantum Dots	InAs
0.033		Waveguide	GaAs
0.5			$Al_{0.35}$GaAs, n=5 × 10^{17}
1		Lower cladding	$Al_{0.35}$GaAs, n=1 × 10^{18}
0.02			GaAs, n=3 × 10^{18}
		Substrate	GaAs, n+

Tab. 4.5: The compostion of the DO451 quantum dot material.

Table 4.6 show the structure of the DO178 quantum dot material. Similarly to the QT1600 material, this has been designed to have a very broad gain spectrum. In addition to the already broad spectrum of a quantum dot layer due to the spread in dot size, a second set of dots with a slightly different size has been added. 5 layers of each Quantum dot size were used in order to increase the gain.

Thickness (μm)	Repeats	Description	Composition and doping
0.1		Cap	GaAs, p=5 × 10^{19}
0.02		Top Cladding	$Al_{0.35}$GaAs, p=3 × 10^{18}
0.7			$Al_{0.35}$GaAs, p=1 × 10^{18}
0.5			$Al_{0.35}$GaAs, p=5 × 10^{17}
0.035	5	Waveguide	GaAs
0.005	5	Barrier	$In_{0.15}$GaAs
0.0007	5	Quantum Dots	InAs
0.035	5		GaAs
0.005	5	Barrier	$In_{0.15}$GaAs
0.0008	5	Quantum Dots	InAs
0.035		Waveguide	GaAs
0.5			$Al_{0.35}$GaAs, n=5 × 10^{17}
1		Lower cladding	$Al_{0.35}$GaAs, n=1 × 10^{18}
0.02			GaAs, n=3 × 10^{18}
		Substrate	GaAs, n+

Tab. 4.6: The compostion of the DO178 quantum dot material. It has 2 different sizes of quantum dots (5 layers of each) deliberately increasing the inhomogeneously broadened spectral bandwidth.

4.6.2 Characterisation of material constants

IN ORDER to compare the performance of different laser wafers, we determines the values

of the optimum gain, g_0 and the internal (optical) loss α_{int} through an examination of the dependence of the threshold current density on the laser length [64]. This technique has advantage in that it requires only the measurement of the threshold current density, a very accessible parameter.

In a stripe laser at threshold, the following equation holds:

$$n_w \Gamma_w g_w = \alpha_{int} + \frac{1}{L} ln \frac{1}{R} \tag{4.1}$$

where Γ_w is the optical confinement to each well, n_w is the number of wells, g_w is the gain per well, α_{int} is the loss, L is the laser length and R is the facet reflectivity, see section 2.3.3 for the derivation of this. g_w can be related to the current density by:

$$\frac{g_w}{g_0} = ln \frac{J_w}{J_0} + 1 \tag{4.2}$$

where g_0 is the gain saturation and J_0 is the current density saturation [64] and J_w is the current density per well. The threshold current density J_{th} is related to J_w by:

$$J_{th} = \frac{n_w J_w}{\eta_i} \tag{4.3}$$

where η_i is the internal quantum efficiency.

Combining equations 4.1, 4.2 and 4.3 and rearranging gives:

$$ln J_{th} = \frac{1}{L} \left(\frac{ln \frac{1}{R}}{n_w \Gamma_w g_0} \right) + \left[\frac{\alpha_i}{n_w \Gamma_w g_0} + ln \frac{J_0 n_w}{\eta_i} - 1 \right] \tag{4.4}$$

where J_0 is given in the literature [96]. Thus from a plot of $\ln J_{th}$ against $\frac{1}{L}$, the values of g_0 and α_{int} may be determined [3].

Table 4.7 gives a summary of the characteristics of the different wafers used. J_∞ is the threshold current density of an infinitely long device, i.e. no mirror losses. The QT1600 material shows a lower gain than the QT1841 due to its more complicated structure. When lasing, some of the wells cannot make a contribution, (due to their wide spread) and lose carriers through spontaneous emission. It has a lower J_∞ value, presumably because at its lasing wavelength only the largest well is active and thus a population inversion may be achieved at lower pumping. However, as a result of the low gain, relatively long devices are necessary to overcome the mirror losses.

As might be expected, an infinitely long laser made from the quantum dot material has the lowest threshold current density. This is consequence of the lower gain of quantum dots (shown by the low G_0 value), thus there are less states to invert in order to achieve a population inversion and lasing starts for lower pumping. One can see from figure 4.14, that for this quantum well material, a laser length of approximately 600 μm is sufficient for mirror losses to become negligible compared with the waveguide losses. The equivalent length for DO178 is 1750 μm. This value is also on the order of 1500μm for DO451, in spite of it having a superior G_0 value to QT1841. Due to its low confinement factor, it does

[3] A careful examination of equations 4.3 and 4.4 will show that α_{int} and η_i may not be determined independently. Following [97], we assume η_i to be 0.8.

	J_∞ (A cm^{-2})	G_0cm^{-1}	α (cm^{-1})	Confinement Factor
QT1719	146	1294	3.7	0.05
QT1841	180	920	6.7	0.05
QT1041	212	1013	16.5	0.05
QT1600	120	540	8	0.03
DO451	83	1235		0.016
DO178	44	466		0.013

Tab. 4.7: A summary of the characteristics of the materials tested in this thesis.

not use this gain as well resulting in this long length. Thus, when fabricating quantum dot lasers with as cleaved facets the cavity should be chosen to be relatively long.[4]

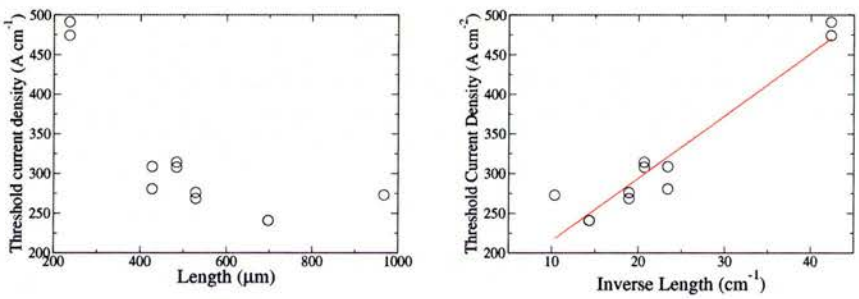

Fig. 4.14: Plot of J_{th} against length on the left and against inverse length on the right. As the laser gets shorter, the effect of mirror losses becomes large relative to the waveguide loss, increasing the threshold current density. The gain parameter may be determined from the slope of the natural logarithm of the threshold current density against inverse length ($ln(J_{th})$vs$1/L$).

Theoretically, this may be achieved through an analysis of the slope efficiency above threshold of lasers of varying length. However, this method requires a very accurate measurement of *all* the light emitted by the laser. In agreement with [90], we found this to be very prone to experimental error.

4.7 Laser Performance

USING the techniques and materials discussed in this chapter, it has been possible to create single mode semiconductor lasers of high quality, see figure 4.15. The technique of shallow etching reliably gives a laser that operates in a single transverse mode. The method of self alligned SU8 insulation allows the injection of current into the laser rigde, while etching as deep as possible (while keeping a single mode) maximises the amount of carriers which contribute to the useful gain. This basic laser designe has been used with success for other

[4] For these calculations, I have assumed that a layer of quantum dots is equivalent to a quantum well and used the resulting value for the confinement factor. This is incorrect as only a fraction of the layer is actually quantum dots. Thus, the gain per dot is higher but the confinement per dot is lower. However, in practice it is the product ΓG that is important for a laser's performance and therefore this is a valid approximation. This is also the reason for the omission of the quantum dot α parameter in table 4.7. A more sophisticated experiment is necessary to extract this parameter.

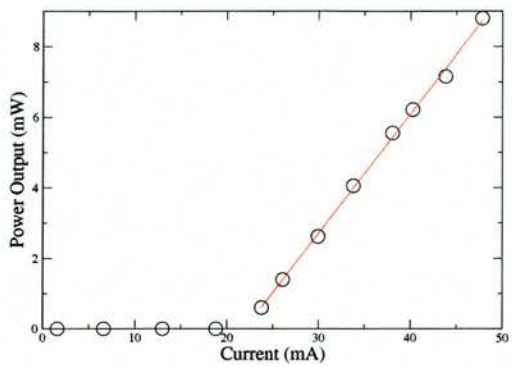

Fig. 4.15: A power-current curve of a single mode laser. Above threshold, the slope is 0.33W A^{-1}. (The output was taken from a single facet).

devices and applications [98] [99].

4.8 Photonic Crystals

PHOTONIC crystal mirrors may be integrated quite easily into these lasers. Following the procedure of chapter 3.5, the desired photonic crystal features are defined and etched. After the CAIBE step, there will typically be thin layer of SiO_2 covering the sample- this must be removed using Hydrofluoric acid, as it is insulating.

As the etched features are small in size, they do not cause discontinuities when the various resists are spin coated. Thus, laser fabrication may continue as normal.

However, care must be taken when depositing the contacts. Any metal that finds its way into the photonic crystal will cause additional loss. This, sometimes, necessitates the use of three point alignment with the electron beam writer so that contact windows are placed with the desired accuracy.

We found that it was possible to create lasers with one PhC mirror which showed slightly less than twice the slope efficiency than that of a laser with as cleaved facets (the output was taken from a single facet). This shows that the use of a photonic crystal mirror did not seriously degrade the performance of the laser.

4.9 Summary

WE HAVE designed and fabricated lasers that operate in a single mode with high slope efficiencies. In practice, due to the high powers necessary for autocorrelations and the extra loss due to the incorporation of a reverse biased saturable absorber section, this is a prerequisite for the creation of modelocked laser diodes.

Part II

RESULTS

5. ADVANCED FABRICATION

IN THIS chapter, we describe some new fabrication techniques developed over the course of this thesis. This work was carried in conjunction with Maria Kotlyar and Rab Wilson of the University of St Andrews.

5.1 High Voltage Low Current CAIBE

FIRST, WE discuss a new development in Chemically Assisted Ion Beam Etching. CAIBE is usually carried out with high beam currents (30 mA) and relatively low beam voltages (300-1000 V). We have found that by using a larger beam current-beam voltage ratio, a significant improvement in etching can be achieved.

5.1.1 Balanced Etching

AS MENTIONED previously, chapter 3.1, in order to achieve balanced etching (vertical sidewalls), the physical etching components, controlled by the beam current and beam voltage, must be carefully matched to the chemical components, controlled by the chlorine flow and substrate temperature. There is a wide range of current-voltage combinations that give the same total amount of physical etching. In fact, we have found that this occurs for voltage-current combinations which correspond to an approximately constant total beam power, see figure 5.1.

The ion flux serves to accelerate the GaAs-Chlorine reaction. There are two ways in which this is acceleration may be considered. First, the chlorine "softens" the GaAs, the ions then sputter atoms/particles of semiconductor which then react with the chlorine forming gaseous products. Second, the ions impact upon the GaAs transferring their energy into heating the semiconductor, the chemical reaction with the chlorine then proceeds faster in the locality of the impact. Essentially, this is a consideration of whether the beam energy or the beam momentum is the decisive factor.

The ion gun gives each ion a kinetic energy according to:

$$E = \frac{1}{2}mv^2 = eV \tag{5.1}$$

where E is the energy, m is the ion mass, v is the ion velocity, e is the charge on the ion, and V is the accelerating voltage. Rearranging gives a square root dependence of the momentum on the voltage:

$$mv = \sqrt{2me}\sqrt{V} \tag{5.2}$$

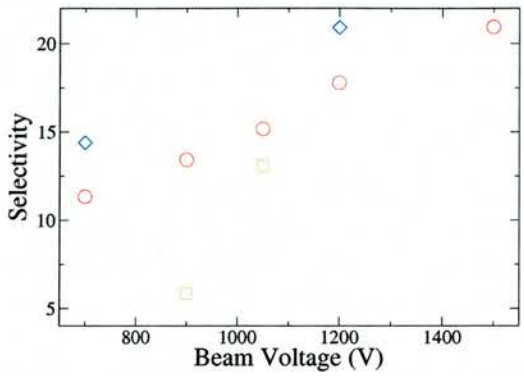

Fig. 5.1: Balanced etching occurs for a constant beam power (red circles). The selectivity also increases with increasing voltage. The blue diamonds correspond to chemical overetching (through an increase in substrate temperature or chlorine flow). The green squares are physically overetched features (through an increase in the beam current). The selectivity has a strong dependence on the amount of chemical etching.

Comparing equations 5.1 and 5.2, we note that the slope of figure 5.1 is linear. This suggests that equation 5.1, the energy argument, better describes the physical process. If the momentum argument, equation 5.2, held, then a sub-linear slope would be expected.

Thus, if balanced etching is obtained for particular values of the beam current and voltage, then a balance may be found for all values which give the same current-voltage product (at least in the voltage range examined here- 750-1500V). This is a subtle point, but it gives an additional degree of freedom to reduce edge roughness.

5.1.2 Selectivity

THE RELATIONSHIP between balanced etching and beam power is also accompanied by a somewhat less well understood phenomenon. Figure 5.2 shows the curious relationship between the silica mask etch rate and the beam voltage (the current was held constant). Contrary to what might initially be expected, the etch rate decreases with increasing voltage. This may be explained as a hardening or compression of the mask under the action of the high energy ions. It has also been observed that silica, following high energy ion bombardment, is more resistant to RIE than would otherwise be expected [100].

This increased etch resistance may be exploited to achieve greater etch depths, as when the etching is correctly balanced, the chief limiting factor then becomes the etch rate of the mask relative to that of the semiconductor, known as the mask/material selectivity.This dependence of the selectivity is shown in figure 5.3.

A potential drawback of this regime of operation is the risk of increased sidewall roughness due to the increased ion energy. However, this effect may be counteracted by the large amount of chemical etching per ion impact (known as the ion-induced chemical etching yield). When a high energy ion strikes, it causes physical sputtering which removes material as well as causing physical damage. The amount of damage will be proportional to the

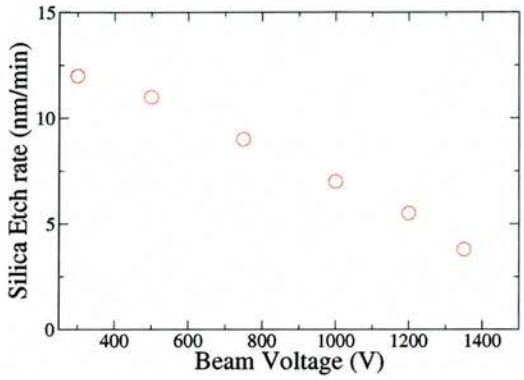

Fig. 5.2: The silica etch rate decreases with increasing voltage. From [87].

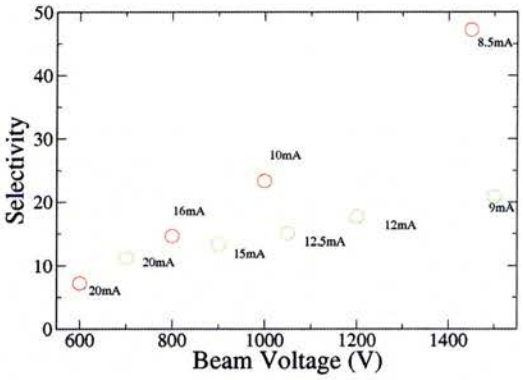

Fig. 5.3: The dependence of the selectivity on the beam voltage-current. From [87].

energy. However, the impact will also cause heating in the vicinity of the impact. The chemical reaction between semiconductor and chlorine will be accelerated in this region and, we believe, largely remove the damage that had just been caused by the impact. This idea agrees qualitatively with results of Daleiden *et al.* [101]. They have shown that the chemical reaction with chlorine results in a reduction in the damage caused by the ion beam. An examination of the sidewalls of devices etched under these conditions shows no increase in roughness relative to those etched at lower voltages, see figure 5.4[1].

This method allows the etching of photonic crystals in GaAs of very high quality. Furthermore, the related advances in InP etching, [102], has the consequence that the techniques developed in this thesis can be readily extended to InP- based devices operating in the important 1.3 μm and 1.55 μm wavelength ranges.

[1] The prediction of increased sidewall roughness follows largely from the momentum argument of section 5.1.1. The absence of increased roughness is additional evidence for the energy argument discussed earlier.

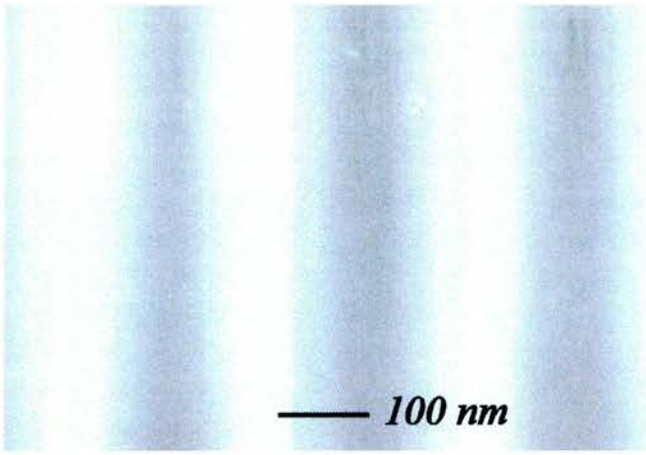

Fig. 5.4: A photonic crystal etched using a low beam current high beam voltage beam. The very low level of sidewall roughness is evident.

5.2 Hydrogen Silsesquioxane Masking

THE CREATION of Photonic Crystal devices invariably requires four processes- hard mask deposition (typically SiO_2 or SiN_x deposited using plasma enhanced chemical vapor deposition (PEVCD)), pattern definition (typically in polymethylmethacrylate (PMMA) using electron beam lithography), pattern transfer into the hard mask (usually by reactive ion etching (RIE) with fluorine chemistry) and finally the deep etch (using RIE, chemically assisted ion beam etching (CAIBE) or inductively coupled plasma etching (ICP)), see chapter 3. Each of these steps is a complex process requiring expensive machinery. Any simplification of this process offers significant advantages in both versatility and cost, particularly for the relatively small-scale production typical in research institutes.

For active photonic crystal devices, carrier injection is one of the most convenient means to achieve tuning, and is widely used [91],[102]. Through the effects of bandfilling, bandgap shrinkage, and free-carrier absorption (plasma effect), the refractive index changes with the injection of carriers. Importantly though, this electro-optic change in the refractive index is of the opposite sign to that caused by the thermo-optic effect. Thus, any heating resulting from the injection of current counteracts this, reducing or removing the desired effect. Therefore, in tunable devices it is vital that the thermal resistance is kept as low as possible [103].

Semiconductor lasers incorporating photonic crystal mirrors and other deeply etched features (also requiring hard masking) have potential for enhanced tunability [98] and mode control. As the performance of a laser strongly depends on the operating temperature (particularly in high power applications), it is also important to minimize all sources of heating in these devices. The PEVCD process used for the hard mask deposition usually results in damage to the surface of the material. This damage increases the electrical resistance of the finished device and generates additional heating during operation.

In this section we look at a method of masking that does not involve plasma deposition. The method proceeds as follows: first, the sample is coated with a spin-on glass (Hydrogen

Silsesquioxane), it is then cured at high temperature (300-500°C) to produce a silica film. This method has a number of advantages over PEVCD deposited silica.

5.2.1 Background

THE ORIGINAL use of Hydrogen Silsesquioxane was as a low K-dielectric (low epsilon) [104] for use in producing faster and more efficient semiconductor devices in the Integrated Circuit industry. It has also found application as an electron beam resist [105], where it has enjoyed considerable success in this field, producing the highest resolution features to date [105], [106]. As far as the molecular structure is concerned, Fourier transform infrared spectroscopy has shown that Hydrogen Silsequioxane consists of molecular network of H-Si-O bonds [107]. As might be expected, the nature of this structure has a strong influence on its physical properties. Depending on the curing temperature, it may have a cage structure (low temperature) or network structure (when the temperature is sufficient to start dissociating the Si-H bonds), see figure 5.5. The ratio of Si-O to Si-H bonds has been shown to be the critical factor governing the mechanical hardness, with the hardness increasing with increasing Si-O fraction. This ratio, in turn, is proportional to the curing temperature [108]. At sufficiently high temperatures, 500-600°C, all of the Si-H bonds will be converted and the hardness of the film will saturate.

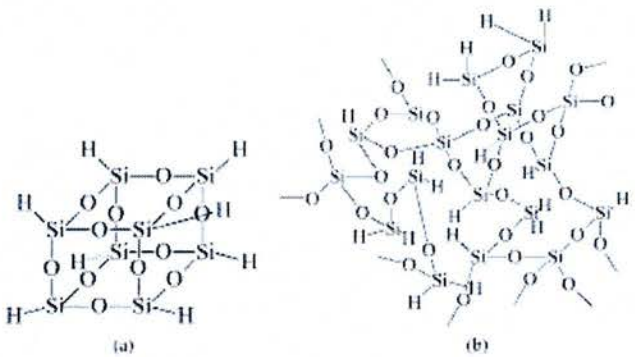

Fig. 5.5: At low temperature HSQ has a cage structure (a), heating at high temperature in the presence of oxygen results in a change to a network structure (b). Reproduced from [109].

5.2.2 Procedure

WHEN HYDROGEN Silsesquioxane is used as a negative e-beam resist, it is spun as normal and baked at a temperature of 220°C. We use a commercially available HSQ resist, (Fox-12, Flowable Oxide from Dow Corning). Multiple layers may be used to build up a film of the desired thickness. Electron beam exposure results in a chemical reaction creating SiO_2 in the exposed region. The unexposed HSQ is then removed in an alkali developer[2].

To create a PEVCD silica substitute, HSQ is spun onto the sample. An intermediate bake at 100°C is carried out to drive off solvents and then the sample is then hard baked

[2] This was sometimes used a substitute for e-beam written SU-8, see section 3.3.1.

at a temperature of 300-500°C. This cures the resist, dissociating the Si-H bonds, at least partially transforming the film into silica.

5.2.3 Etch Resistance

THE MOST important characteristic of an etch mask is its physical resistance (hardness). To examine this, a number of samples were made up. The above steps were followed except for that both the temperature and duration of the final bake that were varied. The etch resistance has a strong dependence on the temperature of the high temperature bake, see figure 5.6.

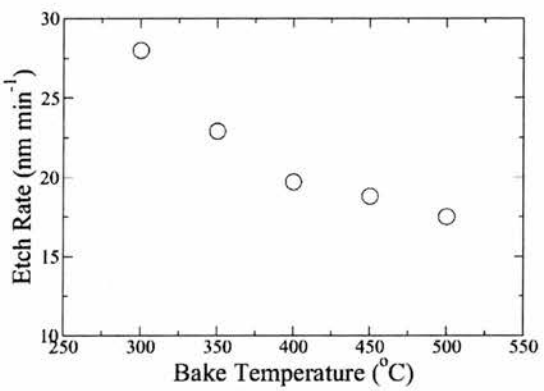

Fig. 5.6: The dependence of the erosion rate of FOx-12 on the curing temperature. These samples were etched using CAIBE at high beam voltage, low beam current conditions suitable for the creation of photonic crystals.

This is in agreement with [108], which reports a linear dependence of the hardness on curing temperature. The curing time is also important, as demonstrated by figure 5.7. After an initial rapid decrease with curing time, the etch rate asymptotically converges to a value that is presumably the etch rate of pure silica. The HSQ silica used in our etching is, thus, slightly less resistant to etching than conventional silica. By curing at even higher temperatures and/or for longer times, equivalent performance to PEVCD silica should be possible as all the S-H bonds break. However, curing at very high temperature (600°C) in an oxygen rich atmosphere may compromise device performance.

5.2.4 Optical Properties

AFTER WRITING the desired pattern in PMMA, it may be transferred into the HSQ silica using standard etching conditions in the RIE, described in chapter 3.5. Figure 5.8 shows a two dimensional photonic crystal created using a FOx-12 mask. A two layer film was used and cured at a temperature of 400°C. This gives a film thickness of approximately 200nm. The pattern was transferred using RIE with identical conditions to those used for PEVCD silica. The deep etch was carried out using standard CAIBE conditions.

A one dimensional photonic crystal created using FOx-12 is shown in figure 5.9. Slots

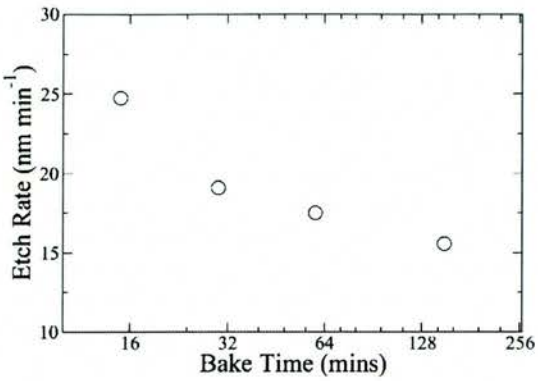

Fig. 5.7: The dependence of the erosion rate of FOx-12 on the duration of the high temperature bake. The etch conditions were the same as for figure 5.6.

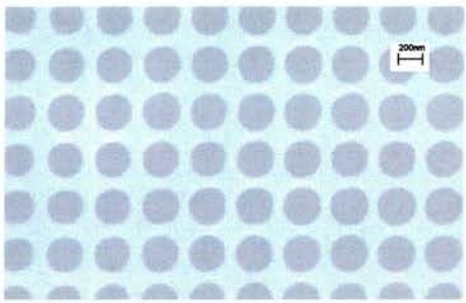

Fig. 5.8: A Photonic crystal pattern created using Fox-12 masking. This used a 2 layer film of HSQ cured at a temperature of 400°C. It was etched in the RIE and CAIBE using standard conditions.

with widths of less than 100nm may be created with low sidewall roughness. For comparison a one dimensional photonic crystal created using PEVCD silica is shown on the right of figure 5.9. As can be seen, there is little observable difference in quality between the two methods.

Figure 5.10 shows a one dimensional Photonic crystal etched in a GaAs laser material. It is well known that two dimensional photonic crystals are more difficult to etch than one dimensional, however we demonstrate that Fox-12 is a suitable mask for these crystals also. Figure 5.11 shows a two dimensional photonic crystals etched in the traditionally problematic InP.

5.2.5 Electrical Properties

IN THIS section, we compare the electrical resistance of devices using HSQ masking and PECVD masking.

In order to prevent errors due to the probe resistance, we then carried out a Transmission Line Measurement experiment [90]. On three samples, as above, a series of large contact pads were created with varying spacings between them, using photolithography and a liftoff

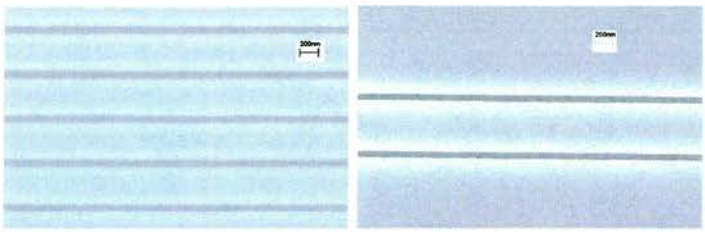

Fig. 5.9: An one dimensional Photonic crystal pattern of the type used widely in this thesis created using Fox-12 on the left and PEVCD silica on the right. Using Fox-12, sub 100nm features, with comparable quality to those etched using PEVCD silica, may be created .

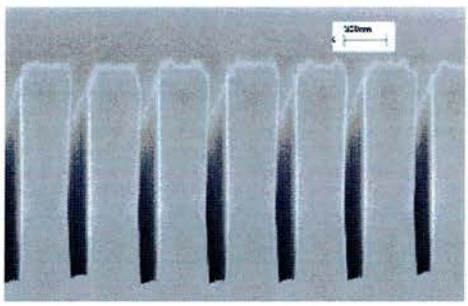

Fig. 5.10: The etching of 1-D photonic crystal in GaAs using a FOx-12 mask.

resist, see section 4.2.1. The samples were then deoxidised in HCl and Ni/Au contacts were deposited in the electron beam evaporator. The resistance between two adjacent pads is given by:

$$R_T = \frac{R_s}{W}L + 2R_c, \tag{5.3}$$

where R_T is the measured resistance, R_s is the sheet resistance, W is the width of the contact pads, L is the separation and R_c is the contact resistance. A four-probe measurement of the resistance for adjacent pairs of pads was made and the results plotted in figure 5.12. The contact resistance can then be determined from the intercept, see equation 5.3. The slope of the plot gives the sheet resistance.

The PEVCD and HSQ samples had the same sheet resistance, as might be expected.

Fig. 5.11: A 2-D photonic crystal in InP etched using a FOx-12 mask.

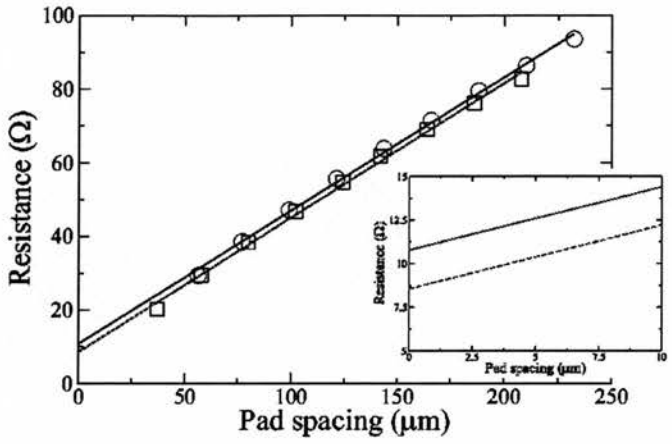

Fig. 5.12: The resistance of a Silica coated sample and a Fox-12 coated sample as a function of distance. The intercept gives twice the contact resistance- a close up of this is shown in the inset.

Interestingly, this was slightly less than that of a control sample. For the PEVCD sample, a value for the contact resistance of 5.4 ohms was obtained. The HSQ sample had a resistance of 4.4 ohms. Within the experimental error, this was equal to that of a control sample. No annealing was carried out. As the HSQ silica is spun on, it avoids the damage caused by the plasma present during PEVCD, resulting in very good surface quality.

5.3 Polymer Infilling

THE ABILITY to fill photonic crystals with nonlinear materials adds a new level of functionality. It has been shown that the presence of nonlinear material in one dimensional photonic crystals allows additional pulse compression effects [110]. Schuller *et al.* have used a related technique to fill a photonic crystal with liquid crystal creating a tunable device [111].

Figure 5.13 shows a photonic crystal which has been filled with PMMA. The PMMA was spun onto the sample and then baked at 180°C for two and a half minutes. This reduces the viscosity of the polymer allowing it to reflow.

The chief difficulty is determining whether or not the polymer is in fact filling the crystal. In figure 5.13, we have burnt contamination spots on the polymer while imaging it in the SEM, thus confirming its presence[3]. To burn a contamination spot the electron is focused to very small spot (10-20 nm) on the surface of the sample. The high intensity attracts nearby contamination (specks of dust etc.) building up a pillar which appears white in the image.

Figure 5.14 shows a 1D photonic crystal which has been filled with SU8.

The polymers used here, PMMA and SU-8, both may be used as hosts for nonlinear materials, such as laser dyes and fullerenes [112]. This could enable the use of integrated

[3] This was also tested on a non polymer filled photonic crystal. No contamination spots could be created on the slots.

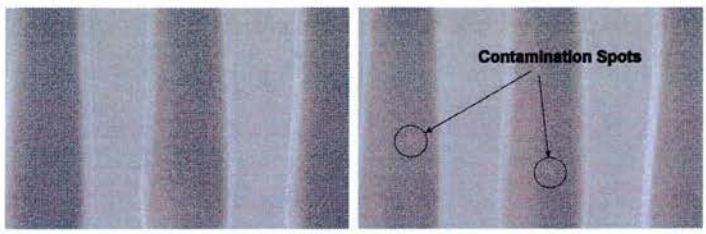

Fig. 5.13: This shows the polymer filled photonic crystal. It is difficult to determine beyond doubt whether the polymer is filling the crystal or not. In the image on the right, the electron beam is focused on part of the polymer for a few seconds burning a contamination spot, proving that polymer is present.

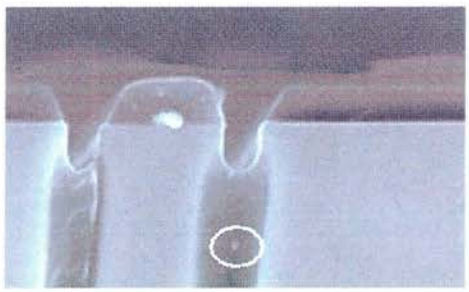

Fig. 5.14: Infilling of a InP PhC with SU8. The presence of the polymer is particularly clear in this image. A contamination spot (circled) has been burnt for illustration.

saturable dyes as the modelocking element for semiconductor lasers.

5.4 Summary

THIS CHAPTER started with a description of a regime of operation of chemically assisted ion beam etching. This method allows the use of the nonlinear etch rate of silica allowing the etching of high quality features to large depths.

Next, we describe a new method of creating etch masks for the etching of Photonic Crystals. This has a number of advantages, it is a very simple process which may be carried out in most cleanrooms, it avoids the expensive step of PEVCD deposition and it is also a more gentle process which maintains the electrical properties of the device. This is an important development for semiconductor lasers incorporating photonic crystals[4]as poor contact resistances can degrade laser performance, particularly in applications that require multiple silica deposition steps, for example [16].

Finally, we demonstrate a relatively new method of incorporating nonlinear materials into photonic crystals. This enhances their versatility and leads to a number of new potential applications. The use and potential of nonlinear laser mirrors will be discussed in a later chapter.

[4] In the later stages of this PhD, this method was used exclusively.

6. MODELOCKING OF SEMICONDUCTOR LASERS

6.1 Introduction

THE FIRST monolithic modelocked semiconductor lasers were reported in 1989 by Vasil'ev *et al.*, [23] and Sanders *et al.* [113], independently. They were multisection devices, similar to that shown in figure 6.1. A trench is etched to break the device into two sections and electrically isolate one from the other. A reverse bias is then applied to the smaller section reducing its recovery time[1].

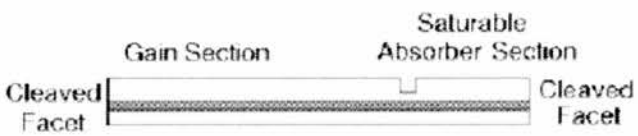

Fig. 6.1: Schematic of a two-section laser. A two-section laser is essentially the same as normal CW device. A trench is etched break the device into two sections and electrically isolate one from the other. A reverse bias is then applied to the smaller section, (from [70]).

Unlike for other short pulse laser systems, such as Ti:Sapphire and vibronic lasers, the saturable absorber is made of the same material as the gain medium.

6.2 Basic Pulsing Behaviour

IN THIS section we look at the simulated behaviour of a standard two-section device. The first section is long (500 μm) and has the parameters of a normal laser. The second section is short (100 μm) and has somewhat different parameters, see figure 6.2. We also describe the interplay between different parameters and their effect on the resulting pulse durations.

First and simplest, there is no current in the absorber section. Secondly, the parameters g_n, B, C, α and ϵ have slightly different values, see table 2.2. This is due to the different levels of band filling in the two sections [69]), i.e. in the gain section the conduction and valence bands are full of carriers, whereas those in the absorber section are relatively empty. Finally the carrier lifetime in the absorber is much shorter as a result of the applied reverse bias, (this is, after all, its purpose). We use parameters determined by Karin *et al* [41].

[1] There is another type of modelocked semiconductor laser which uses an ion implanted section as the saturable absorber. As a result, this section then acts as a saturable absorber. This is essentially the same as those mentioned above- the only difference is the method of recovery in the absorber.

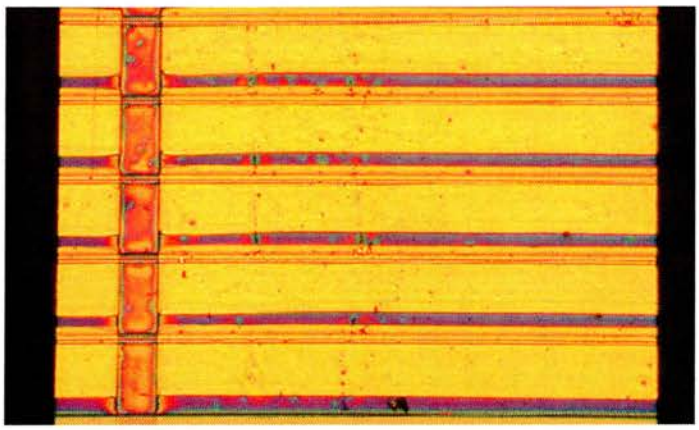

Fig. 6.2: A plan view of an actual device.

Figure 6.3 shows a typical pulse from a two-section laser. It has a duration of 2.2 ps. The asymmetry (with the front being sharper) is due to different shaping mechanisms at the front and rear of the pulse. The front of the pulse is absorbed by the saturable absorber but due to the long recovery time of the absorber (5ps at the fastest) relative to pulse duration, the saturable absorber does not shape the trailing edge. Instead, the trailing edge is shaped by gain depletion in the gain section, i.e. as a result of the passage of the pulse, the gain is reduced to the level at which the trailing edge experiences a net loss.

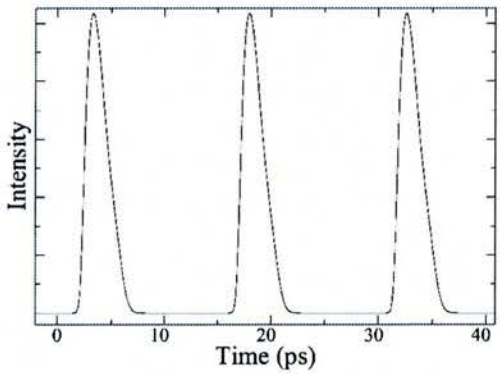

Fig. 6.3: Sample pulses from the laser (the device had a gain length of 500 μm and a 100 μm saturable absorber). The pulse duration is 2.2ps. Note the asymmetric shape.

Figure 6.4 shows one of the more straightforward aspects of modelocking in semiconductor lasers[2]. The duration of the pulse is proportional to the recovery time of the absorber. Keller *et al.* state that a slow saturable absorber can produce pulses up to 30 times shorter than the absorber recovery time [114]. This clearly does not occur in figure 6.4 (not even in theory!) In order to achieve this limit, the cavity must be carefully constructed with a slightly negative net group delay.

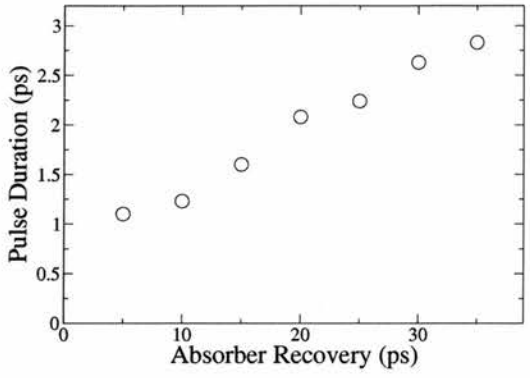

Fig. 6.4: The dependence of the pulse width on the recovery time of the absorber. For this simulation, a gain length of 500 μm, an absorber length of 100 μm and a current of 50mA.

6.3 Self Phase Modulation

6.3.1 Pulse Lengthening

MODELOCKED lasers semiconductor are limited to producing pulses in the picosecond range as a result of the large amount of Self Phase Modulation in semiconductor materials. Semiconductors are inherently very high gain materials but unlike many other systems their refractive index is very strongly coupled to their gain (both are proportional to the carrier density, see section 2.3.2). This leads to considerable nonlinearities, and thus the passage of a pulse depletes the carriers, changing the refractive index resulting in very strong self-phase modulation. The leading edge of the pulse sees the full carrier density, while the trailing edge sees a very much reduced refractive index. Reducing the carrier density, increases the refractive index. This causes a reduction in the instantaneous frequency over the duration of pulse.

The phase change that occurs when passing through a length L of the material is given by

$$\Delta\Phi(t) = -k\Delta n(I)L', \tag{6.1}$$

where k is the wavenumber of the pulse, L' is the effective length- $\int_0^L e^{-\alpha x}dx$, and $\Delta n(I)$ is the change in refractive index as a function of intensity. The pulse then develops a frequency shift

$$\Delta\omega(t) \approx \frac{d\Delta\Phi(t)}{dt} = -kL'\frac{d\Delta n(I)}{dt}, \tag{6.2}$$

following [115].

In materials in which the Kerr nonlinearity is the cause of SPM, the front of the pulse experiences an increase in instantaneous frequency while the trailing edge sees a decrease [114]. This broadens the spectrum around the original CW wavelength. In SPM, due to carrier density changes, the pulse spectrum is expanded to longer wavelengths, see figure

[2] For values of the absorber recovery above 60-70ps modelocking was incomplete or did not occur.

6.5. This leads to very strong SPM, producing relatively long, highly chirped pulses with a comparatively broad spectral width.

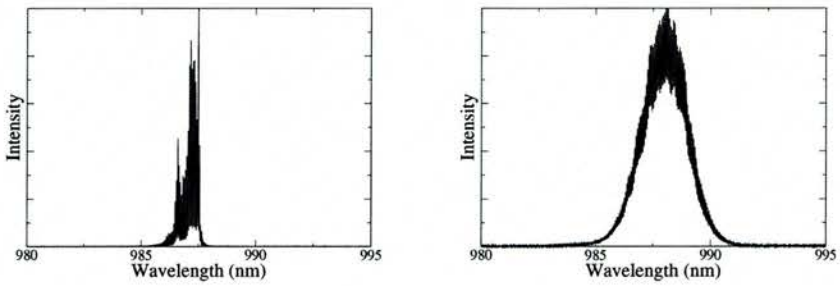

Fig. 6.5: Experimental spectra of laser operating in CW (a) and modelocked (b).

Figure 6.6 shows how the carrier density changes with the passage of a pulse. The leading edge experiences a higher carrier density whereas the trailing edge sees a depleted density. This is the origin of the considerable chirp picked up by these pulses, as in quantum wells the refractive index is strongly coupled to the carrier density,

$$\Delta n = -\frac{1}{4\pi} g_n \alpha \lambda_l (N - N_0) \tag{6.3}$$

where n is the refractive index and λ_l is the central lasing wavelength [66][3]. It should be noted that the refractive index change in the absorber is opposite to that in the gain section, see figure 6.6b. This is an additional pulse shaping mechanism, as it imposes the opposite chirp on an already chirped pulse resulting in compression it propagates through this section. However, this is small relative to the amount of chirp picked up in the gain section and the end result is a very strongly chirped pulse train.

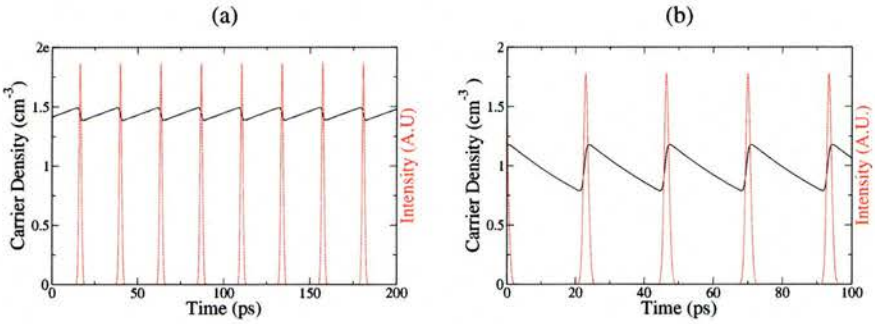

Fig. 6.6: The variation of the carrier density with the passage of pulses a) for the gain section and b) for the Saturable Absorber.

As the current injected into the gain section is increased, the carrier density and thus the amount of SPM increases. This results in greater chirping resulting in longer pulses with

[3] This is, in fact, the definition of the linewidth enhancement factor, α.

larger time-bandwidth products, see figure 6.7, which agrees qualitatively with the results of Salvatore *et al.*, [116]. In this simulation, the spectral width was approximately 2.5 nm and only slowly increased with increasing current. The time-bandwidth product is approached but not reached in this simulation.

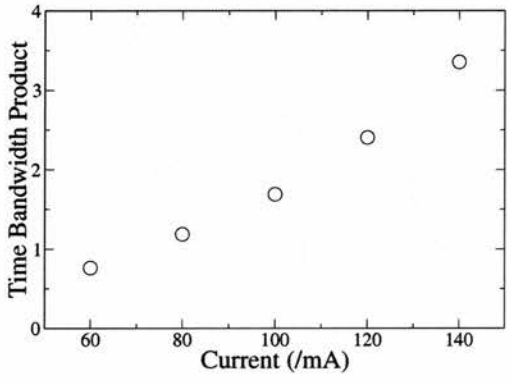

Fig. 6.7: The dependence of the time bandwidth product on the current injected into the gain section. (For a gain length of 500 μm and an absorber length of 100 μm). The pulse duration increased slowly with increasing current. The threshold current was just above 50mA.

In figure 6.8, we have modelled a hypothetical situation in which SPM can be turned on and off at will. As might be expected, the amount of of spectral broadening is directly proportional to the amount of SPM. The bandwidth width product steadily increased as well, however even for zero SPM it did not reach the transform limit. This shows chirping due to other effects such as gain saturation and gain dispersion is important.

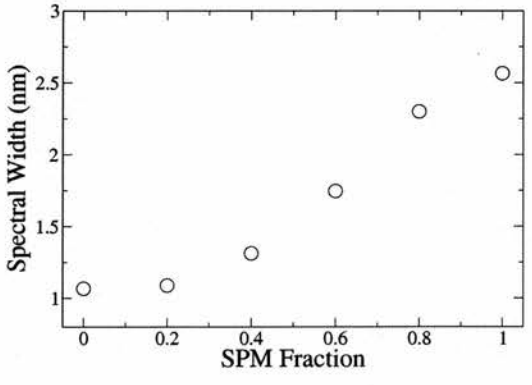

Fig. 6.8: The spectral width as a function of the fraction of normal linewidth enhancement factor.

Interestingly, for zero SPM, the spectral width of pulse was insufficient to support 2ps pulses. This demonstrates that SPM is not necessarily a disadvantage and, is in fact, essential

for ultrashort pulses[4].

6.3.2 Chirp Compensation

THE SOLUTION to this problem is, as has been demonstrated in other systems, a form of intracavity dispersion compensation. As stated earlier, ultrashort pulses have been produced from semiconductor lasers (external cavity) which have had forms of intracavity dispersion compensation. For monolithic devices, due to the simple problem of scale, this is difficult. Clearly, elements such as prism pairs and dispersion compensating fibres may not be incorporated into an 0.5-2mm long cavity. However, the dispersion compensating mirrors used successfully in solid state lasers are actually very small, typically only microns long[5]. Thus, analogous features may expected to have a role to play in monolithic devices.

Chirped mirrors are problematic in monolithic lasers. Monolithic high reflecting multilayer mirrors have been demonstrated in the form of one dimensional photonic crystals, but due to the high refractive index contrast in such deeply etched structures, reflection occurs very "quickly"i.e. over 3-7 periods. Thus, chirping is difficult to implement. Shallow etching (it does not penetrate the waveguide) gives much smaller contrasts and control of the chirped is practical [118]. However, these typically have 100s of periods, which would cause very high absorption losses in an active device. Intermediate contrasts are difficult to achieve when etching slots vertically from above as when the waveguide is partially etched through, light couples to substrate modes dramatically increasing the losses, see figure 3.2 for an example. By "etching laterally", i.e. creating a corrugation or fins along the sides of the waveguide, virtually any contrast may be achieved. On the other hand, impedance matching such a feature to a typical 5μm wide, shallow etched ridge waveguide laser would require the use of a taper. Furthermore, etching through the waveguide may create undesirable effects such as surface recombination. In time, such chirped structures may become practical, however, there is a means of achieving chirp compensation without chirping.

The Gires-Tournois interferometer (GTI) was invented in 1964 by Gires *et al.* [119]. It consists of fully reflecting mirror, a cavity and a partially reflecting mirror see figure 6.9. Intuitively, it may be considered as a spectral filter in front of a mirror. Some wavelengths are reflected by the filter, others are allowed through to be reflected at the rear mirror a certain amount of time later (given by the cavity length). Thus, these wavelengths get delayed relative to the rest. A GTI can give three orders of magnitude more dispersion than a prism pair, though over a much narrower spectral width [120]. This makes them an excellent candidate for use in modelocked semiconductor lasers which operate with relatively small spectral widths and with relatively large amounts of chirping.

[4] Most of the above discussion was aimed toward Quantum well device. Of course, if linewidth enhancement factors of zero are realised the amount of SPM will dramatically reduce, however as of yet, this is not the case and linewidth enhancements factors of 2-3 seem normal [117] as opposed to the values of 3-4 which are typical of Quantum wells. Thus, SPM in Quantum dot lasers is still very important, though slightly less so than in quantum well devices.

[5] This is, of course, ignoring the substrate on which the multilayer film is grown or deposited. It has, after all, no optical interaction with the laser.

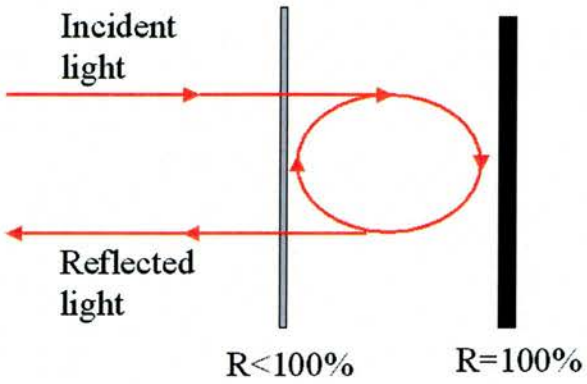

Fig. 6.9: A schematic of a Gires-Tournois Interferometer. The rear mirror is fully reflecting while the front mirror is only partially reflecting.

A GTI is described by the following equations:

$$t_g(\omega) = 2n\frac{d}{c}\frac{Q}{cos^2(\omega\tau - \frac{1}{2}) + Q^2 sin^2(\omega\tau - \frac{1}{2})}, \tag{6.4}$$

where $w = 2\pi f$, n is the refractive index of the cavity, d is the length of the cavity and Q is the cavity Q-factor [121]. This is given by:

$$Q = \frac{\nu}{\Delta\nu} = 2\pi n\nu \left[c(\alpha - (\frac{1}{L_{eff}})ln(R_1R_2)^{\frac{1}{2}})\right]^{-1}, \tag{6.5}$$

where ν is the resonant frequency of the cavity, $\Delta\nu$, α is the loss of the cavity, r_1 and r_2 are the mirror reflectivities [6]on either side of the cavity and L_{eff} is the effective length of the cavity [122]. The cavity Q-factor is clearly the dominant parameter determining the GTI behaviour[7]. This results in an inherent trade off between amount of dispersion and bandwidth over which this may be obtained. Reference [102] makes a detailed consideration of the Q-factor of 1-dimensional photonic crystal cavities.

A GTI mirror may realised monolithically using a variant of the standard deeply etched Bragg mirror, see figure 6.10. In order to obtain quantitative figures for the dispersion of such a GTI, we assume that the front mirror, corresponding to the two furthest left air-slots of figure 6.10, has a reflectivity of 0.8 and that the rear mirror has a reflectivity of unity. This is approximately valid. Loss in the mirrors will appear as a reduction in the Q-factor resulting a reduction of the maximum delay and some broadening of the dispersion curve. The cavity loss term of equation 6.5 has relatively little effect at least for the cavity lengths considered here.

[6] r_2 is set to 1 for the fully reflecting rear mirror.

[7] Note the difference between d and L_{eff} in equations 6.4 and 6.5. In a cavity of length d in a multilayer stack, light penetrates a finite distance in the mirrors. This must be included in the calculation of the Q-factor. In the calculations that follow, we assume that these are the same. There is no loss of generality, but when choosing cavity lengths in practice, this must be remembered.

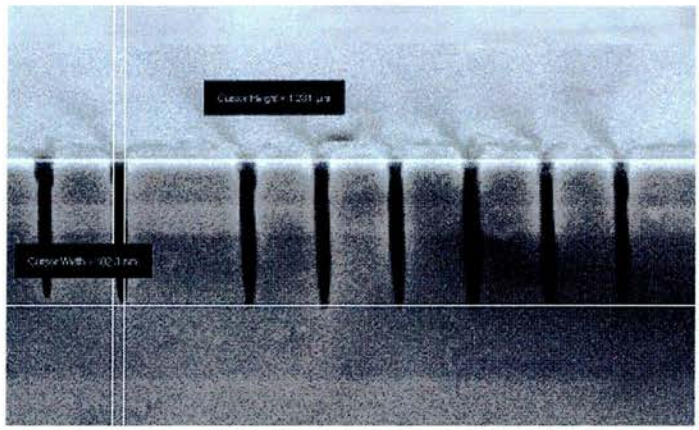

Fig. 6.10: An SEM image of deeply etched GTI mirror created using the principles of chapters 3 and 5.

Figure 6.11 shows an analytic calculation of a GTI with a cavity length of 193nm. The relatively short cavity gives low Q and thus low maximum group delay over a wide range. Reducing the front reflectivity reduces the maximum delay. Changing the cavity length slowly changes the maximum delay but it also shifts the spectral position of the maximum.

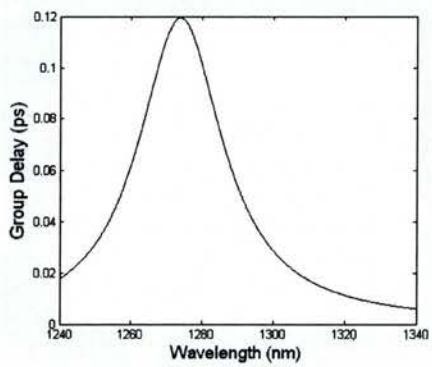

Fig. 6.11: An analytic calculation of the group delay curve of a GTI. The front reflectivity was taken as 0.8 and the cavity length was 193nm. A small amount of almost linear dispersion may be obtained over a 20nm range.

We will now make a simple calculation for the amount of chirp that must be corrected. Consider a 2ps pulse with a spectral width of 3nm. In other words, the rear of the pulse has a redshift, see section 6.3.1, of 3nm and lags behind the front by 2ps. We would, therefore, like to delay the front by, say, 1.5ps (preferably more). We may consider a single pulse as experiencing an effective length of semiconductor before being emitted (only a fraction is released at every bounce off the facet. This depends on the mirror reflectivities. The effective length:

$$L_{eff} = LF = L\left(1 + \frac{1}{ln(\frac{1}{r^2})}\right), \tag{6.6}$$

where L is the roundtrip length, r is the facet reflectivity and the rear facet reflection is

taken to be unity. Thus, we must use F bounces off the GTI to compensate the chirp. For a front reflectivity of 0.3, F is therefore 1.5. Consequently, the GTI must delay the front of the pulse by 1ps at every reflection.

Figure 6.12 shows a GTI designed according to the above criteria. It provides the necessary delay, however, linearity of the dispersion is being lost. This will complicate the chirp on the pulse making compensation more difficult.

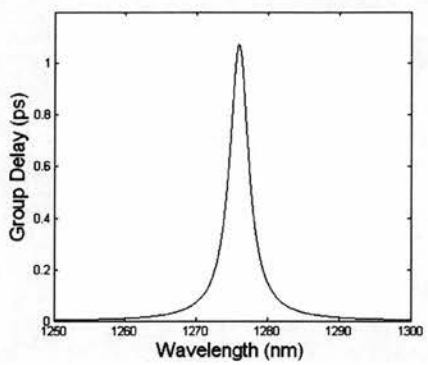

Fig. 6.12: A GTI with a 580nm cavity. It provides a large amount of chirp over a relatively narrow wavelength range.

In practice, even modeling the effects of a GTI on the laser is a very demanding task. Due to the small size of the cavity, a very fine time step is required to resolve it fully numerically, with prohibitively long computation times as a consequence.

Alternatively, a Fabry-Perot interferometer could be used. The essential principle is the same but it is somewhat more practical both numerically and experimentally. Figure 6.13 shows a simulation of the effects of a Fabry-Perot interferometer (FPI). An FPI is essentially a GTI of which the rear mirror has a reflectivity less than 1. Thus, the Q factor is reduced counteracting the effects of a longer cavity. This allows the use of longer time steps. Changing the front mirror reflectivity then gives a degree of control over the total amount of dispersion. For the parameters used in this simulation the uncompensated pulse duration was 2.5ps. The shortest pulses still did not reach the transform limit, probably as a consequence of a nonlinear compensation.

We have highlighted the usefulness of GTI mirrors and described how they might be used to produce short pulses. At the same time, we point to some of their disadvantages, namely the inherently limited bandwidth and lack of control over the shape of the group delay curve. This limited bandwidth is also a problem experimentally, as the target cavity length is very narrow, giving a very small margin for error. Thus, despite the imperfect compensation of figure 6.11, it should be easier to make than that of 6.12. Chirped mirrors, such as those of the side corrugation type, need not suffer from the above mentioned limitations and may have considerably more potential in the long term.

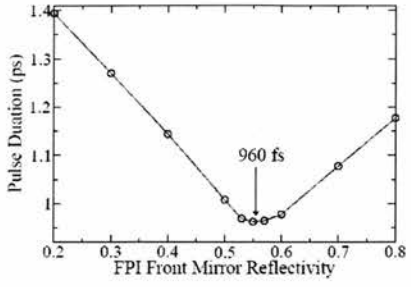

Fig. 6.13: Modeled pulse duration as a function of the front mirror reflectivity of Fabry-Perot interferometer with an 8μm cavity, from [66].

6.4 Saturable Absorber

THE THEORY of modelocking predicts that one of the prerequisites for slow saturable absorber modelocking is that the absorber saturates more strongly than the gain section. As mentioned previously, this is achieved, for example, in dye lasers, by focusing the beam tighter in the saturable dye stream than in the gain dye stream [7].

In monolithic semiconductors lasers, such an arrangement would be difficult if not impossible. Thus, it might appear, preventing the realisation of modelocking. Happily, the differential gain in a semiconductor is different above and below threshold, see figure 2.13, allowing the fulfillment of this condition. However, the similarity between the gain and absorber materials is not favourable.

It has been shown by Derickson *et al.* [123] that the pulse shortening rate increases with larger ratios between the saturation energies of the gain and absorber. This is in agreement with [13]. The saturation energy is defined as:

$$E_{saturation} = \frac{h\nu A}{\frac{\partial g}{\partial N}}, \tag{6.7}$$

where h is Planck's constant, ν is the optical frequency, A is the mode cross-sectional area, and $\frac{\partial g}{\partial N}$ is the differential gain.

Intuitively, the difference between absorbers with high and low cross sections is illustrated in figure 6.14. The high cross section absorber bleaches very quickly and removes only the very first portion of the leading edge whereas in the case of a low cross section, absorption extends further into the pulse, which is less favourable.

In figure 6.15 we look at the effects of changing the saturation energy of the absorber while holding the gain constant. This is carried out by changing the confinement factor in the absorber which changes parameter A in equation 6.7. As the confinement factor was increased, the length of the saturable absorber was simultaneously reduced to prevent the onset of Q-switching i.e this holds the depth of modulation constant. This illustrates one of the disadvantages of waveguide saturable absorbers- the low confinement factor (on the order of 0.05). Intuitively, if one was to give a SBR to a solid state laser scientist and tell him that he can use only 3% of it, he would not be too happy! Of course, changing the

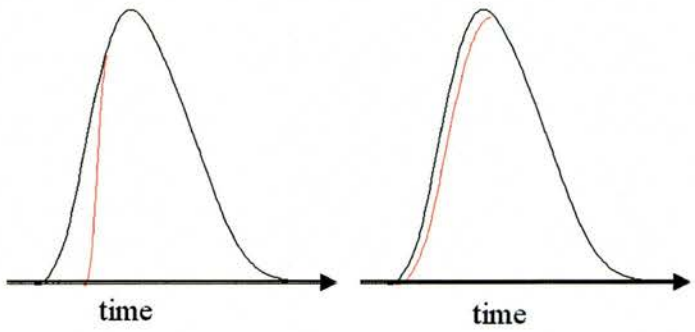

Fig. 6.14: An intuitive of picture of the difference betweeen absorbers with high and low cross-sections. On the right is an absorber with a high cross-section. This saturates very quickly removing only a portion of the leading edge of the pulse. The low cross section absorber takes longer to saturate and absorbs a small portion that extends deep into the pulse.

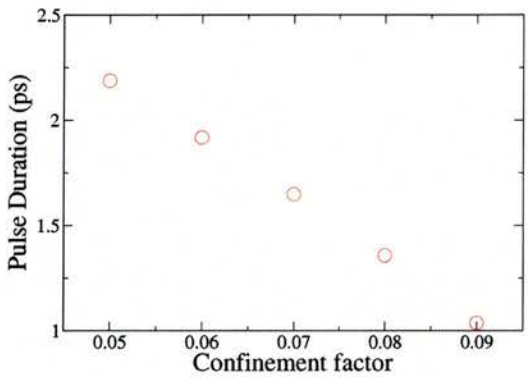

Fig. 6.15: The pulse duration as a function of confinement factor. The gain section has a constant confinement factor of 0.05. The saturable absorber length was reduced as the confinement factor was increased in order to prevent Q-switching.

confinement factor in the saturable absorber of a real device while holding it constant in the gain section is not a viable solution in practice (at least, not large changes). Thus, we must look elsewhere for an alternative.

One of these is the use of Colliding Pulse Modelocking. The geometry of the laser is chosen such that two pulses counterpropagate in the cavity and collide simultaneously in the saturable absorber. Due to the resultant increased energy in the saturable absorber, it is bleached faster increasing the effective absorption cross section [13] and [57]. From the point of view of a single pulse, it experiences an absorption that decreases almost twice as fast as would without the help of the second counterpropagating pulse (the finite size of absorber is ignored in this intuitive explanation). This method (actually, its extension multiple colliding pulse modelocking) currently produces the shortest pulses in semiconductor lasers- 610 fs at a repetition rate of 350 GHz [25]. However, this method appears to have been pushed to its

limits- there has been little further reduction in pulse duration since this result (1991).

In macroscopic scale lasers, semiconductor saturable absorber mirrors are very popular and effective methods of modelocking. While also using a semiconductor medium as the saturable absorber, much shorter pulses have been produced. This results from the positioning of the quantum well absorber in the mirror, thus all the light may interact with it.

The polymer infilling technique of section 5.3 suggests a method of achieving such a saturable absorber mirror monolithically. The insertion of nonlinear materials into Bragg mirrors could result in a sufficiently nonlinear reflectivity for use as a saturable absorber for modelocking.

6.5 Characterisation

CHARACTERISING ultrashort pulses is a difficult procedure. Everyday temporal measurements use some fast phenomenon to measure the actual phenomenon, which is invariably slower i.e. a camera flash to determine the winner of a horse race. In the case of ultrashort pulses, almost by definition, nothing shorter exists. Therefore, a technique was developed which uses the pulse itself to measure the pulse duration. The pulse is split in two, one of the sub pulses is given a delay and then the two are recombined and passed to a nonlinear detector such as a Second Harmonic crystal, see figure 6.16. This has a nonlinear response with increasing incident intensity. Thus, it gives a different signal depending on whether the two pulses are superimposed or separate. This technique, while very popular and widely used, has some drawbacks. It is very dependent on the intensity of the incident pulse, making the characterisation of low power pulses (such as those from a modelocked semiconductor laser) difficult. Furthermore, as the pulse is compared with itself, definitive information on the pulse shape is difficult to obtain. Very complicated pulses can give very confusing autocorrelations.

6.5.1 Theory of Autocorrelations

THE TYPICAL autocorrelation setup consists of a Michelson interferometer, in which one of the mirrors is movable, see figure 6.17. This may be mounted either on a loudspeaker or a motorised translation stage.

A 50:50 beamsplitter splits the incident pulse in two. One of these is given a variable delay relative to the other, τ, by the variable length arm of the Michelson Interferometer. The resultant field in the detector is given by:

$$E(t) + E(t+\tau), \tag{6.8}$$

Thus the signal from the detector as a function of τ can be described by:

$$G(\tau) = \int_{-\infty}^{\infty} \left| (E(t) + E(t+\tau))^2 \right|^2 dt, \tag{6.9}$$

where

$$E(t) = \epsilon(t) e^{i\phi(t)} e^{i\omega_0 t} \tag{6.10}$$

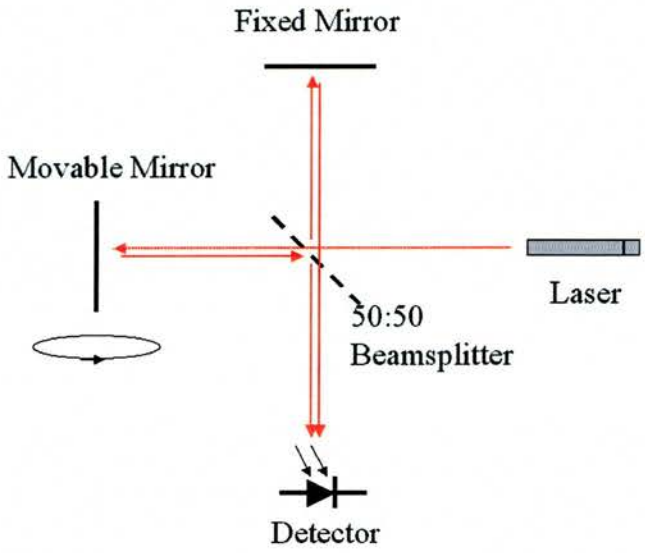

Fig. 6.16: A schematic of the typical autocorrelation setup. One of the mirrors of the Michelson interferometer is movable.

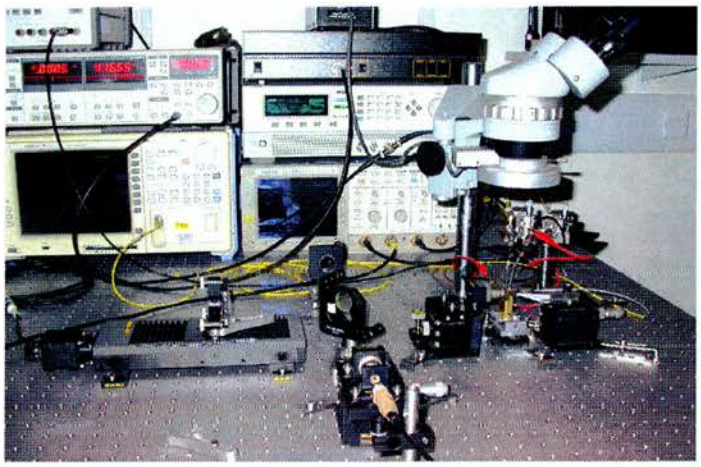

Fig. 6.17: The experimental autocorrelation setup. One mirror is mounted on a motorised translation stage. A Silicon photodiode is used as the detector.

and $\epsilon(t)$ is the real electric field amplitude of the pulse, $\phi(t)$ the phase and ω_o the frequency.

The interferometric fringes may be resolved if the speed of the detection setup is such that the detector rise time is shorter than the time to scan one fringe. This results in what is known as an interferometric autocorrelation which preserves some information on the phase[8]. If the speed is slow however, then the phase information is lost and an intensity autocorrelation results, given by:

$$G(\tau) = 1 + \frac{2\int_{-\infty}^{\infty} (I(t)I(t-\tau))\, dt}{\int_{-\infty}^{\infty} I(t)^2 dt}, \tag{6.11}$$

where I is the intensity [124]. In general, this is the preferred method to measure pulse durations as the presence of chirp in the pulse may distort an interferometric autocorrelation. An examination of this equation shows that this function has a maximum value of 3 and a minimum of 1 for delays of $\tau = 0$ and $\tau = \pm\infty$ respectively.

In order to obtain the pulse duration from the autocorrelation, the pulse shape must be assumed. For Gaussian pulses, the Full Width at Half Maximum of the autocorrelation is 1.414 times that of the assumed pulse. Similarly, for sech^2 pulses the FWHM is 1.543 that of the pulse.

A typical (numerical) autocorrelation is illustrated in figure 6.18. This was taken for a 2.5 ps gaussian pulse. As discussed above, the autocorrelation trace is wider than the actual pulse and must be deconvolved to extract the pulse duration. It being a theoretical simulation, it has the ideal 3:1 ratio, see equation 6.11 and is perfectly symmetric. In practice, due to slight misalignments and linear absorption, this ratio is not always observed.

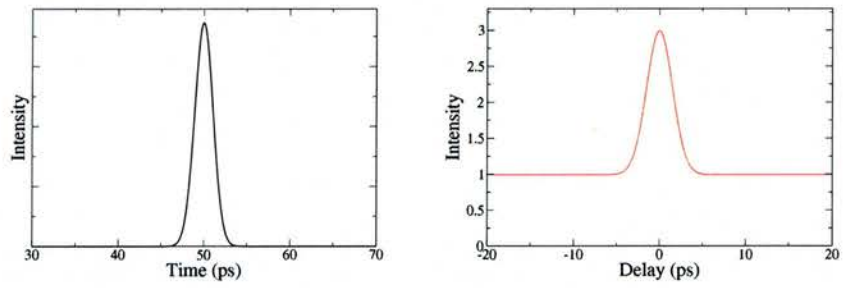

Fig. 6.18: A 2.5ps input pulse is shown on the left and the resulting autocorrelation on the right.

Figure 6.19 shows one of the disadvantages of the autocorrelation method. As the pulse train is compared with itself, the pulse shape cannot directly be measured. Thus the double pulse on the left of figure 6.19 gives a very smooth clean autocorrelation trace.

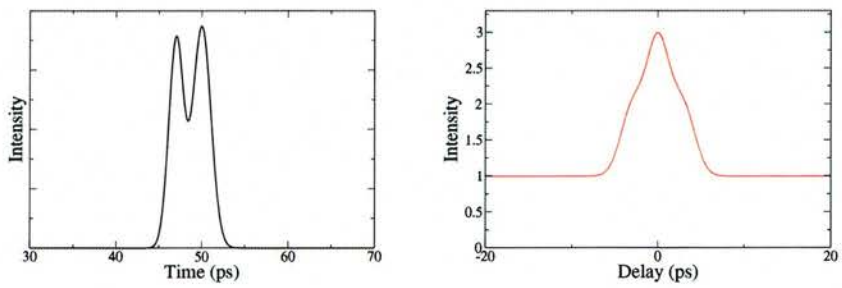

Fig. 6.19: When a double pulse is autocorrelated, the fine detail is washed out and the autocorrelation trace develops "shoulders". It the separation between the pulses is sufficiently large, they may be resolved individually.

In fact, it often happens that the more complex the pulse train, the simpler the auto-

[8] This information is usually hard to access, though.

correlation. Figure 6.20 was taken for a very complex and erratic train of pulses. The fine detail of pulses gets washed out and we see the appearance of a spike at the zero delay. This feature is known as a coherence spike. In general, as the pulse train increases in complexity, the spike becomes more pronounced.

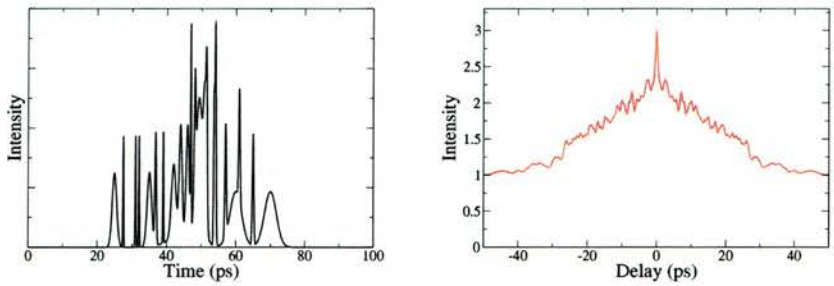

Fig. 6.20: When a complex series of pulses is autocorrelated, the resulting trace can be very confusing. A common feature is the "coherence spike" at the zero delay point.

Modelocked semiconductor lasers are renowned for the relatively poor quality of their pulses and pulse trains, thus great care must be taken when interpreting their autocorrelations.

6.5.2 *Experimental Setup and Detectors*

THE LASER diode bar was mounted on an earthed brass block. Needle probes were used to probe each laser individually. The output from one facet was used for the autocorrelation setup and that from the other (saturable absorber end) was collected with an optical fibre and taken to an Optical Spectrum Analyser or RF spectrum analyser, see figure 6.21. A pulse generator was used to drive the gain section while a DC power supply was used to apply the reverse bias to the saturable absorber section.

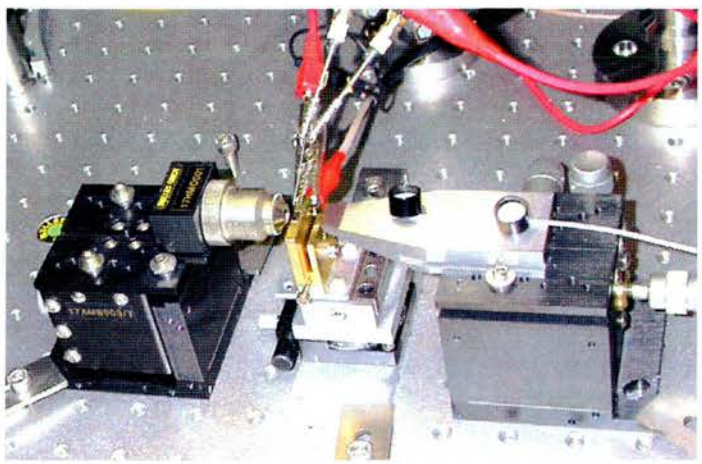

Fig. 6.21: A close up of the needle probes which are used to inject current and apply a reverse bias. These were used for all the measurements made in this thesis.

A 50:50 beamsplitter, coated for the relevant wavelength, creates the Michelson interferometer. One mirror was held fixed while the other was mounted on a computer controlled Melles Griot nanopositioning stage. The stage was paused after each movement. This allows the lock-in amplifier to remove more noise and results in an intensity autocorrelation.

The TPA detector is one of the must critical parts of an autocorrelator. In many autocorrelators, Second Harmonic Crystals are used. A photomultiplier tube then collects the light at the second harmonic. These have the advantage of being very sensitive, however they are difficult to align and have a very limited detection range. In our setup we used, primarily, photo- and laser diodes. These have been shown to be very effective TPA detectors [124] which can rival and even better SHG crystals. The output of this was connected to a lock-in amplifier which was triggered off the pulse generator. It was found that the choice of diode was extremely important. In particular, diodes which had AlGaAs active layers were very poor as a consequence of the low TPA coefficient of AlGaAs. This was exaggerated in our case due to the low peak powers produced by modelocked semiconductor lasers. The wavelength of the detector is also very important. It is preferable to be far from the bandedge of the material as linear absorption distorts the autocorrelation trace giving less than the perfect 3:1 ratio. The best results (when working at a wavelength of 1280nm) were obtained with a silicon photodiode.

6.5.3 Autocorrelations

FIGURE 6.22 shows an autocorrelation of a two-section laser made from the DO178 quantum dot material. It was 2.9mm long with a 0.5mm saturable absorber section. A 50μm wide, 300nm deep trench was used to electrically isolate the two sections. The laser had a single mode 5μm wide, shallow etched waveguide. SU-8 was used for the contact insulation. The gain section current was 310mA and the reverse bias was 7V. To avoid heating effects the device was driven at a low duty cycle (2-3%). The slight slope on the trace is due to a fractional misalignment in the setup. This is difficult to completely remove over the range of movement necessary for a 250ps scan.

Figure 6.23 shows a close up of the zeroth order autocorrelation. The trace is very symmetric. It was not possible to observe the ideal 3:1 ratio due to the presence of some linear absorption. A prominent coherence spike may seen at the zero position. The FWHM is 9ps - assuming a Gaussian pulse, this deconvolves to a pulse duration of 7 ps.

This material was designed to have a very broad bandwidth. A typical spectrum is shown in figure 6.24. The spectral width is 7nm, meaning that the pulses have a very large time bandwidth product.

For different values of the current and reverse bias slightly different pulse durations were obtained. The shortest pulse measured was 4ps.

Figure 6.25 shows an RF spectrum of one of the lasers on the same bar as the laser on which the above autocorrelations were obtained. This shows a peak at 14.8 GHz. As the length was measured to be 2.9 mm, one may deduce that the device had an effective refractive index of 3.65[9].

[9] Curiously, a value of 3.35 was predicted from a eigenmode solver.

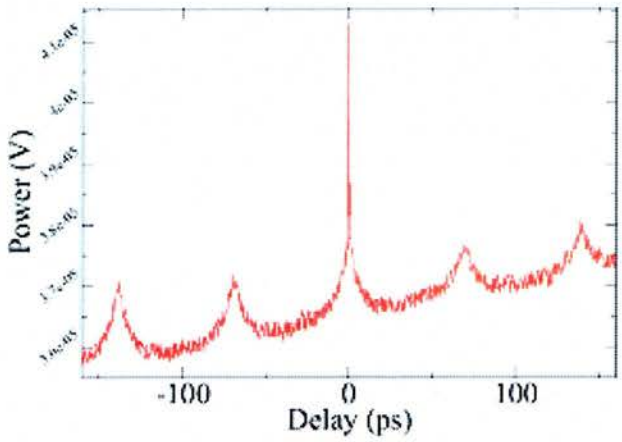

Fig. 6.22: An autocorrelation of a quantum dot laser. Cross correlations appear at delays corresponding to the roundtrip time of the laser cavity.

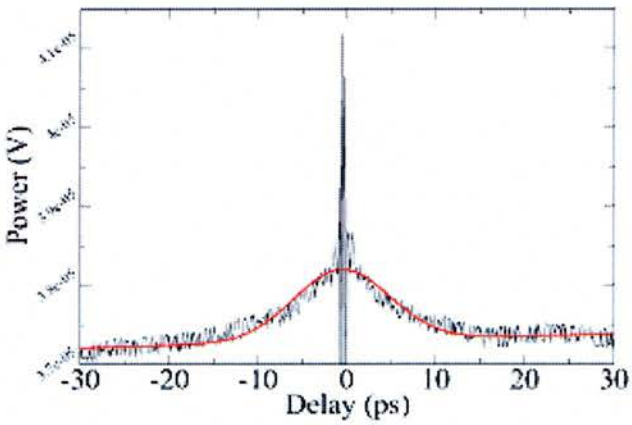

Fig. 6.23: A close up of the central peak shown in figure 6.22.

6.6 Quantum Dots versus Quantum Wells

OVER THE course of this thesis, two section lasers were fabricated in Quantum Well and Quantum Dot material. However, modelocking was observed conclusively only in the quantum dot material. It has been observed that modelocking in Quantum wells is very sensitive to the device parameters [125]. It would, therefore, appear that this is less critical for Quantum dots.

We have just mentioned the advantages of increasing the cross section of the absorber, however, a related effect occurs if the gain saturates thus reducing the differential gain. As Quantum dots have lower gain than Quantum wells, see section 4.6.2, this is a possible

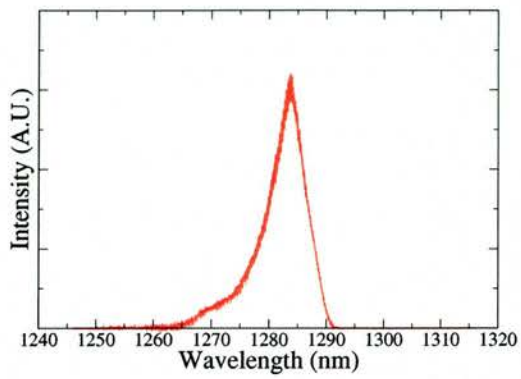

Fig. 6.24: The modelocked spectrum of the quantum dot laser.

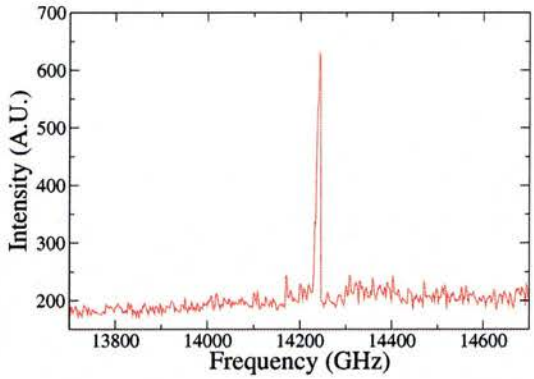

Fig. 6.25: The RF spectrum of one of the modelocked quantum dot lasers. The gain section current was 270mA and the reverse bias was 6V. The device was running at a 2% duty cycle. This repetition rate corresponds to a refractive index of 3.65.

explanation of the observed behaviour. In slow saturable absorber modelocking, the trailing edge of the pulse can only be shaped by gain saturation, thus Quantum dots have an additional pulse shaping mechanism which is weak or absent in Quantum wells.

6.7 Summary

IN THIS chapter, we started by giving a brief overview of the basics how monolithic modelocked semiconductors lasers work. We then went on to discuss the parameters which limit the pulse durations produced. SPM is the dominant effect that lengthens the pulses, though other phenomena are also present. The result of this is that typical monolithic semiconductor lasers produce pulses that are an *entire order of magnitude* longer than the limit imposed by the saturable absorber and/or the available bandwidth. Following the example of solid state and dye lasers, a method of chirp compensation is necessary. The most favourable

situation is one in which the net cavity group delay dispersion is slighlty negative. We then proposed the method of deep etching a Gires-Tournois Interferometer at one end of the laser cavity and successfully fabricated and integrated such a structure. This method, while limited in both its bandwidth and dispersion, has the advantage of being very simple in its implementation. A chirped mirror has considerably greater potential and scope, but is almost impossible to realise in high contrast deeply etched structures while absorption in low contrast structures is likely to prohibitive.

While noting that, in theory [114], waveguide saturable absorbers should be sufficient to produce ultrashort pulses, we demonstrate that they have relatively low absorption cross sections. With imperfect or absent chirp compensation, considerable advantages would be obtained through increasing this cross section and thus the pulse shortening rate of the absorber.

We discuss a method of introducing intracavity chirp compensation, a deeply etched Gires-Tournois Interferometer, and examine the potential and the drawbacks. We consider here, a simple GTI design. Numerical optimisation can be used to improve the amount and linearity of the dispersion [49], however the GTI idea is very close to limits for this application. Lateral DBRs, therefore, have the greater potential, but considerable difficulties must be overcome before they are a viable alternative.

We finish with a description of how modelocked semiconductor lasers may be characterised and give some experimental results from a two-section quantum dot laser.

In agreement without other research [126], it was observed that Quantum dot lasers appear to modelock easier than Quantum well lasers (this is, as yet, not fully quantified [10]). A possible explanation for this is the presence of an additional pulse shaping mechanism.

[10] For a full quantative analysis, more materials would need to be compared.

7. Q-SWITCHED MODELOCKING

7.1 Q-switched Modelocking

A MODE-LOCKED two-section semiconductor laser (and in general, all modelocked lasers) can operate in, broadly speaking, 2 main regimes- Q-switched mode-locking (QML) and CW mode-locking (CWML). This regime is interesting as it can produce much higher (4 to 5 times) peak powers than comparable CW mode-locked lasers [1]. Since much of the interest in ultrashort pulses involves the use of the high resulting peak intensity, Q-switched operation is promising as it maximises the peak power, see figure 7.1. This also has applications for detecting Two Photon Absorption by loss modulation [127].

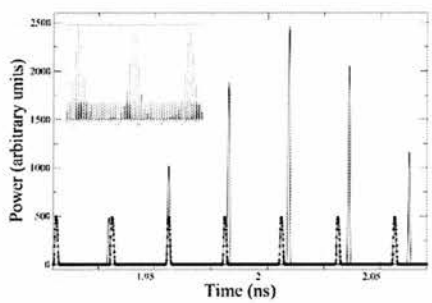

Fig. 7.1: Simulated Q-switched vs CW Mode-locking. Both taken for the same current (70 mA), continuous line for a 200 μm absorber, dashed for a 125 μm absorber. The length of the gain section was 1000 μm in both cases. The inset has a longer timescale, showing a number of Q-switching oscillations.

The QML regime occurs in a range of gain currents just above threshold, and switches over to the more commonly used CWML at higher currents. This changeover point is governed by the saturable absorber conditions, i.e. length and reverse bias. As the Q-switched envelope has a repetition rate of around 1 GHz, the mode-locked pulses (repetition rate approx. 40 GHz) beneath the envelope can have much higher peak powers than those of CWML pulses from a comparable device see figure 7.1. (It should be noted that due to the added absorption from the longer absorber, the average output power from a Q-switched laser is slightly less than from a comparable laser in the CW mode-locking regime.)

Figure 7.2 shows the pulse trains produced by a device with a 1000 μm gain section. As the length of the absorber is increased from 100 μm to 240 μm the device makes the transition to Q-switched modelocking. For intermediate lengths the amplitude modulation of the underlying modelocked pulses is unstable.

[1] This work was carried out in conjunction with Michael Flynn.

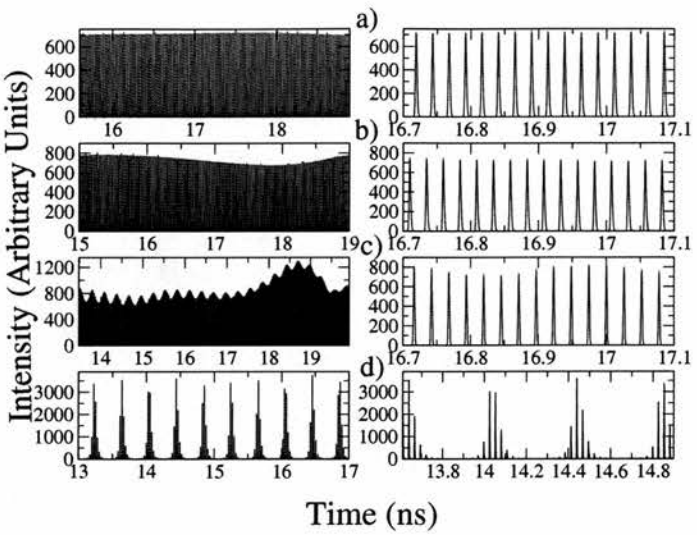

Fig. 7.2: The change of regime with increase in saturable absorber length. a) CW Modelocking, b) and c) unstable modelocking, d) Q-switched modelocking, (from [70]).

The model also predicts some more complicated features. In certain parameter ranges discontinuities appear in the previous graphs, figure 7.3. With the increase in the "strength"of the absorber section due to the quicker recovery time, the laser's mode of operation can change dramatically, and instead of producing a regular train of pulses, bursts of higher energy pulses are released.

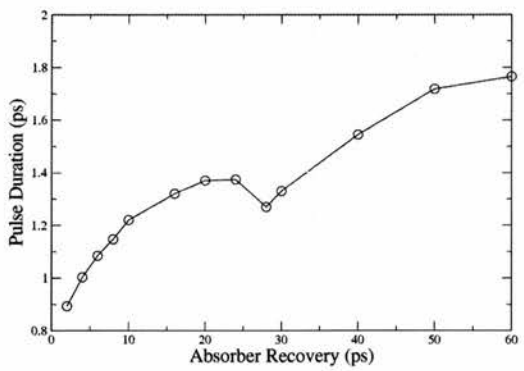

Fig. 7.3: The dependence of the pulse width on the recovery time of the absorber. The absorber length was 1000μm and the current was 60mA. This anomalous behaviour occurs only in certain parameter ranges.

7.1.1 Causes of Q-switched Modelocking

TO OPERATE in the QML regime, a relatively long saturable absorber is necessary. Intuitively, due to the resulting high absorption, the onset of pulsing is delayed and the carrier

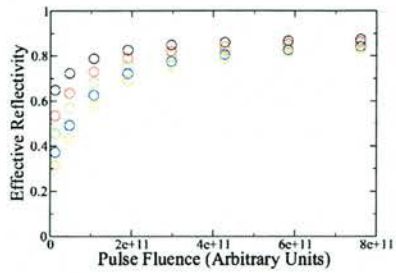

Fig. 7.4: The effective reflectivity of a set of absorber-facet combinations. This was calculated using the previously described numerical model in single pass configuration. Black indicates an absorber length of 50 μm, red- 75μm, green- 100μm, blue- 125μm and orange 150μm.

population builds up to a higher level. A burst of high-energy pulses is then released, depleting the carrier population. The carrier density then recovers, setting up a cycle. Increasing the current reduces the time taken for the gain density to reach the point where the burst of pulses is released, thus increasing the Q-switching repetition frequency. Q-switching in solid-state lasers has been examined by Honninger *et al.* [4], and the tendency to Q-switch has been shown to be related to the depth of modulation of the saturable absorber. Using the above-mentioned model in a single pass configuration, we can estimate the depth of modulation of a given saturable absorber, see figure 7.4. A sample pulse makes a single roundtrip through the saturable absorber; the resulting energy of the pulse is compared with that of the original, giving an effective reflectivity for the absorber-facet combination. By repeating this for a number of different initial pulse energies, the depth of modulation can be calculated. This is a measure of how effective the absorber is in discriminating between high and low energy pulses. In figure 7.4, we plot the difference in reflectivity between the lowest intensity pulse and the highest. While this is not the strict definition of the depth of modulation, it is an accurate comparison.

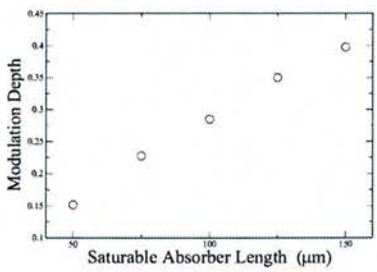

Fig. 7.5: The depth of modulation of the absorber plotted against absorber length. The depth of modulation is an important parameter which governs the mode of operation of the laser.

We also find, as might be expected, that the depth of modulation is proportional to the length of the absorber, see figure 7.5.

7.1.2 Q-switching Repetition Rate

IN THE case of a relatively short absorber, the absorber is fully saturated at high pulse energies. Thus, two high-energy pulses with slightly different energies see much the same effective reflectivity. This corresponds to the case of CW mode-locking. For a relatively long absorber, the depth of modulation is much larger, and for pulses with energies similar to those just discussed, the absorber may not be saturated to the same degree. Thus, for two comparable pulses, the higher energy pulse can experience a significantly lower loss[2]. This favours the production of very high-energy pulses i.e. Q-switched mode-locking.

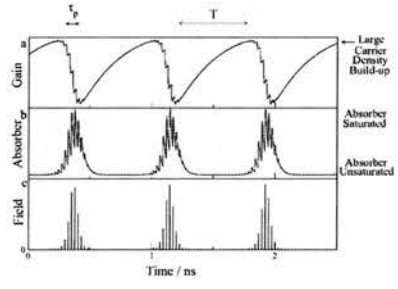

Fig. 7.6: Gain curves plotted against time for both gain and absorber sections The passage of the burst of pulses deeply depletes the carrier density. Also shown is a pulse train, (from [70]).

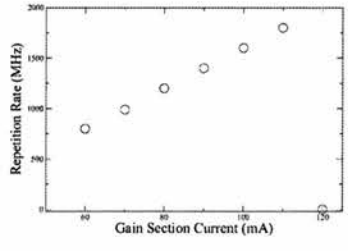

Fig. 7.7: Simulated dependence of the Q-switching frequency on the current. With increasing current, the time taken to the reach the threshold for the release of the Q-switched pulses is reduced.

The burst of Q-switched pulses very quickly depletes the carrier density, and thus the gain, in the gain section (the rate of gain/carrier depletion is proportional to the peak intensity- see equation 2.18). After the passage of these pulses, the intensity of light oscillating drops down to a very low level. The carrier density then starts to rise again, until the gain reaches a threshold level at which the pulse starts to increase again. Within a few roundtrips, the pulse grows to an unsustainable level and starts depleting the carrier density faster than it can be replenished, releasing a burst of Q-switched pulses, see figure 7.6. Clearly, the time taken to reach this threshold will be inversely proportional to the current.

In fact, there is a linear relationship between the repetition rate and the current as illustrated by figure 7.7. This linear relationship is somewhat surprising and is related to

[2] All lasers are very sensitive to reflection- a change of a few percent can have dramatic effects.

the assumption that the gain depends linearly on the carrier density, made earlier in the derivation of the model, equations 2.15 and 2.27 and figure 2.13. However, this is actually quite accurate as will be demonstrated later.

7.1.3 Suppression of Q-switching

INCREASING the current eventually results in the device switching its mode of operation to CW modelocking. At the first level, the increased current brings the bursts of Q-switched pulses closer together. Also, due to the effects of gain saturation and spectral hole burning, the gain section may preferentially amplify weak pulses over strong. In figure 7.8, using the previously mentioned single-pass variant of the traveling wave rate equation model, we examine the amplification of different pulses by the gain section. The calculation is made for three different carrier densities. In order to allow a comparison to be made between their shapes, these have been normalised so that the highest energy pulses see the same amplification. This mechanism acts to equalise the peak intensities of the pulses and acts against the tendency to Q-switch.

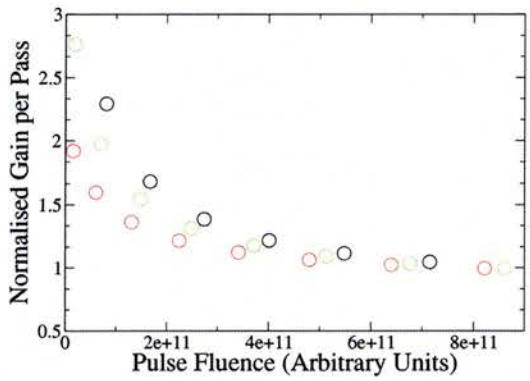

Fig. 7.8: Normalised gain curves for carrier densities of $2.0\times10^{18}\text{cm}^{-3}$- red, $2.5\times10^{18}\text{cm}^{-3}$- green and $3.0\times10^{18}\text{cm}^{-3}$- black.

7.1.4 Regimes of Operation

IN FIGURE 7.9, we show a simulation which examines the dependence of the laser's regime of operation on the saturable absorber length and current in the gain section. As this parameter map was to be used as an aid to fabrication, we only consider the broader features i.e. CW modelocking vs Q-switched modelocking. In practice, there are a number of intermediate regimes which occur near the switch-over points. Figure 7.10 shows the dependence of the operating regime on the length and recovery time of the absorber. The depth of modulation depends very strongly on the length and this is the dominant factor.

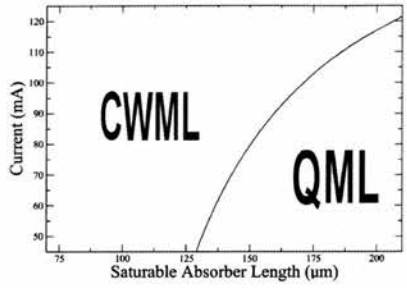

Fig. 7.9: This shows the regimes of Q-switching behaviour as a function of saturable absorber length and current. (The region marked QML shows the parameter range for which Q-switched Mode-locking takes place; CWML indicates CW mode-locking). All simulations were carried out for a gain section length of 1000 μm.

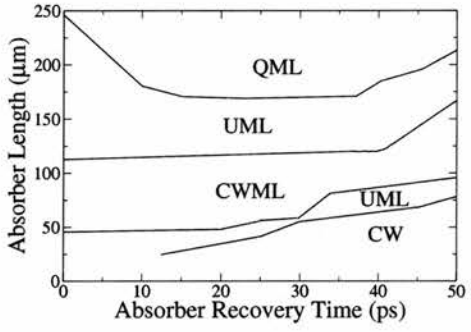

Fig. 7.10: The various regimes as a function of absorber length and recovery time. The regimes are only weakly dependent on the absorber recovery time, (at least when compared with the dependence on the absorber length), from [70].

7.2 Experimental Results

7.2.1 Quantum Well Devices

WE FABRICATED a simple two-section laser comprising of a 1080 mm long gain section and a 270 mm long saturable absorber section. The two sections were isolated using a 25 mm wide, 200 nm deep trench. This had an electrical resistance of approximately 1 KΩ. This was fabricated in the QT1719 material, see section 4.6.1. The output was examined using a 25 GHz RF spectrum analyser and fast photodiode. Figure 7.11 shows a sample trace. With the absorber grounded, the device showed pulsing in the range 400 MHz to over 1.6 GHz, the frequency of which is dependent on the current flowing through the gain section. The device had a threshold of approximately 40mA. Due to the low power output, it proved difficult to detect pulsing close to threshold. The observed frequency shows a linear dependence on the current injected into the gain section, see figure 7.12. No Q-switching is observed for currents greater than 100 mA. As the photodiode used in the experiment cannot respond to a repetition rate greater than 25 GHz, we can interpret this point as being the transition point to CW mode-locking (with a repetition rate of approx 40 GHz). Devices with approximately

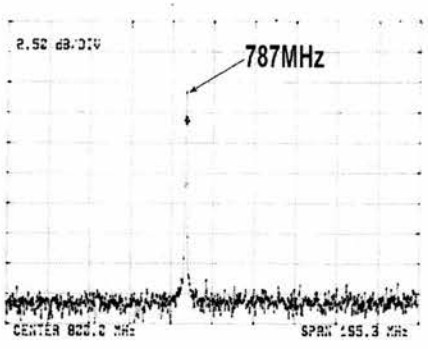

Fig. 7.11: An RF spectrum of Q-switching at 787 MHz. Measured using a fast photodiode and RF spectrum analyser, (from [70]).

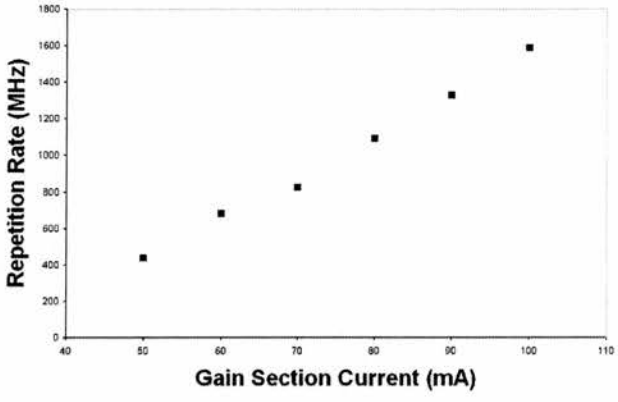

Fig. 7.12: The experimental dependence of the Q-switching frequency on the current flowing through the gain section, (from [70]).

the same gain section length but with shorter saturable absorbers were also fabricated. No Q-switching was observed from these devices. This shows reasonable agreement with the predictions of the model.

Figure 7.12 shows good agreement with the behaviour predicted theoretically in figure 7.7. This shows the accuracy of the seemingly simplistic assumption of a linear gain with carrier density, see section 7.1.2.

7.2.2 Quantum Dot Devices

WE HAVE also observed Q-switched modelocking in a Quantum dot laser. This was made from the DO-171 material. Autocorrelations of this device are presented in section 6.5.3[3].

Figure 7.13 shows pulsing at a repetition rate of 64MHz. Higher harmonics appear at higher frequencies. When Q-switched modelocking occurs, sidebands are created on the main modelocking peak in the RF spectrum, as the two oscillations mix. Figure 7.14 shows side bandbands on the main modelocking peak generated by the Q-switching.

[3] For the autocorrelations, the device was operating in the CW modelocked regime.

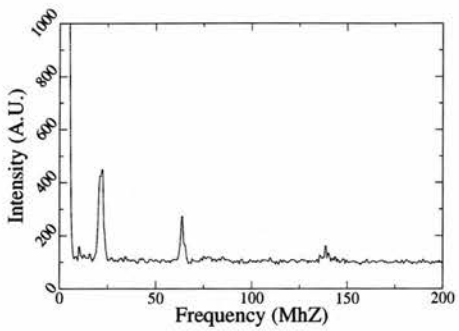

Fig. 7.13: Qswitching observed in a Quantum dot laser.

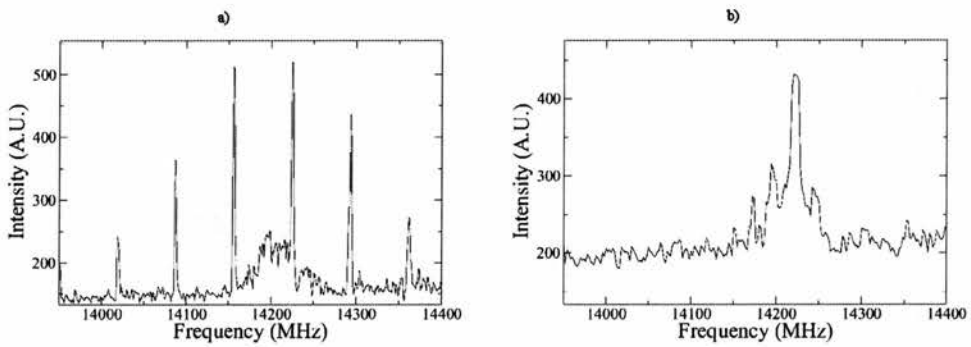

Fig. 7.14: a) The Q-switching modulation envelope generates sidebands on the main modelocking peak in the RF spectrum. b)The RF trace for a higher current than that shown in a). As expected, this moves the device out of the Q-switched modelocking regime and into the pure modelocking regime. (The observed trace is weak as the device is running at a low duty cycle. The actual power output from the laser was also very low for this measurement).

In qualitative agreement with figure 7.1.4, when the current was increased (from 320 to 360mA), the Q-switching envelope disappeared. Contrary to the model's predictions though, no tuning of the Q-switching frequency with current was observed. The window of currents for Q-switched modelocking is evidently much smaller than that for quantum well devices.

7.3 TPA and loss modulation

WARREN *et al.* have recently demonstrated a new technique of measuring the two photon absorption cross section (TPA) of a material. This has a number of advantages over other techniques. Firstly, it may be used on non fluorescent material unlike the very sensitive method of two-photon excited fluorescence (TPF), in which the TPF is picked out from the main signal using spectral filters. Secondly, it requires 100 times less peak intensity than the other main method of detecting TPA, the Z-scan technique, during which the sample is translated along the propagation path of the focused beam [127].

When a train of modelocked pulses (frequency f_0) are modulated in the time domain at a frequency f, sidebands are generated in the frequency domain at $f_0 \pm f$. Two photon absorption will then preferentially absorb pulses at the maxima of the modulation envelope. This generates additional sidebands in the frequency domain at $f_0 \pm 2f$, see figure 7.15. Thus, the TPA signal is separated from the main signal in the frequency domain and using an RF spectrum analyser may be determined accurately.

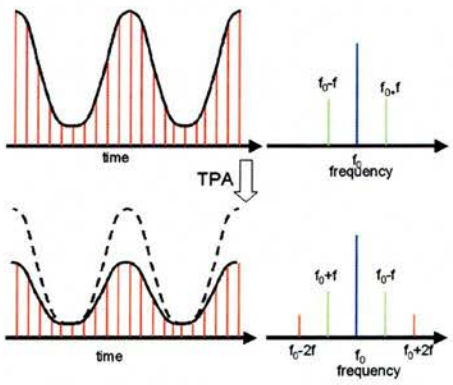

Fig. 7.15: TPA will preferentially absorb pulses with high peak intensities over those with low peak intensities. Thus the shape of the Q-switched envelope is changed resulting in additional sidebands in the frequency domain.

Warren *et al.* developed this technique using a Ti:Sapphire laser with an acousto-optic modulator. Q-switched modelocking in semiconductor lasers naturally provides a modulated train of modelocked pulses with high peak powers and thus may find application as a cheap source for TPA detectors.

7.4 Summary

IN THIS chapter, we have used the numerical model of chapter 2 to determine one of the most fundamental questions when fabricating two-section semiconductor lasers- what lengths should chosen for the two sections?

Devices with relatively long saturable absorbers easily operate in the what is known as Q-switched modelocking. We then examined the Q-switched mode-locking regime in detail both experimentally and theoretically and explained the principal mechanisms behind this behaviour. From this, simple guidelines to maximise the peak power from such a laser may be formulated. The maximum usable current should be determined and consulting figure 7.9 (or its equivalent), an absorber with sufficient length to cause Q-switching then chosen. Conversely, if Q-switching is undesirable, the operating current range should be chosen and an appropriate saturable absorber chosen to ensure over all this range, in particular at the lower currents. This is of particular importance if the shortest possible pulses are desired as these occur at low currents (low SPM) and long absorbers (large DOM).

Q-switched modelocked semiconductor lasers may also be useful as a source for TPA detection. Clearly the peak intensities produced will not compete with those produced from

a solid state laser, however their cheapness and compactness may be preferable in some lower specification applications.

8. SIDEWALL RECOMBINATION DEVICES

8.1 Introduction

IN this chapter we look at two types of devices in which surface sidewall recombination is an important factor. In the first device, surface sidewall recombination is desirable and is used to provide a means of fast recovery to the saturable absorber. In the second device, a quantum dot laser, we make use of the high confinement of carriers to the dots which minimises surface recombination. Thus, we may create devices with very narrow waveguides which normally have prohibitively high threshold currents.

8.2 Background

WHEN creating a semiconductor laser, it is desirable to confine carriers to the active region as tightly as possible. The obvious way of achieving this is to etch the waveguide defining ridges all the way through the active layer (known as a mesa), thus carriers are unable to diffuse laterally and leave the active region. This has the side effect of confining light very strongly to active layer, due to the very large refractive index step. If operation in a single mode is required then the width of the active layer must be kept very small- on the order of 1-3 μm wide.

However, when the quantum well(s) are etched through, carriers may recombine nonradiatively using surface states, see figure 8.1. These surface states are caused by unmatched bonds at the abrupt termination of the lattice (known as "dangling bonds") [128][1]. This is normally described by a surface recombination velocity. Values on the order of 10^5cms^{-1} for GaAs and 10^4cms^{-1} and InP are typical [128]. These values are large- to give a physical picture, for a 10μm mesa laser in InGaAs, over half the carriers can be lost at the interfaces.

Nonetheless, it is very advantageous to use very small, strongly confined active regions, leading to a number of efforts to circumvent this problem. The simplest method to avoid surface recombination is to use shallow waveguide defining trenches which do not break the active layers (i.e. a ridge waveguide). This is relatively simple and effective and was the primary method used in this thesis, see section 4.3. However, this has the disadvantage of very weak lateral confinement of carriers. In fact, in some cases, the loss of carriers due to outward diffusion can be on the same order of magnitude as that due to sidewall recombination in mesa devices.

The use of surface passivation, such as immersion in an aqueous sulphur solution or

[1] In the early days of quantum wells, surface recombination at the interfaces between layers was also a problem. With various developments and improvements in material growth, this is minimal in most modern materials (experimental new materials being the exceptions).

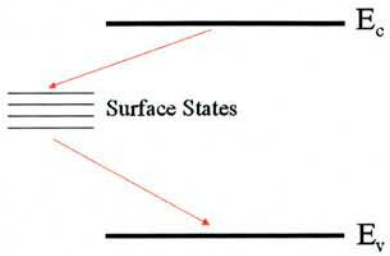

Fig. 8.1: The presence of surface states may create midgap energy levels. Electrons may be trapped in these temporarily before dropping to the valence band. This is a non radiative recombination path [128].

heating in a hydrogen atmosphere, may reduce the surface recombination velocity through the removal of surface states, however these effects are not always permanent.

The most successful solution has been to regrow a higher bandgap material over the etched mesa, creating what is known as a buried heterostructure (BH). This then provides a lateral potential difference which confines carriers. This provides lasers of very high quality and performance, though the regrowth step is demanding. Furthermore, they are very difficult to realise in materials containing AlGaAs as the mesa etching process often results in the oxidation of the Aluminium.

Surface recombination can be included into the rate equations by adding a term, R_{sr}, to equation 2.25, following [128]. This is given by:

$$R_{sr} = \left(\frac{2}{w} + \frac{2}{L}\right) v_s N, \tag{8.1}$$

where w is width, L is the length, v_s is the surface recombination velocity and N is the carrier density. The term $\left(\frac{2}{w} + \frac{2}{L}\right)$ describes the device geometry and is the ratio between the exposed surface area and the volume of the active region [2].

Some recombination mechanisms, such as spontaneous emission, are described using a decay time, e.g. $\frac{1}{\tau_n}$. For surface recombination, the rate is described as a decay rate for some capture length- $\frac{L_c}{\tau}$. Thus, more surface states result in a smaller lifetime and a larger overall capture rate. Greater thermal diffusion of carriers gives a larger L_c and similarly a larger capture rate. As this rate has units of velocity, this phenomena is described as a surface recombination velocity.

8.3 Measurements of Recombination Rates

IN ORDER to determine the amount of sidewall recombination that takes place, we fabricated sets of mesa lasers in a quantum well material (QT1041).

Using layers of spun on HSQ that was then baked at 500°C for an hour, a hard mask was put down on, as described in section 5.2. An SU-8 mask was then spun on, and using

[2] Calculated here for an in-plane geometry, i.e. the lasers used in this thesis. This term would be different for a vertical cavity surface emitting laser.

electron beam lithography, 5-50μm stripes were defined. This pattern was then transferred into the HSQ using RIE and the remaining SU8 removed in an oxygen plasma. Using high voltage, low current CAIBE, (section 5.1) 2μm mesas were created. The remaining HSQ was then removed using a Hydrofluoric acid wet chemical etch. SU-8 insulation pads were put down using second stage alignment in the electron beam writer and contacts were then down as normal using electron beam evaporation.

The devices were then cleaved up into desired lengths and P-I curves were taken for each mesa width. The threshold current densities were then plotted as a function of mesa width.

A simple model, that is based on rate equations that include a sidewall recombination term, e.g. equation 8.1, is sufficient to describe the varied width Quantum well lasers. However in more complicated material, i.e. Quantum dots, the curve is more complicated, requiring the diffusion length to be included.

This effect was then added to the model through, following [61]. The resulting theoretical curves are shown in figure 8.2. For this material, a value of 5×10^5cm s^{-1} was obtained for the surface recombination velocity and 6μm for the diffusion length (long enough that it may be ignored with little loss of accuracy).

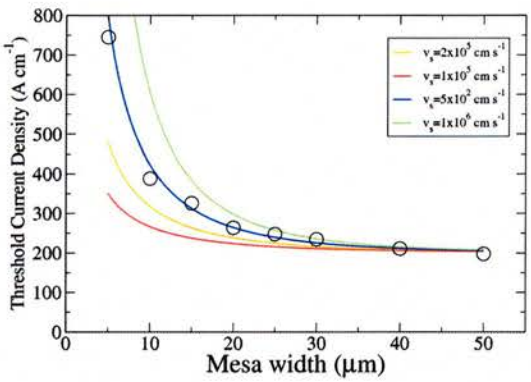

Fig. 8.2: The dependence of the threshold current density as a function of mesa width for a quantum well material (QT1041). The experimental data data points are shown as circles with the curves showing the theoretical curves for various values of the surface recombination velocity.

8.4 Sidewall Recombination for Saturable Absorber Recovery

AS mentioned previously, a saturable absorber with fast recovery is necessary to achieve modelocking, see section 6.2. Traditionally, the speed of the saturable absorber is enhanced by applying a reverse bias which removes carriers at faster rate than without a bias. Another possibility has been to use ion bombardment to create defects at which carriers recombine non-radiatively. Thus, any method which removes carriers may be suitable. Recent work [129] demonstrated recovery times of 5-10 ps in a GaAs photonic crystal using sidewall recombination. This compares favourably with the values obtained via a reverse bias (5-

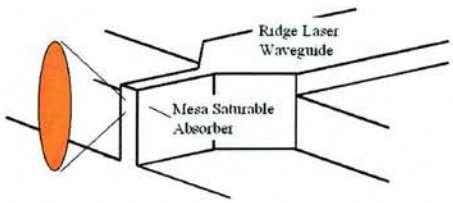

Fig. 8.3: A schematic of the laser design, showing the ridge laser,the taper and the mesa saturable absorber.

50ps) [41].

There is also the additional advantage in that, as carriers are directly removed from the well rather than from the well to the seperate confinement heterostructure and only then out of the device, they do not have the opportunity to increase the recovery time through a screening of the applied electric field [43].

When a pulse is incident on the device, it is absorbed, creating carriers, see section 2.3.1. These diffuse rapidly to the etched interfaces where they recombine nonradiatively, returning the absorber to a unsaturated state.

In this section, we attempt to create a modelocked laser which uses such a saturable absorber. Clearly, similar to [129], a photonic crystal saturable absorber may be incorporated which would have additional functionality to that of a simple absorber. This is the ultimate goal, however initially we attempt to incorporate a straightforward sidewall recombination SA.

We work with a device with the simple design of the usual ridge waveguide as a gain section which tapers down into an uncontacted narrow mesa. The combination of deep and shallow etched waveguides makes the fabrication of this device challenging.

8.4.1 Design

IN ORDER to avoid reflection at the interface between the gain section and sidewall recombination SA, a tapered section must be used, see figure 8.3. Figure 8.4 shows how this taper length affects light propagating in the device. This is, in fact, a very important point. Reflection at this interface not only reduces the interaction with the SA, it may also create shadow pulses of the primary modelocked pulse rapidly increasing the pulse duration, see figure 8.5.

8.4.2 Fabrication

THE OBVIOUS method of creating the deeply etched section is to follow the method used when integrating photonic crystal features i.e. to deeply etch first and spin resist layers on top, see section 4.8. This simple procedure works effectively only for small ($\approx$100 nm wide) features (though care must still be taken) as the resist easily fills this features and a high quality film may be created with little difficulty. However, over the relatively large feature

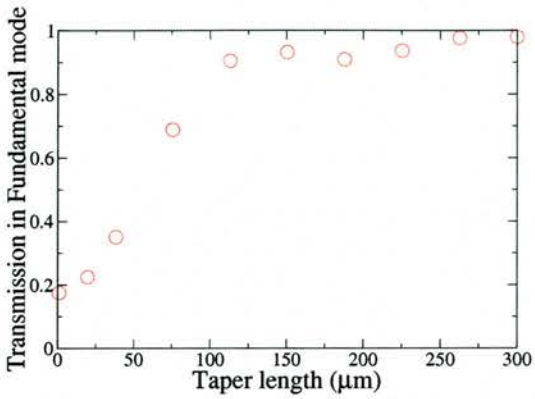

Fig. 8.4: Transmission in the fundamental mode as function of taper length.

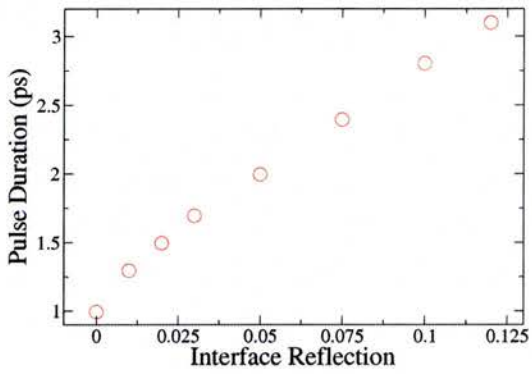

Fig. 8.5: The effect of a finite reflectivity at the interface with the saturable absorber on the pulse duration. Any reflection at this point creates shadow pulses. Values greater than than those shown may even prevent modelocking.

sizes needed here ($\approx 100 s \mu m^2$), resist is unable to form a continuous film. Thus, we must reverse the procedure and follow one of the standard rules of lithography and leave the deep etch step until last.

An elegant solution to this would be to fabricate the laser as normal until the contact deposition step. Using electron beam resist for liftoff, the contacts may be deposited in a suitable shape and used as the etch mask. However, the standard contact does not have sufficient hardness to achieve the necessary etch depth. Its resistance may be improved by depositing an additional layer of Nickel but this has a detrimental effect on the device resistance.

The following solution was, therefore, adapted- after creating the ridge waveguides as normal, the sample is spun with SU8[3]and etch masks of the necessary shape electron beam written, see figure 8.6. SU8 has a very good physical resistance to ion beam etching and

may be used to reach the necessary depth with little difficulty.

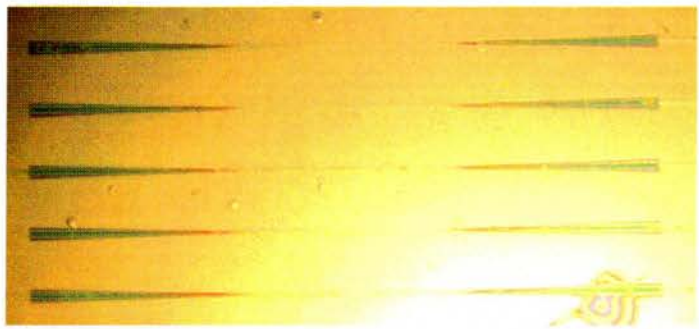

Fig. 8.6: The SU8 deep etch mask (appears green) prior to the insulation step. The taper and narrow waveguide region is clearly shown. (The chip will be cleaved on a line through the middle of the picture seen here, creating two sets of devices).

The next step is to put down the contact insulation. Clearly, care must be taken not to cover the area to be deeply etched with insulation. This be may be carried out easily using photolithography. Surprisingly, SU8 insulation proved unsuitable. It seems that some acid [4]remains in the electron beam written SU8 which triggers crosslinking in the insulating layer preventing its removal. Therefore, SR1818 photoresist was used instead (following a similar procedure as for SU8). After this, fabrication may continue largely as normally. After contact deposition, the deep etch step may be carried out. To prevent damage to the contacts, and hence an increase in the electrical resistance, these were protected with a photoresist mask.

A step by step description of the final process is given in section 10.4.

8.4.3 Measurements

FIGURE 8.7 is an endview of an actual device. The gain section comprised a 500μm long, 5μm wide shallow waveguide. This was tapered down to a 100 μm long, deeply etched 1-2μm wide waveguide over a length of 200μm [5].

The output of this device (from the untapered facet) was taken to a fast photodiode (up to 25GHz) using an optical fibre. The fast photodiode was then connected to an RF spectrum analyser.

Self-Pulsing at frequency of 540MHz was observed for a device with a deeply etched waveguide width of 2μm for an injected current of 175mA, see figure 8.8. This frequency was found to increase with increasing current, though with a noticeable broadening of the peak.

As may be seen from figure 8.7, the quality of the narrow waveguide was poor. Electron beam written SU8 does not have square edges. Thus, during the deep etch, the edges may degrade resulting in increased edge roughness in the final waveguide. The scattering

[3] As used during the insulation step, SU8 may reflow off the etched ridges. To avoid this problem here, the SU8 was "baked"under vacuum rather than on a hotplate. This bake step is carried out to simply drive off solvents, thus placing under vacuum is equivalent to normal hotplate baking.

[4] The chemical used to catalyse the cross linking reaction reaction in SU8 after exposure [130].

[5] It should be noted that this device has only a single contact, i.e. no reverse biased section was used.

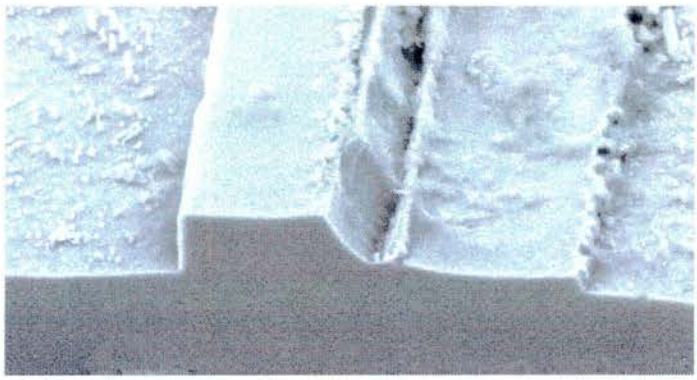

Fig. 8.7: An endview of a SWSA device. The ledge to the right of the narrow deeply etched waveguide is the remains of the shallow waveguide initially etched.

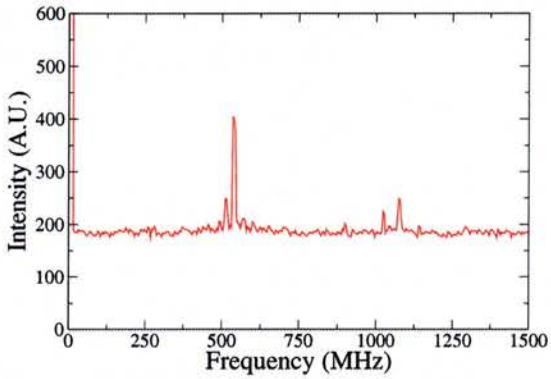

Fig. 8.8: Self pulsing of a laser with a Sidewall Recombination Saturable Absorber. The length of the narrow section was 100μm, the gain section 500μm and the taper was 200μm. The current was 175mA.

loss of such a waveguide has been measured to be $\approx$30 cm^{-1}, using the Fourier Transform technique of [77]. This is undesirably high and clearly the device performance would benefit from reduced loss. A solution to this would be to replace the SU8 deep etch mask with a Nickel mask put down using an electron beam liftoff resist.

Additionally, we believe that there was imperfect matching between the waveguides resulting in reflections at the interface. (When viewed with an infrared camera, light was seen to be scattered at the interface).

A faster taper would also be advantageous as the unpumped tapered section is an considerable source of loss (without benefit), which degrades the overall efficiency of the laser. A fast taper over 10-50μm has been proposed and modeled [131] which could improve the performance of this device.

This device was not observed to modelock, perhaps as a result of a larger than optimum depth of modulation in the saturable absorber or else due to reflection at the interface with the taper. However, this device demonstrates a new method of causing a semiconductor laser

to pulse. Through an optimisation of the fabrication process and the depth of modulation of the saturable absorber, it should be possible to use this technique to modelock the device.

8.5 Deep etched Quantum Dot Waveguides

IT HAS been observed that quantum dot material may be deeply etched with very little loss in carriers to sidewall recombination [132]. The reason for this is that carrier movement is much restricted in a quantum dot material due to their continual capture by and escape from the dots resulting in a reduction in the diffusion length and also the surface recombination velocity due to a reduced interaction with the sidewalls.

8.5.1 Fabrication

SIMILAR TO the process used in section 8.3, varied width, 2-10μm, mesa lasers were created in Quantum dot (DO-451), (the etch depth was 2.2μm), see section 10.5 for a description of the process. For these devices, insulation was provided using a layer of BCB. This was then etched back using RIE with an SF6/O2 plasma until the mesas were just exposed, resulting in self aligned insulation pads. (Due to wider mesas of the Quantum well devices, this self-aligned process does not work due to insufficient planarisation). Contacts were then deposited as normal.

8.5.2 Measurements

FROM EQUATION 8.1, it may be seen that as the mesa width decreases, the threshold current increases as the fraction of carriers recombining at the sidewall becomes larger. The experimental dependence of the threshold current density on the mesa width is shown in figure 8.9. Using the more sophisticated model of [133], a fit can be made to this data using the diffusion length and the surface recombination velocity as fitting parameters giving values of 1.2μm and 5×10^4cm s^{-1} respectively[6].

These compare very favourably with Quantum wells, see section 8.3. Thus, narrow mesa devices may be created that demonstrate threshold current densities comparable to that of broad area devices- 140 Acm^{-2} for a 5μm wide device and 122 Acm^{-2} for a 50μm wide device. This makes Quantum dot material an excellent candidate for the creation of the active photonic crystal devices. Also, the prevention of current spreading reduces the capacitance of the resulting device improving its high frequency performance [134].

The slope efficiency of these lasers was about 0.25WA^{-1}- this is less than that of broad area lasers and is probably due to an increase in the loss for the deeply etched waveguide. Through an optimisation of the RIE and CAIBE etch steps and the reduction of any stitching errors during the electron beam writing, it should be possible to reduce this loss and attain a higher slope efficiency.

[5] A hard silica mask was used, as SU-8 mask can result in high sidewall roughness, see above.

[6] The model assumes that there is no dependence of waveguide loss on mesa width. As this may not be true in practice, we measured the loss of each using the Fourier Transform technique of [77]. We found the loss to be constant, within the experimental error, with a value of $5cm^{-1}$.

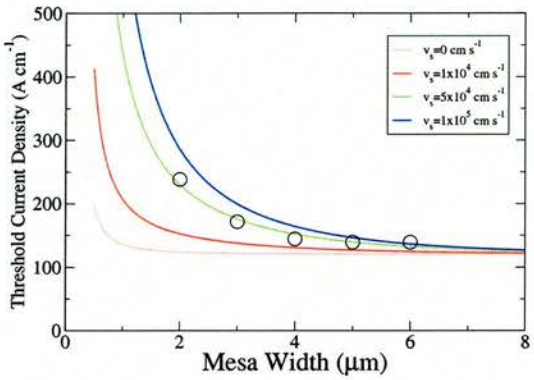

Fig. 8.9: The dependence of the threshold current density as a function of mesa width for a quantum dot material (DO-451). The experimental data data points are shown as circles with the curves showing the theoretical curves for various values of the surface recombination velocity.

8.6 Conclusion

IN THIS chapter, we looked at devices which use very different aspects of the same physical process. We have shown that sidewall recombination may be used as a means of recovery for saturable absorbers. This allows the creation of a new type of pulsed laser that uses neither a reverse biased or ion implanted section. We have demonstrated self-pulsing behaviour in such a laser and we believe that through more efficient fabrication and design (particularly of the taper), the correct depth of modulation will be found which will allow modelocked operation. These devices would have a number of advantages, for instance a simpler device layout (i.e a single contact) and a saturable absorber with more efficient recovery (no screening of the electric field).

In the second half of this chapter, we look at the effects of sidewall recombination on narrow waveguides in Quantum dot material. Due to the nature of Quantum dots, this effect is minimised, allowing the use of highly effective narrow waveguides with very strong optical confinement. With this development, the double etch step previously used to make lasers incorporating photonic crystals is no longer necessary and may replaced with a single etch step[7]. Using this method, quantum dot lasers with photonic crystal mirrors have been created which had the same total slope efficiency (from one facet) as quantum dot lasers with as cleaved facets (output taken from both). Additionally, this widens the range of device geometries which may be used- for instance, ring lasers with tighter bending radii will be possible. This also has potential for the creation of lasers incorporating photonic crystal and other active photonic crystal devices.

[7] Furthermore, from a fabrication point of view, a simplification of the process is always favourable.

9. KERR MODELOCKING

9.1 Introduction

IN THIS chapter, we discuss a method of producing shorter pulses from a semiconductor laser. By increasing the effectiveness of the modelocking mechanism i.e. the saturable absorber, a greater amount of pulse shortening per pass (known as the pulse shortening rate), may be achieved. While this is a "brute force" method, lacking the subtlety and elegance of chirp compensation, it has been shown in other systems to be a highly effective method of producing shortened pulses.

In the 1980s, Colliding Pulse Modelocking (CPM) [2] was introduced in dye laser systems and later in solid state systems, leading to, at those times, the shortest pulses. This was due to an increased pulse shortening rate as a consequence of the increased light intensity in the saturable absorber due to the collision of two pulses. With the development of intracavity dispersion compensation and Kerr-Lens and Saturable Bragg Reflector (SBR) modelocking methods, CPM has largely become obsolete in present solid state lasers systems.

It is informative to note, however, that in monolithic semiconductor lasers, CPM is still the premier method of producing short pulses [46], see figure 1.3. It may, therefore, be deduced that following the example of macroscopic laser systems, shorter pulses may be achieved through improvements to the saturable absorber.

The work of Tropper *et al.* in surface emitting semiconductor lasers [45], also suggests some additional advantages of strengthening the modelocking element. The propagation of ultrashort pulses ($\approx 500ps$ and shorter) in semiconductor medium can lead to some very complex chirping effects due to effects related to the finite intraband relaxation time and other phenomena [34]. Effective chirp compensation in such cases is difficult [35]. Tropper *et al.* have demonstrated transform limited 620 fs pulses from their system which uses the AC Stark effect in a Saturable Bragg Reflector. This implies that this complex chirping is relatively weak in magnitude compared with Self Phase Modulation induced chirp[1](SBR modelocking in edge emitting semiconductor lasers is not as effective) thus allowing it to be overcome by a strong pulse shortening rate.

Following the example of macroscopic lasers systems, we consequently think it advantageous to attempt to introduce Kerr effect modelocking to semiconductor lasers. In this chapter, using the numerical model developed in collaboration with Michael B. Flynn (described in chapter 2), we describe a method of using this effect to produce shorter pulses from a monolithic semiconductor laser.

[1] By its surface emitting nature, the system of Tropper *et al.* avoids large amounts of SPM.

9.2 Basic Idea

KERR LENS modelocking has been demonstrated to be a very successful method of producing short pulses [3]. The gain material of the laser shows a moderate Kerr nonlinearity where the change in refractive index n induced by an optical field intensity I is given by:

$$n = n_0 + n_2 I, \tag{9.1}$$

where n_0 is the linear refractive index and n_2 is the Kerr coefficient. A high intensity pulse incident on this material may cause self-focusing, see figure 9.1. The pulse then experiences a reduced loss on passage through an aperture. Lower intensity light sees a much greater loss. This behaviour simulates a fast saturable absorber, as the Kerr effect, due to its electronic nature, is near instantaneous ($\approx fs$) [115].

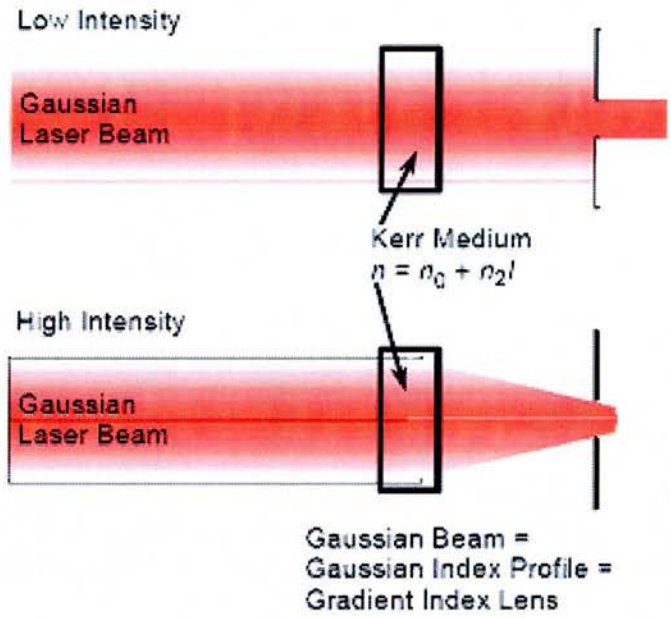

Fig. 9.1: An overview of Kerr Lens modelocking. High intensity pulses cause self-focusing and experience a reduced loss relative to CW lasing. Reproduced from [52].

We would, therefore, like to incorporate a variant of Kerr lens modelocking in a semiconductor laser. There are three requirements: a suitable nonlinear material, a method of integrating it and a design which can make use of this nonlinearity.

We use, as our starting point, the deeply etched Bragg mirrors of chapter 3.5 and [78], see figure 9.2. The stopband of such a mirror is shown in figure 9.3. The position of this stopband is dependent on the lengths of the two sections and their refractive indices. This leads us to a method of realising Kerr modelocking, if one of the sections has a strong n_2 coefficient (equation 9.1), then the position of this bandgap may become a function of the incident pulse intensity.

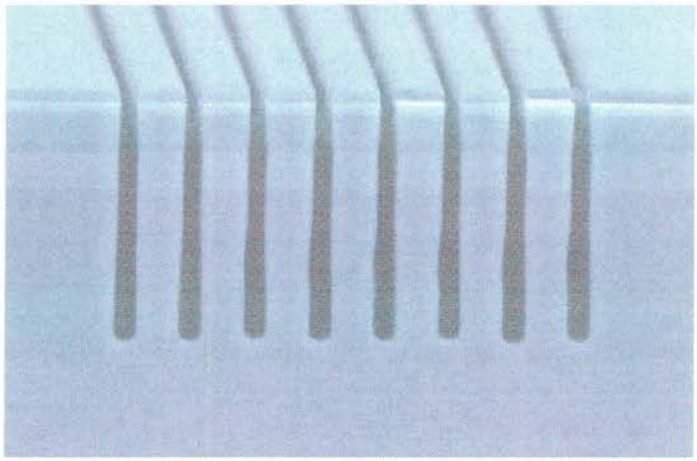

Fig. 9.2: A deeply etched bragg mirror of chapter 3.5. This was created using CAIBE.

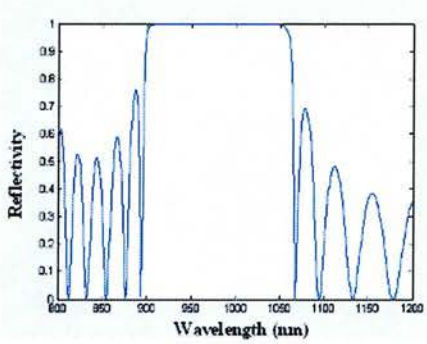

Fig. 9.3: The reflection from a mirror such as that shown in figure 9.2. The position of this stopband depends on the refractive indices of the two components as well as their lengths.

Figure 9.4 shows how this may be used. The bandgap is positioned so that for low intensites, the lasing wavelength is just off the bandedge, figure 9.4a. High intensity light may shift the bandgap relative to the lasing wavelength, and thus experience the high reflectivity portion of the bandgap.

9.3 Design

9.3.1 Asymmetric Mirrors

THE SIMPLE design of figure 9.4 will not work due to the width of the semiconductor gain curve. In the normal situation, with cleaved facets, the device will lase at the peak of the gain curve. In the case of our initial design with a single Bragg mirror, the device will lase at the maximum of the combined gain-reflectivity curve, i.e. it is unfavourable for the laser to operate at such a low reflectivity position on the mirror, see figure 9.5. In practice, it will sacrifice some of the gain and shift to the nearby high reflectivity.

The straightforward solution to this would be to use a Distributed Bragg Reflector (DBR)

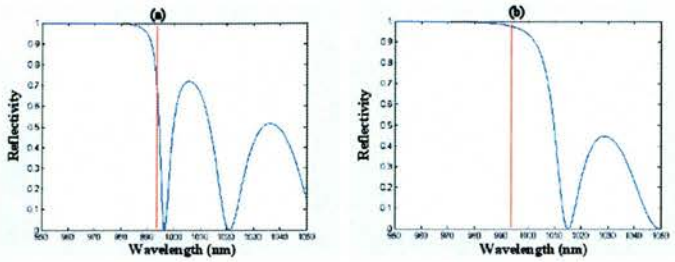

Fig. 9.4: a) A low intensity pulse incident on the mirror will see a low reflectivity. b) A high intensity pulse shifts the position of the bandgap and experiences a much higher reflectivity. The lasing wavelength is shown by the red vertical line.

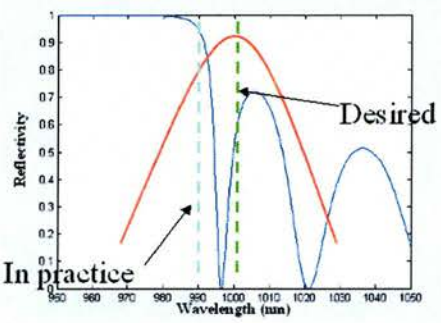

Fig. 9.5: It is unfavourable for the device to lase at the desired wavelength. It will, instead, lase at maximum of the gain-reflectivity curve. The gain curve is shown in red. If the product of the blue and red curves is considered, it will be seen, the value for 990nm will exceed that at 1000nm. For our design to work, a method of holding the lasing wavelength at a lower reflectivity is neccessary.

at the opposite end of the cavity. Due to the low contrast and large number of periods, this can very accurately define the lasing wavelength of the device. However, these devices involve a difficult etch and regrowth step and can be inherently bandwidth limiting (due to the low contrast). In consequence, it would be preferable to use another deeply etched Bragg mirror.

We, therefore, intend to use an asymmetric mirror design, see figure 9.6. This involves the use of two mirrors, the periods of each chosen such that the bandgaps are offset from one another with only a small overlap between the two. The device will then lase at the maximum of the cavity reflectance, $\sqrt{R_1 R_2}$, see figure 9.7a, assuming that the gain curve matches. If the two do not match, then the lasing wavelength will be dragged over to one side slightly, though this is now unimportant (at least theoretically). One of the mirrors should then be nonlinear so that a high energy pulse increases the overlap[2], see figure 9.7b.

It might be envisaged that these mirrors may be fabricated by lithographically tuning one of the mirrors [135]. By choosing the tuning step fine enough, it should be possible to achieve the required overlap.

[2] Only one mirror should be nonlinear. If both are nonlinear, then the pulse will shift both in the same direction and no increase in overlap will be obtained. This process is, in fact, useful. A semiconductor material has many nonlinearites, such as its own Kerr effect and carrier related refractive index change,

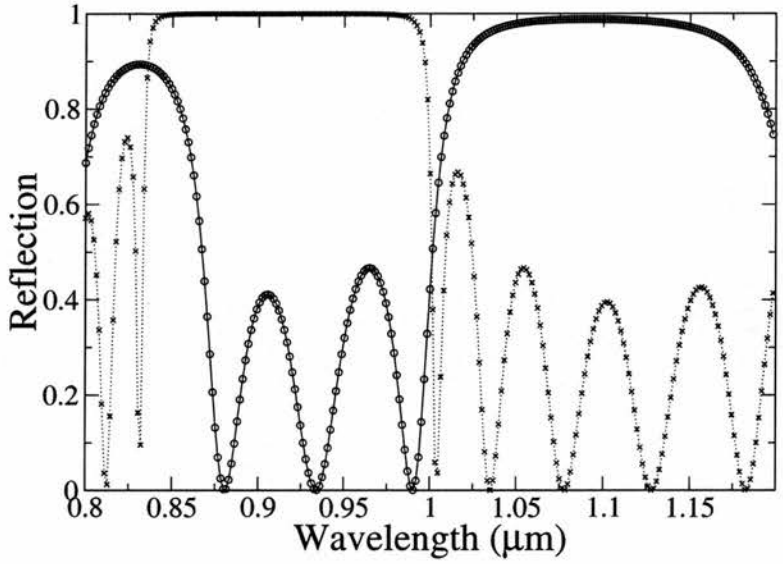

Fig. 9.6: The bandgaps of the two mirrors show only a small overlap at low light intensity. Crosses indicate the back mirror and circles the polymer-filled front mirror.

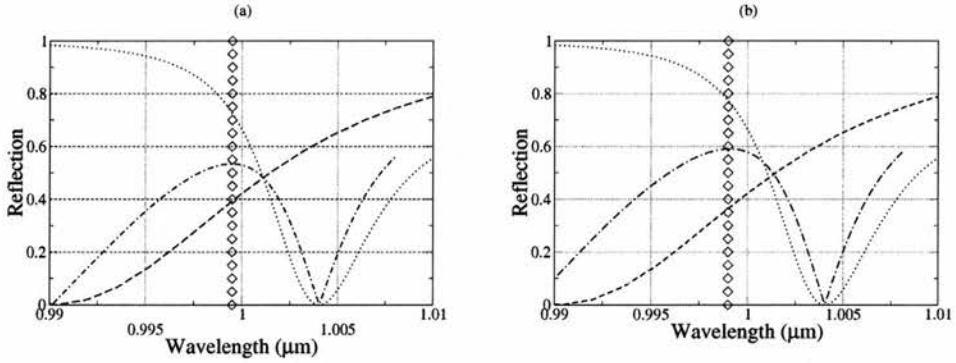

Fig. 9.7: (a) the unshifted case, (b) under the influence of a high energy pulse that causes a refractive index change of -0.005. The dotted line corresponds to the rear unfilled mirror, the dashed to the front polymer-infilled mirror and the dot-dashed to the total reflectance. The vertical line (diamonds) indicates the lasing wavelength.

9.3.2 Nonlinear Polymers

USING A polymer with a strong Kerr coefficient is a promising method of making one of the sections of the Bragg mirror nonlinear. To my knowledge, the largest Kerr coefficient are exhibited in polymers. Also, the mechanical properties of polymers allow a straightforward method of incorporating them.

which could act against pulse formation. However in this design, the effects of these will cancel out over the two mirrors.

Figure 9.8 shows a polymer (SU8 in this case) filled mirror. While imaging using the SEM, a contamination spot was burnt (the beam was focused onto one spot for a few seconds) verifying that the polymer is in fact filling the feature. The mirror is filled with polymer using an embossing technique, see section 5.3.

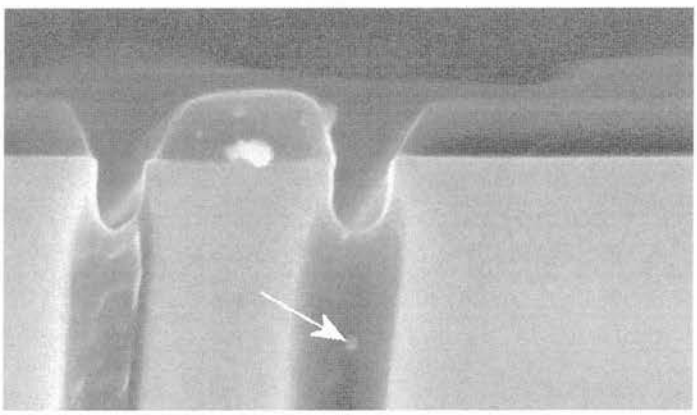

Fig. 9.8: A scanning electron microscope image of a polymer infilled photonic crystal. A contamination spot (marked) has been burnt confirming that the polymer fills the feature.

There are a number of potential polymers that could be used. For example, Polycarbonate is reported to have a n_2 of -2.99×10^{-11} cm^2W^{-1} [136]. Polydiacetylene in crystalline form has a n_2 of 3×10^{-8} cm^2W^{-1} [137]. Soluble forms exist but with a reduction in the value of n_2. Soluble polymers with even stronger n_2 values, such as dialkylaminonitrodiphenylpolyene -DANS (7×10^{-8} cm^2W^{-1}) are reported in [138]. A summary of these is given in table 9.1. A number of liquid crystals have very high n_2 values, though the response time of these are very slow.

The problem of photostability must be considered, since the polymers examined in [138] have a shorter life than would be required for commercial use [139]. Polycarbonate should be more resilient, in this respect, as its peak absorption (295 nm, 345 nm) [140], is further from the wavelengths of interest than that of DANS (approx. 500 nm), yet its n_2 value is already sufficient to produce a significant improvement, see figure 9.11.

Polymer	n_2 (cm^2W^{-1})	Reference
Polycarbonate	-2.99×10^{-11}	[136]
Polydiacetylene	3×10^{-8}	[137]
Dialkylaminonitrodiphenylpolyene	7×10^{-8}	[138]
GaAs	3×10^{-13}	[141]
TiSaf	10^{-20}	[142]
Fused Silica	10^{-20}	[115]

Tab. 9.1: A comparison of the Kerr coefficients for a variety of polymers. Also included are the values for GaAs, Ti:Sapphire and fused silica.

The Kerr coefficient of the polymer could be enhanced in the Bragg mirror as a result of the reduction in the group velocity, see figure 9.9. Very low group velocities have been observed in one-dimensional photonic bandgap structures [143]. The successful realisation

of this is probably a long term project. However there are two other photonic crystal effects which we may make use of. For the nonlinear mirror, the low-index region may be chosen to be large in order to increase the interaction of the light with the polymer. The mirror period of the polymer can be chosen such that lasing takes place at the shorter wavelength edge of the bandgap. This results in the majority of the light building up in the low index regions thereby enhancing the influence of the polymer.

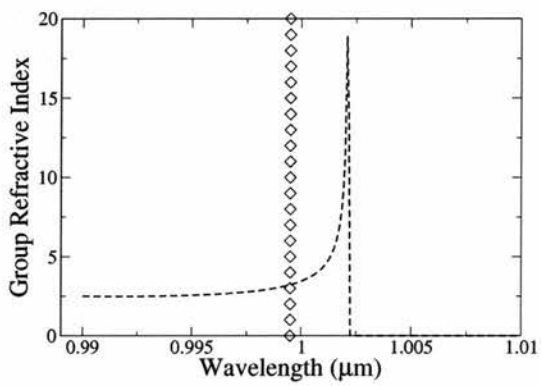

Fig. 9.9: This shows the dispersion of the polymer filled mirror approaching its band edge. Calculated from the group velocity following [144]. The lasing wavelength is indicated by a vertical line (diamonds).

9.4 Theory

WE USE THE model descibed in section 2.5 to examine the possibilities and potential of these devices. We implement the intensity dependent reflectivity of the polymer filled mirror by replacing the standard boundary condition for one mirror with one of the form:

$$R = 0.5 + C\frac{S}{AS_{1W}}n_2 \tag{9.2}$$

where C is a constant determined by the slope of figure 9.10, S_{1W} is the photon density corresponding to power of 1 W and A is the waveguide area (taken to be 5 μm$\times$0.2 μm)[3].

As an accurate representation of the interaction of light with the polymer is vital to the practical value of this model, we deviate from the normal method of calculating the power output from the photon density. Instead, we use an empirical approach directly relating our modeled output power to that observed in real devices (5 mW average power for a normal two-section device), through the conversion factor in equation 9.2. The calculations assume that this corresponds to an intra-cavity value of approximately 10 mW (the mirror has a reflectivity of approximately 0.5). We take the waveguide confinement factor Γ to be 0.6, calculated from a real device design using a commercial eigenmode solver (FIMMWAVE). In addition, the nonlinear response of the polymer is taken to be instantaneous.

[3] A term to prevent a reflectivity greater that one was also included.

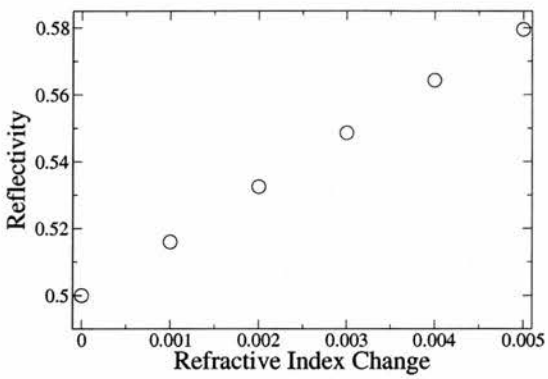

Fig. 9.10: Figure showing how the total cavity reflectance changes with the polymer refractive index change.

Including the wavelength dependence of the reflection from the mirrors is a very complex task and goes beyond the scope of this model. As the gain bandwidth of the material is usually much larger than that of the pulse, this spectral change will have little effect on the gain experienced by the pulse. However, the change in spectrum on reflection will perturb the pulse and would most likely result in additional chirping. It is unlikely to have more serious consequences, such as the prevention of mode-locking, as this wavelength dependent reflection will cancel out over a roundtrip limiting the effect. Furthermore, as this perturbation is related to the mirrors, it will be less important the longer the device.

There would also typically be a net dispersive effect on reflection from the mirrors (a portion will cancel out over a round trip, as for each mirror, reflection occurs on opposite sides of the bandgap), see figure 9.9. As the lasing wavelength is relatively far from the mirror band edge, the overall dispersive effects are very small, i.e. a few femtoseconds per nanometre, and are negligible compared to the effects of SPM. Our model, therefore, ignores these effects.

As mentioned earlier, see section 6.3.1, at the current point in time SPM induced chirp is the main obstacle to monolithic ultrashort pulses. While this phenomenon is described by our model, the model is not sufficiently complex and does not include sufficient terms to describe the effects related to the intraband relaxation time. These become important for pulses shorter than $\approx 700fs$, [34]. In this section, we use our model to study the possibility of using Kerr Modelocking to overcome the effects of SPM. It is beyond the scope of the model to quantitatively predict its ability to produce subpicosecond pulses[4].

9.4.1 Hybrid Kerr Mode-locking

LOOKING AT the results of the model in detail shows that it takes a reflectivity increase of approximately 25 percent to initiate mode-locking. Much less (1-2 percent) is necessary

[4] However, we will later give an intuitive argument which suggests that Kerr Modelocking may in fact do so.

to sustain Kerr mode-locking and shorten the pulses once pulsing has started. This occurs because the pulse shortening rate (mode-locking strength) is proportional to the induced reflectivity change which in turn depends on the intensity of the incident pulse. Thus, initially, as pulsing coalesces out of noise spikes, the peak intensities are low resulting in a self starting problem,(following [7] which approximates the effects of a Kerr medium as a fast saturable absorber). Therefore, a hybrid system that uses a saturable absorber to begin pulsing and a nonlinear mirror to shorten pulses may be of more use than a pure nonlinear mirror laser, which would require polymers with a very large n_2 value, see section 9.4.2.

Figure 9.11 shows how the pulse duration varies with the Kerr coefficient of the polymer. For low values of n_2 (less than approximately 2×10^{-11} cm^2W^{-1}), the strength of the Kerr mode-locking is weak compared to the effect of the saturable absorber and the pulse duration is only fractionally reduced. For values of n_2 above a magnitude of approximately 2×10^{-11} cm^2W^{-1}, the intensity of the light is sufficient for the Kerr effect to start shortening the pulse dramatically. The nonlinear reflectivity change is governed largely by the n_2S term in equation 9.2. This value can depend on the repetition rate of the laser- by using a longer device a higher peak power can be achieved even with the same average power output.

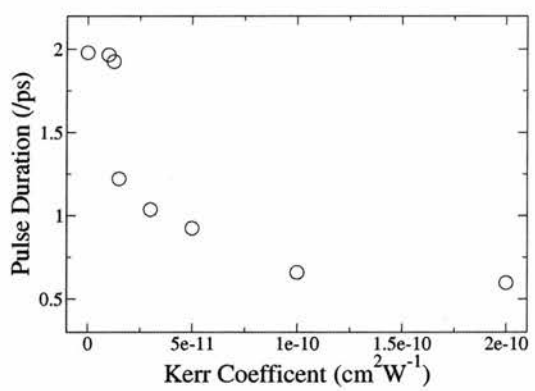

Fig. 9.11: Pulse width with respect to Kerr coefficient in the hybrid case. This clearly shows the transition between saturable absorber mode-locking and Kerr effect mode-locking. This device had a 3000 μm gain section and a 300 μm absorber.

The simulation in figure 9.11 uses a 3000 μm gain section and a 300 μm absorber section. If a shorter (1000 μm) device was used, the threshold n_2 for Kerr mode-locking to become noticeable would be more than doubled- see figure 9.12, (crosses). This device was also predicted to operate in the Q-switched modelocking regime (see section 7.1)- this aspect will be discussed in more detail later.

9.4.2 Pure Kerr Mode-locking

IN THIS SECTION, we look at the case where the Kerr coefficient is large enough to start mode-locking on its own. In figure 9.12 we show the results of modeling a device consisting of a 1000 μm gain section (no saturable absorber) with various Kerr coefficients. For com-

parison a similar hybridly mode-locked device is also shown. For values of n_2 below approx. $5.5\times10^{-10}\text{cm}^2\text{W}^{-1}$ no pulsing is observed for the pure Kerr mode-locked case. The pulse shortening rate of a fast absorber is typically proportional to the peak intensity meaning the shortening rate is initially very small [32] and hence the pulse width is long. In a fast saturable absorber (the effect of which is simulated by Kerr-lens mode-locking [7] and our Kerr mode-locking), the pulse shortening rate is directly proportional to the peak pulse intensity and thus the inverse of the pulse duration [32]. As a result, the effectiveness increases with shorter pulses. In contrast, the effects of a slow saturable absorber are constant with respect to the pulse width- the enhancing effects of higher peak powers are counteracted by the increasing ratio between the saturable absorber's recovery and the pulse width. As the pulse gets shorter, the increased peak intensity saturates the absorber "better"- simultaneously, the ratio between the pulse duration and absorber recovery time increasing making the absorber less able to shape the pulse. Thus, a very large Kerr coefficient is required to initiate mode-locking from low peak intensities. Once pulsing begins, the peak power levels almost immediately reach a very high level, giving a very large pulse shortening rate and hence very short pulses, see figure 9.12.

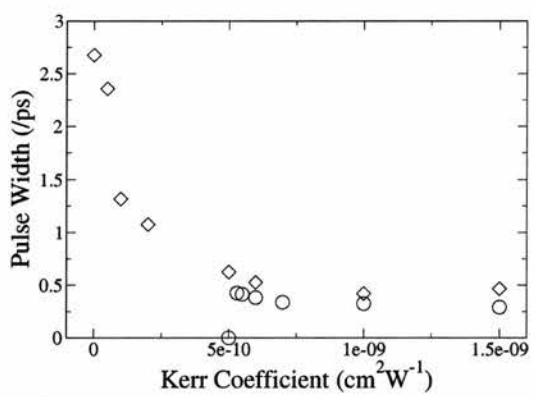

Fig. 9.12: Graph showing how the pulse shortens with increasing n_2. Crosses show a hybridly mode-locked device and circles a purely Kerr mode-locked device. This was measured for devices with a gain length of 1000 μm. The hybrid device had a saturable absorber of length 100 μm. Note the increase in the threshold n_2 for the hybrid device compared with figure(9.11). For the pure Kerr modelocking trace, no modelocking occurs below a certain strength of polymer (indicated by zero pulse duration).

The hybridly mode-locked device always produces longer pulses than the pure case for the same n_2 value (once the purely Kerr mode-locked device is above its threshold). There are two possible reasons for this: either the saturable absorber increases the magnitude and/or the complexity of the SPM induced chirp or as a result of absorption in the saturable absorber the pulse sees weaker pulse shortening as a result of its lower peak intensity. Figure 9.12 demonstrates another feature of this device- the pulse width of the hybridly mode-locked case appears to start increasing above a certain value of n_2. The hybrid device operated in a Q-switched mode-locking regime, which typically produces peak intensities 3-4 times higher than that of the comparable CW mode-locking regime, whereas the pure Kerr mode-locked

device is CW mode-locked. Thus the hybrid device reaches a peak intensity at which the nonlinear mirror saturates and the pulse centre no longer experiences any shortening effects. For sufficiently high n_2, the pure device also exhibits such behaviour. However, this is a somewhat artificial problem as the mirror used in the above simulation was designed to amplify the effects of a weak polymer. With polymer strengths corresponding to those of figure 9.12, the initial overlap between the bandgaps should be reduced (the unsaturated value of R was 0.5 in this case, see equation 9.2) making the mirror capable of shaping the pulse over a wider range of peak intensities.

In general, we find the parameter ranges which result in Q-switched modelocking to be much wider in Kerr mode-locked devices (particularly so in the hybrid design) than those for standard two-section devices [70], (also discussed in section 7.1). Q-switched mode-locking is undesirable in many applications, thus in each case (i.e. for the actual n_2 value) section lengths and currents should be chosen following the guidelines described earlier. In addition, Kerr mode-locking has the additional parameter of the position of the lasing wavelength relative to the bandgap of the nonlinear mirror. Careful adjustment of these should allow the avoidance of Q-switched mode-locking.

The shortest pulses produced by the simulated devices had a duration of 290 fs, a spectral width of 7 nm and a time-bandwidth product of 0.63.

9.4.3 Mode-locking using a Resonant Polymer

IF THE ENERGY of the incoming light is close to that of an excitonic resonance of the polymer, the effect of the exciton alters the nonlinear response. This can result in a nonlinear refractive index which is much larger than the nonresonant value (by as much as four orders of magnitude). However, this effect is typically slower than the nonresonant case. Polydiacetylene, mentioned previously- table 9.1, has a relaxation time of 2 ps [137].

We incorporate this effect into our model using a simple differential equation:

$$\frac{dR}{dt} = \frac{R_{inst} - R}{t_{rel}}, \tag{9.3}$$

where t_{rel} is the polymer relaxation time, R is the reflectivity of the nonlinear mirror and R_{inst} is the value corresponding to a polymer which reacts instantaneously. With this alteration, the system now resembles one that uses a slow saturable absorber. However, unlike the saturable absorber in the conventional two-section configuration, which typically interacts with only 3 percent of the light that passes through it, the polymer, as it is contained in an end mirror, can interact with most of the light, giving stronger mode-locking. This, coupled with the pulse shortening effects at the trailing pulse edge due to gain saturation (enhanced in this case due to the shorter pulse and higher peak power), allows the polymer to remain highly effective. This results in only a slight increase in pulse duration when the polymer has a non-zero relaxation time (approx. 20 fs for a relaxation time of 5 ps). Polydiacetylene has a crystalline form and as a result, it is likely that incorporation into the mirror may cause a significant reduction in the n_2 value (involves the use of nanocystals suspended/dissolved in a polymer). However, our modelling shows that significant shortening may be observed for an n_2 as low as 10^{-10} cm^{2}W^{-1}. This is two orders of magnitude less than the maximum

recorded value, and should be achievable in practice.

9.5 Conclusion

IN THIS CHAPTER, we have proposed a design for a monolithic diode laser capable of producing subpicosecond pulses. As demonstrated by Tropper *et al.* [45] and Martins *et al.* [46], increasing the mode-locking strength is an effective means of shortening pulses. The device considered here makes use of perhaps the strongest possible form of mode-locking, i.e. Kerr effect mode-locking.

Whereas the lithographic tuning required to fabricate the photonic bandgap mirrors to the required tolerance and the incorporation of a suitable polymer [5]will entail much time and effort, the currently available technology is sufficient to produce devices with better performance than those available using only a reverse biased section as the saturable absorber.

We have considered here, a stripe geometry ridge laser (5μm wide), as this is most suited (by its relative ease of fabrication) to the experimental realisation. However, using buried heterostructure lasers, a much higher power concentration may be achieved (potentially a better than five-fold improvement). This would widen the range of the suitable polymers, increasing the possibility of finding one with suitable characteristics (physical properties such as solubility, damage resistance, etc).

The time-bandwidth product of the simulated pulses was typically twice the transform limit. Increasing the mode-locking strength results in only a slightly shorter pulse with approximately the same time-bandwidth product. This suggests that some form of dispersion compensation is necessary to efficiently shorten the pulse further.

As the model does not include terms to describe ultrafast processes which become important for subpicosecond pulses, such as those related to the finite intraband relaxation time (100 fs), and the effects of the complicated reflection of the mirror, we expect, in practice, that the produced pulses would be somewhat longer than those predicted. However, as mentioned in the introduction to this chapter, this complex chirping can be overcome in surface emitting systems which use an SBR [45] producing transform limited pulses. This is interesting as SBRs have not been able to overcome SPM in edge emitting systems[145]. This indicates that the complex chirping due to ultrafast gain dynamics is much weaker than the simple chirp (often linear [40]) that results from SPM. Our Kerr modelocked design has been shown to overcome much of SPM induced chirp. Thus, this does suggest that Kerr modelocking has a strong possibility of overcoming this ultrafast gain dynamic chirp.

We have demonstrated the potential of Kerr mode-locking using three very different forms of polymers. Whereas the problem of photostability remains, the versatility of this design gives the possibility of finding a polymer with the desired properties.

Furthermore, if a damage resistant polymer with n_2 greater than 1×10^{-9} cm^{2}W^{-1} becomes available, then the potential of Kerr modelocking greatly expands. Instead of having to choose designs to amplify the Kerr coefficient, as we have done here, a design which

[5] Incorporating the polymer into only one mirror presents its problems. Filling both mirrors presents little trouble, however, removing polymer from one mirror or preventing its filling, will add at least another two steps to the process.

minimises the pulse duration can be chosen. For instance, by reducing the initial mirror overlap, improved pulse shortening could be achieved. This may increase the self-starting problem, however a more satisfactory solution than a saturable absorber section may be to use a series of sub-harmonic gain switched pulses to trigger passive modelocking.

Thus, we argue that Kerr modelocking may be able to overcome the complex chirping which has defeated other techniques. In combination with a chirp compensating scheme, such as that described in section 6.3.2, much of the strong linear SPM-induced chirp may be removed, there is a strong possibility that very short (<200fs pulses) can be produced. Whereas as the proposed device is of a complex nature, requiring demanding fabrication, it is, to the best of our knowledge, the only such device, theoretical or experimental, which has the potential to overcome the considerable obstacles presently preventing the realisation of a true monolithic femtosecond diode laser.

10. CONCLUSION

IN THIS THESIS, we have examined modelocked semiconductor lasers and the improvements in performance to be gained through the integration of photonic crystals and other microstructures.

Over the course of this PhD the techniques and processes required for the fabrication of modelocked semiconductor lasers were developed at the University of St Andrews for the first time. In the process, three new fabrication techniques were examined which enhance the performance and versatility of photonic cyrstals (chapter 5). The high voltage low current regime of Chemically Assisted Ion Assisted Ion Beam Etching improves the quality of photonic crystal which may be created in GaAs- and InP- based material. The use of spun on Hydrogen Silsesquioxane as a substitute for silica masks deposited using Plasma Enhanced Chemical Vapour Deposition is attractive for a number of reasons. It is a very simple, versatile, inexpensive process. It is also less damaging to the electrical properties of the device, making it the preferred option for use in active devices. Polymer infilling of photonic crystals adds another level of functionality. The inclusion of nonlinear material may considerably alter the response of a photonic crystal. This may also be used to simplify the fabrication process and allow more straightforward contacting of active devices contain photonic crystals.

Techniques for modelling modelocked semiconductor lasers were also developed, which allowed a greater understanding of their behaviour. Using this model, a study was made of Q-switched modelocking in semiconductor lasers. Guidelines were formulated, such that this regime may be avoided or attained as desired. Indepth study of this model also allowed the determination of the obstacles that prevent the generation of ultrashort pulses and suggested means by which these problems may be overcome.

This led us to the conclusion that a greater degree of intracavity control was necessary (following the example of ultrafast solid state lasers, dye lasers and external cavity semiconductor lasers). We have considered the advantages of a different semiconductor gain medium, i.e. Quantum Dots, but conclude that the main obstacle lies elsewhere. The only method of achieving this control in a monolithic system is through the use of photonic crystal elements and related microstructures. For example, if one was to give a solid state laser to an expert in the field and *prevent him/her from putting their hands into the cavity* to adjust mirrors, add/remove components etc., it would not be reasonable to expect ultrashort pulses. This, however, is the current state of affairs in the field of monolithic semiconductor lasers. Yanson *et al.* were one of the first to attempt to correct this situation, when in 2003, 2.1 THz modelocking was generated using intracavity photonic bandgap mirrors. This thesis has developed a number of similar methods that give enhanced control over the cavity of a

monolithic semiconductor laser.

The use of a Quantum well gain material poses many problems for ultrashort pulse production and propagation. Their strong gain is strongly coupled to refractive index resulting in high SPM. However, high SPM need not be disadvantageous as it broadens the spectrum of the generated pulses thus potentially allowing shorter pulses. It has been shown that a laser produces the shortest pulses when the net cavity group delay dispersion is slightly negative. Photonic crystals have been shown to have considerable dispersive properties. Thus, the integration of a suitable photonic crystal element may be able to provide the required dispersion compensation.

The creation of monolithic chirp compensating structures may appear simple. The use of shallow DBR type gratings might be envisaged, however the low contrast forces the use of very long sections which even then struggle to provide enough chirp compensation to be useful in highly dispersive semiconductor lasers. They may also impose bandwidth limitations. The integrated Gires-Tournois Interferometer/Fabry-Perot Interferomether proposed in chapter 6, successfully achieves sufficient compensation to be useful and is very simple in its fabrication. However, its low bandwidth will prevent the realisation of sub 200-400fs pulses (depending on the operating wavelength). To broaden the application of such mirrors, a method using a lateral DBR would be preferable in quantum dot lasers (taking advantage of their low surface recombination velocity, chapter 8). These could also be pumped which would provide gain to overcome any loss that be be incurred. These may achieve a wide range of refractive index contrasts, from the short deeply etched one dimensional photonic crystal design to the low contrast DBR structures of hundreds of periods. This would allow the creation of mirrors with genuinely chirped periods which may attain almost any chirp compensation, including double chirping, see figure 10.1. Furthermore, as there are no obstacles to pumping the mirror section, there is little limitation on the DBR length.

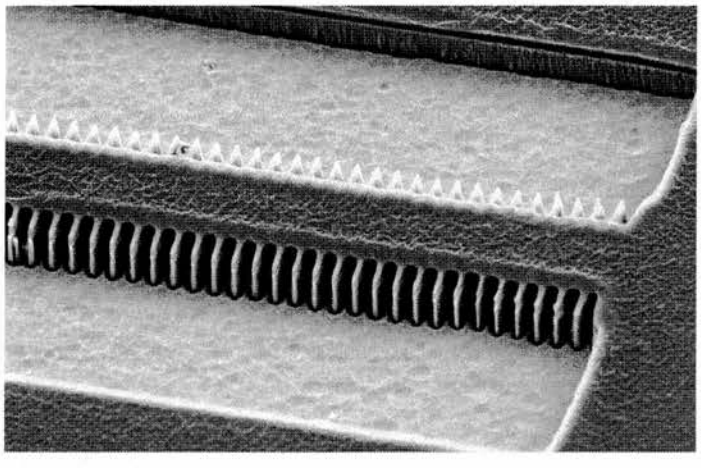

Fig. 10.1: A mirror in which the refractive index changes are provided by varying the waveguide width. This structure has considerable promise for the creation of chirp compensating mirrors.

The waveguide saturable absorber currently in use has a weak pulse shortening rate as a result of its low absorption cross section. Increasing the pulse shortening rate, while in-

elegant compared with chirp compensation, is extremely effective in producing ultrashort pulses. Colliding Pulse modelocking is one method by which this may increased. This technique, though it has been largely superseded in macroscopic lasers by SESAMs, Kerr Lens modelocking and chirp compensation with prisms and dielectric GTI, currently produces the shortest pulses in monolithic semiconductor lasers.

A mirror based saturable absorber which would have a larger absorption cross section might be preferable. The polymer infilling technique of chapter 5 allows the filling of a Bragg Mirror with a saturable absorber dye doped polymer. This would be analogous to the macroscopic SESAM. However, the quantities of dye that may be included are very small and initial experiments were not encouraging. In chapter 9, a similar but different approach is proposed. If the saturable absorber effect is based on the nonlinear refractive index change of the polymer, then the actual amount incorporated becomes less important. This design is extremely promising and has the potential to produce very short pulses. Its main drawback is the nonlinear polymer, those of sufficient strength generally have very poor photostability.

It should be remembered, though, that semiconductor itself is highly nonlinear. The carrier density induced refractive index changes easily exceed that of the nonlinear polymers discussed in chapter 9. This effect is of course slower than the Kerr Nonlinearity, but as discussed in chapter 8, this effect is nevertheless very fast (5ps). An asymmetric mirror design using the carrier density nonlinear refractive index, while offering a small improvement in speed over a reverse biased saturable absorber, would have a much greater absorption cross section and thus may create significant pulse shortening.

Currently, there appears to be some discouragement in the field of ultrashort pulse monolithic semiconductor lasers. Efforts seem to be being concentrated on creating devices that produce useful (though long) transform limited pulses, or else in Vertical Extended Cavity Surface Emitting Lasers that avoid the disadvantages and advantages of edge-emitting devices. Over the course of this thesis, however, we have examined the various options and proposed two feasible designs that may produce ultrashort pulses from a monolithic device.

To conclude, we demonstrated the potential of intra-cavity chirp compensation for the production of ultrashort pulses from a semiconductor laser. We have successfully fabricated such devices and integrated them into a laser cavity, developing several new fabrication techniques in the process. In parallel, we examined the possibility of improving the saturable absorber through the use of a nonlinear polymer filled mirror. While posing a number of difficulties, this design has considerable potential and if used in conjunction with chirp compensation would have a very strong possibility of producing the shortest pulses to date from a semiconductor laser.

10. APPENDIX- FABRICATION PROCESS FLOW

Initially, the wafer is scribed and cleaved into typically 6 mm×6 mm chips. It is then washed in acetone and agitated in the sonic bath. If the sample has a silica coating, the sonic bath should not be used as it may cause delamination of the coating, it should be agitated gently using a pipette instead. The sample is then rinsed in IPA. In general, throughout the rest of the fabrication process, the sample is cleaned whenever possible.

10.1 Photonic Crystals

Before use, a silica mask must be deposited. This is traditionally carried using PECVD, though spin-on glass may also be used.

1. A layer of MicroChem PMMA with a molecular weight 475, is spun onto the sample at 5000rpm and baked for 2 minutes on 180^o hotplate. This is repeated twice in order to build up a coating of the required thickness ($\approx$400nm).

2. A 10nm layer of Aluminium is deposited using a thermal evaporator.

3. The sample is loaded into a hybrid LEO 1530 SEM/Raith Elphy Plus electron beam writer. The working area on the sample is defined.

4. The beam is then alligned and focused to a $\prec$20nm spot size on the sample. This is determined by burning contamination spots.

5. The desired pattern is then exposed. A dose of approx 180μAscm^{-2} is usually suitable, though this varies depending on the pattern, material, mask, etc.

6. The layer of Aluminium is removed in undiluted Phosporic acid. This usually takes about 4 minutes.

7. After exposure is developed in a solution of 3:7 water and IPA for 45s and then rinsed in IPA. This has been shown to be one of the highest resolution developers.

8. The pattern is transferred into the silica mask using RIE at 33W, a pressure of 3×10^{-2}mB, a ring position of 30 and a CHF_3 flow of 200. An etch time of 12 minutes is used for 200nm of PEVCD SiO_2.

9. The remaining PMMA is then removed using acetone or a short oxygen etch in the RIE system

10. The sample is then etched using CAIBE under conditions of 1450V beam voltage, 12mA beam current, 500 Ar flow, 250 Cl_2 flow, chamber pressure of 1-2$\times 10^{-4}$ and a starting substrate temperature of 120°C. The temperature usually climbs by about 10 degrees during the etch. An etch time of 8 minutes is sufficient for most devices.

Photonic crystal creation may be seamlessly integrated with lasers. After the removal of the silica mask using HF, the laser fabrication process may proceed as though the etched sample was untouched. Due to the small size of the PhCs, resists may be usually be spun over them without any degradation of the film quality, (it is sometimes necessary to use a thicker film than usual). Furthermore, they are usually reasonably visible allowing simple alignment using a mask aligner.

10.2 Ridge Lasers

As an aid to handling, the sample is usually mounted on a coverslip. A layer of PMMA is used to attach it. PMMA was chosen as it remains soluble in acetone after processing at all of the temperatures used in the following steps.

1. The sample is spun at 5000rpm with SR1805 photoresist. The sample is then baked on a hotplate for 1 minute at 100°C.

2. Using a Karl Suss Mask Aligner, a series of trenches defining 4 μm waveguides are exposed for 8 seconds. A trench to define the isolator behind the gain and absorber sections is also defined at this point.

3. The sample is then developed in MF319 developer for 20-30 seconds and rinsed in deionised water.

4. It is etched in the CAIBE system using a beam voltage of 350V, a beam current of 10mA, an Argon flow of 500, a Chlorine flow of 250, at a temperature of 120°C. For trenches of depth 500nm, a time of 2-2.5 minutes is usually appropriate, see page 52.

5. The photoresist is then removed using acetone and IPA.

6. The sample is then spun with SU-8 and baked at 100°C.

7. The SU-8 is made to reflow by heating on a hotplate at 130-140°C for 2-5 minutes. This clears most of the polymer from the top of the ridge.

8. Any remaining polymer on ridge is removed using RIE with conditions of 10W, pressure 3$\times 10^{-2}$mB and a O_2 flow of 200. (The ring position is set to 30).

9. The sample is then given a flood exposure for 30s in the mask aligner and baked for 1min on the 100°C hotplate.

10. The sample is then hardbaked in a 180° oven for 10 minutes. This completes the SU-8 crosslinking, helping the mechanical properties.

11. A layer of LOR (Liftoff resist) is spun at 5000rpm and baked for 5 minutes in a 180^ooven.

12. SR1818 photoresist is spun on top of the LOR and baked for 1 minute on a 100^o hotplate.

13. Using the mask alligner, approx. 50μm contact windows are opened on top of the laser ridges by exposing for 28s and developing for $\approx$30s. After the initial 30s the sample is developed for a further 45s- this creates the undercut necessary for liftoff.

14. Immediately prior to contact deposition, the surface of the sample is de-oxidised in 1:1 HCl and water solution for 1 minute and then rinsed in deionised water.

15. The sample is loaded into an Edwards 306 electron beam evaporator and 20nm Ni and 100+nm Au contacts are deposited at pressure less than 2×10^{-5}. The pressure is less than 5×10^{-6} before evaporation is started.

16. The sample is washed in acetone to remove the unwanted metal. The acetone is usually agitated gently using a pipette. The sample is then rinsed in IPA.

17. The sample is mounted face down and deoxidised.

18. An N-type contact consisting of 14nm Au, 14nm Ge, 14nm Au, 11nm Ni and 100+nm Au is then deposited.

10.2.1 Second stage alignment

For some designs, the mask aligner has insufficient precision to align successive processing steps. For such processes the electron beam writer must be used.

1. Suitable alignment marks must be created during the initial processing step.

2. After respinning with an electron beam resist and loading into the electron beam writer, these marks must located.

3. The current positions and the design positions of these marks must be loaded into the software and the working area defined accordingly.

4. Exposure may continue as normal.

5. This may be repeated for multiple alignment steps.

10.3 HSQ masks

HSQ is used here as a substitute for PEVCD silica. Thus it will typically be one of the first processes carried out on a new sample.

1. The sample is cleaned very thoroughly.

2. HSQ (FOx-12) is spin coated at a speed of 5000rpm.

3. The sample is prebaked on 100°C for one minute. This drives off the solvent.
4. It is then baked at on a 300°C hotplate for 5 minutes.
5. This may be repeated as required to build up a coating of the desired thickness.
6. It is then cured on a 500°C hotplate for 1 hour.
7. Processing now continues as with a normal silica coated sample.

10.4 Sidewall Recombination Saturable Absorber

1. Ridge waveguides are created following section 10.2.
2. The sample is then spun with SU-8 and the taper and saturable absorber section defined using electron beam lithography (a second stage alignment).
3. Contact insulation was created using photoresist (SR1818) and an etch back process (section 10.2).
4. Contacts are then put down, taking care to leave the taper and saturable absorber free from metal.
5. The contacts are then protected using a layer of photoresist and the taper and saturable absorber etched to a depth of approx. 2μm using high voltage low current CAIBE.

10.5 Deeply etched Quantum dot mesa lasers

1. A 300nm layer of HSQ silica is put down following 10.3.
2. 5 μm wide trenches defining waveguides of the desired width are created in PMMA using electron beam lithography.
3. This pattern is transferred into the silica using RIE.
4. Mesas are then etched to a depth of of approx. 2μm using CAIBE.
5. The sample is then spun with SR1818, filling the deep trenches.
6. The sample is then etched in an oxygen plasma until the tops of the mesas are exposed.
7. Contact insulation is then completed using a layer of photolithographically defined SU-8.
8. The remaining silica is removed from the mesas using a 1 minute etch in a 1:10 HF to water solution.
9. Contacts are then put down as normal.

LIST OF FIGURES

BIBLIOGRAPHY

[1] B. Agate, *Portable and efficient Cr:LiSaF lasers*, Ph.D. thesis, University of St Andrews, 2003.

[2] R. L. Fork, B. I. Greene and C. V. Shank, "Generation of optical pulses shorter than 0.1 psec by colliding pulse mode locking," *Appl. Phys. Lett.*, volume 38, p. 671, 1981.

[3] D. E. Spence, P. N. Kean and W. Sibbett, "60-fsec pulse generation from a self-mode-locked Ti:Sapphire laser," *Opt. Lett.*, volume 16, pp. 42–44, 1991.

[4] C. Honninger, R. Paschotta, F. Morier-Genoud, M. Moser and U. Keller, "Q-switching stability limits of continuous-wave passive mode locking," *J. Opt. Soc. Amer. B*, volume 16, pp. 46–56, 1999.

[5] C. T. A. Brown, M. A. Cataluna, A. A. Lagatsky, E. U. Rafailow, M. B. Agate, C. Leburn and W. Sibbet, "Compact laser-diode based femtosecond Sources," *New Journal of Physics*, volume 6, p. 175, 2004.

[6] S. Gee, A. Alphonse, J. C. Connolly, C. Barty and P. J. Delyfett, "Ultrashort Pulse Generation by Intracavity Spectral Shaping and Phase Compensation of External-Cavity Modelocked Semiconductor Lasers," *IEEE J. Quantum Elec.*, volume 36, pp. 1035–1040, 2000.

[7] H. A. Haus, "Mode-Locking of Lasers," *IEEE J. Select. Topics Quantum Electron.*, volume 6, pp. 1173–1185, 2000.

[8] Y. Arakawa and H. Sakaki, "Multidimensional quantum well laser and temperature dependence of its threshold current," *Appl. Phys. Lett.*, volume 40, p. 939, 1982.

[9] S. Fathpour, Z. Mi, P. Bhattarcharya, A. R. Kovsh, S. S. Mikhrin, A. V. Kozhukhov and N. N. Ledentsov, "The role of Auger recombination in the temperature-dependent output characteristics ($T_0=\infty$) of p-doped 1.3μm quantum dot lasers," *Appl. Phys. Lett.*, volume 85, pp. 5164–5166, 2004.

[10] D. O. Brien, S. Hegarty, G. Huyet and S. Uskov, "Sensitivity of Quantum Dot Semiconductor Lasers to Optical Feedback," *Opt. Lett.*, volume 29, p. 1072, 2004.

[11] F. Camacho, E. A. Avrutin, P. Cusumano, A. S. Helmy, A. C. Bryce and J. H. Marsh, "Improvements in Mode-Locked Semiconductor Diode Lasers Using Monolithically Integrated Passive Waveguides Made by Quantum-Well Intermixing," *IEEE Photon. Tech Lett.*, volume 9, pp. 1208–1210, 1997.

[12] O. Graydon, "Perfect mirrors give diode breakthrough," *Opto and Laser Europe*, volume 120, pp. 30–31, 2004.

[13] P. P. Vasil'ev, I. H. White and J. Gowar, "Fast phenomena in semiconductor lasers," *Rep. Prog. Phys.*, volume 73, pp. 1997–2042, 2000.

[14] C. Systems, *Introduction to DWDM technology*, Cisco Systems, 2004.

[15] J.-P. Laude, *DWDM, fundamentals, components and applications*, chapter 2, Artech House, Boston, 2002.

[16] D. A. Yanson, M. W. Street, S. D. McDougall, I. G. Thayne, J. H. Marsh and E. A. Avrutin, "Ultrafast Harmonic Mode-Locking of Monolithic Compound-Cavity Laser Diodes Incorporating Photonic-Bandgap Reflectors," *IEEE J. Quantum Elec.*, volume 38, pp. 1–11, 2002.

[17] K. Yvind, *Semiconductor Modelocked lasers for Optical Communication systems*, Ph.D. thesis, Technical Univesity of Denmark, 2003.

[18] R. K. Jain and C. P. Ausschmit, "Subpicosecond pulse generation in a synchronously mode-locked cw rhodamine 6G dye laser," *Opt. Lett.*, volume 2, pp. 117–119, 1978.

[19] H. Kubota, K. Kurokawa and M. Nakazawa, "29-fs pulse generation from a linear-cavity synchronously pumped dye laser," *Opt. Lett.*, volume 13, pp. 749–751, 1988.

[20] J. Goodberlet, J. Wang, J. G. Fujimoto and P. A. Schulz, "Femtosecond passively mode-locked Ti:A1203 laser with a nonlinear external cavity," *Opt. Lett.*, volume 15, pp. 1125–1127, 1989.

[21] I. D. Jung, F. X. Krtner, N. Matuschek, D. H. Sutter, F. Morier-Genoud, G. Zhang, U. Keller, V. Scheuer, M. Tilsch and T. Tschudi, "Self-starting 6.5-fs pulses f rom a Tisapphire laser," *Opt. Lett.*, volume 22, pp. 1009–1011, 1997.

[22] U. Morgner, F. X. Krtner, S. H. Cho, Y. Chen, H. A. Haus, J. G. Fujimoto, E. P. Ippen, V. Scheuer, G. Angelow and T. Tschudi, "Sub-two-cycle pulses from a Kerr-lens mode-locked Tisapphire laser," *Opt. Lett.*, volume 24, pp. 411–413, 1999.

[23] P. P. Vasil'ev and A. B. Sergeev, "Generation of bandwidth-limited 2 ps pulses with 100GHz repetition rate from multisegmented injection laser," *Electon. Lett.*, volume 25, pp. 1049–1050, 1989.

[24] M. C. Wu, Y. K. Chen, T. Tanbun-Ek, R. A. Logan, M. A. Chin and G. Raybon, "Transform-limited 1.4ps optical pulses from a monolithic colliding-pulse modelocked quantum well laser," *Appl. Phys. Lett.*, volume 57, pp. 759–761, 1990.

[25] Y. K. Chen, M. C. Wu, T. Tanbun-Ek, R. A. Logan and M. A. Chin, "Subpicosecond monolithic colliding-pulse mode-locked multiple quantum well lasers," *Appl. Phys. Lett.*, volume 58, pp. 1253–1255, 1991.

[26] A. G. Deryagin, D. V. Kuksenkov, V. I. Kuchinskii, E. L. Portnoi and I. Y. Khrushchev, "Generation of 110 GHz train of subpicosecond pulses in 1.535 mm spectral region by passively modelocked InGaAsP/InP laser diodes," *Electon. Lett.*, volume 30, pp. 309–311, 1994.

[27] A. G. Weber, M. Schell, G. Fischbeck and D. Bimberg, "Generation of single femtosecond pulses by hybrid mode locking of a semiconductor laser," *IEEE J. Quantum Elec.*, volume 28, pp. 2220–2228, 1992.

[28] R. Ludwig and A. Ehrhardt, "Turn-key-ready wavelength, repetition rate and pulsewidth-tunable femtosecond hybrid modelocked semiconductor laser," *Electon. Lett.*, volume 32, pp. 1165–1167, 1995.

[29] N. Stelmakh and J. M. Lourtioz, "230 fs, 25 W pulses from conventional mode-locked laser diodes with saturable absorber created by ion implantation," *Electon. Lett.*, volume 29, pp. 160–162, 1993.

[30] P. J. Delfyett, L. T. Florez, N. G. Stoffel, T. J. Gmitter, N. C. Andreadakis, G. A. Alphonse and W. Ceislik, "200-fs optical pulse generation and intracavity pulse evolution in a hybrid mode-locked semiconductor-laser/amplifier system," *Opt. Lett.*, volume 17, pp. 670–672, 1992.

[31] Y. Matsui, M. D. Pelusi and A. Suzuki, "Pulse compression of an actively modelocked diode laser using dispersion in fiber," *IEEE Photon. Tech Lett.*, volume 11, pp. 1217–1219, 1999.

[32] E. P. Ippen, "Principles of Passive Modelocking," *App. Phys. B*, volume 58, pp. 159–170, 1994.

[33] T. F. Krauss, G. Hondromitros, B. Vogele and R. M. D. L. Rue, "Broad spectral bandwidth semiconductor lasers," *Electon. Lett.*, volume 33, p. 1142, 1997.

[34] Y. H. Kao, I. V. Goltser, M. Jiang, M. N. Islam and G. Raybon, "Gain dispersion induced subpicosecond pulse breakup in a fiber and semiconductor laser amplifier combined system," *Appl. Phys. Lett.*, volume 69, pp. 4221–4223, 1996.

[35] A. Azouz, N. Stelmakh, P. Langlois, J. Lourtioz and P. Gavrilovic, "Nonlinear Chirp Compensation in High-Power Broad Sectrum Pulses from Single-Stripe modelocked laser," *IEEE J. Select. Topics Quantum Electron.*, volume 1, pp. 577–582, 1995.

[36] D. Bimberg, N. Kirstaedter, N. N. Ledentsov, Z. I. Alferov, P. S. Kop'ev and V. M. Ustinov, "InGaAs-GaAs quantum dot lasers," *IEEE J. Select. Topics Quantum Electron.*, volume 3, pp. 196–205, 1997.

[37] T. C. Newell, D. J. Bossert, A. Stintz, B. Fuchs, K. J. Malloy and L. F. Lester, "Gain and Linewidth Enhancement Factor in InAs Quantum-Dot Laser Diodes," *IEEE Photon. Tech Lett.*, volume 11, pp. 1527–1529, 1999.

[38] M. G. Thompson, K. T. Tan, C. Marinelli, K. A. Williams, R. V. Penty, I. H. White, M. Kuntz, D. Ouyang, D. Bimberg, V. M. Ustinov, A. E. Zhukov, A. R. Kovsh, N. N. Ledentsov, D. J, Kang and M. G. Blamire, "Transform-limited optical pulses from 18 GHz monolithic modelocked quantum dot lasers operating at $\approx$1.3 μm," *Electon. Lett.*, volume 40, pp. 346–347, 2004.

[39] P. Bhattacharya, S. Ghosh, S. Pradhan, J. Singh, Z. Wu, K. Kim and T. B. Norris, "Carrier Dynamics and High-Speed Modulation of Tunnel Injection InGaAs-GaAs Quantum Dot Lasers," *IEEE J. Quantum Elec.*, volume 39, pp. 952–962, 2003.

[40] F. Futami, Y. Takushima and K. Kikuchi, "Generation of 10Ghz, 200fs Fourier-transform-limited pulse train from modelocked semiconductor laser at 1.55um by pulse compression using dispersion-flattened fibre with normal group-velocity dispersion," *Electon. Lett.*, volume 34, pp. 2129–2130, 1998.

[41] J. R. Karin, R. J. Helkey, D. J. Derickson, R. Nagrajan, D. S. Allin, J. E. Bowers and R. L. Thornton, "Ultrafast dynamics in field-enhanced saturable absorbers," *Appl. Phys. Lett.*, volume 64, pp. 676–678, 1994.

[42] E. L. Delpon, J. L. Oudar, N. Bouch, R. Raj, A. Shen, N. Stelmakh and J. M. Lourtioz, "Ultrafast excitonic saturable absorption in ion-implanted InGaAs/InAlAs multiple quantum wells," *Appl. Phys. Lett.*, volume 72, pp. 759–761, 1998.

[43] V. V. Nikolaev and E. A. Avrutin, "Photocarrier escape time in quantum well light absorbing devices: Effects of electric field and well parameters," *IEEE J. Quantum Elec.*, volume 39, pp. 1653–1660, 2003.

[44] V. V. Nikolaev and E. A. Avrutin, "Quantum well design for monolithic optical devices with gain and absorber sections," *IEEE Photon. Tech Lett.*, volume 16, pp. 24–26, 2004.

[45] A. Garnache, S. Hoogland, A. C. Tropper, I. Sagnes, G. Saint-Girons and J. S. Roberts, "Sub-500-fs soliton-like pulse in a passively mode-locked broadband surface-emitting laser with 100mW average power," *Appl. Phys. Lett.*, volume 80, pp. 3892–9894, 2002.

[46] J. F. Martins-Filho and C. N. Ironside, "Multiple colliding pulse operation of a semiconductor laser," *Appl. Phys. Lett.*, volume 65, pp. 1894–1896, 1994.

[47] R. L. Fork, O. E. Martinez and J. P. Gordon, "Negative dispersion using pairs of prisms," *Opt. Lett.*, volume 9, pp. 150–152, 1984.

[48] E. B. tracy, "Optical Pulse compression with diffraction gratings," *IEEE J. Quantum Elec.*, volume 5, pp. 454–458, 1969.

[49] E. J. Mayer, J. Mobius, A. Eutaneuer, W. W. Ruhle and R. Szipocs, "Ultrabroadband chirped mirrors for femtosecond lasers," *Opt. Lett.*, volume 22, p. 528, 1997.

[50] R. Szipocs, A. Kohazi-Kis, S. Lako, P. Apai, A. P. Kovacs, G. Debell, L. Mott, A. W. Louderback and A. V. T. adn M K Trubetskov, "Negative Dispersion Mirrors for

Dispersion Control in Femtosecond Lasers: chirped dielectric mirrors and multi-cavity Gires Tournois interferometers," *App. Phys. B*, volume 70, pp. S51–S57, 2000.

[51] J. Kuhl, M. Serenyi and E. O. Gobel, "Bandwidth-limited picosecond pulse generation in an actively mode-locked GaAs laser with intracavity chirp compensation," *Opt. Lett.*, volume 12, pp. 334–336, 1987.

[52] "Physics 7810: Ultrafast Optics (Lecture Notes)," Helsinki University of Technology, http://jilawww.colorado.edu/ cundiffs/PHYS7810, 2005.

[53] "Tfy-125.422 Laser Physics: Transients II (Lecture Notes)," Helsinki University of Technology, http://omm.hut.fi/optics/laserfysiikka/2004/contents.shtml, 2004.

[54] G. R. Fowles, *Introduction to Modern Optics*, chapter 5, Dover Publications, Inc., New York, 1989.

[55] Siegmann, *Lasers*, chapter 27, University Science Books, California, 1986.

[56] F. A. Kartner, J. A. der Au and U. Keller, "Modelocking with slow and fast saturable absorbers- what's the difference," *IEEE J. Select. Topics Quantum Electron.*, volume 4, pp. 159–168, 1998.

[57] P. Vasil'ev, *Ultrafast diode lasers*, chapter 1, Artech House, Boston, 1995.

[58] O. Svelto, *Principles of Lasers*, chapter 6, Plenum Press, New York and London, second edition, 1982.

[59] L. A. Coldren and S. W. Corzine, *Diode Lasers and Photonic Integrated Circuits*, chapter 2, John Wiley and Sons, Inc., New York, 1995.

[60] C. Hepburn, "The Britney Speares Guide to Semiconductor Physics," University of Essex, www.britneyspears.ac/lasers.html, 2004.

[61] L. A. Coldren and S. W. Corzine, *Diode Lasers and Photonic Integrated Circuits*, chapter 5, John Wiley and Sons, Inc., New York, 1995.

[62] M. Henini, "Quantum Dot Heterostructures," *Materials Today*, pp. 48–53, 2002.

[63] G. P. Agrawal and N. K. Dutta, *Semiconductor Lasers*, chapter 2, Van Nostrand Reinhold, New York, 2 edition, 1993.

[64] P. McIlroy, A. Kurobe and Y. Uematsu, "Analysis and application of theoretical gain curves to the design of multi quantum-well lasers," *IEEE J. Quantum Elec.*, volume 21, pp. 1958–1963, 1985.

[65] M. Asada, A. Kameyana and Y. Suematsu, "Gain and intervalence band absorption in quantum well lasers," *IEEE J. Quantum Elec.*, volume 20, pp. 745–753, 1984.

[66] M. B. Flynn, *Modelling of monolithic integrated semiconductor diode lasers as wavelength tunable and ultra short pulsed sources*, Ph.D. thesis, University of St Andrews, 2004.

[67] M. P. van Exter, G. Nienhuis and J. P. Woerdman, "Two simple expressions for the spontaneous emission factor β," *Phys. Rev. A*, volume 54, pp. 3553–3558, 1996.

[68] J. L. A. Dubbeldam and B. Krauskopf, "Self-pulsations of lasers with saturable absorber: Dynamics and bifurcations," *Opt. Comm.*, volume 159, pp. 325–338, 1999.

[69] M. Schell, M. Tsuchiya and T. Kamiya, "Chirp and stability of Mode-Locked Semiconductor Lasers," *IEEE J. Quantum Elec.*, volume 32, pp. 1180–1190, 1996.

[70] M. B. Flynn, L. O'Faolain and T. F. Krauss, "An experimental and numerical study of Q-switched modelocking in monolithic semiconductor diode lasers," *IEEE J. Quantum Elec.*, volume 40, pp. 1008–1013, 2004.

[71] J. F. Martins-Filho, E. A. Avrutin, C. N. Ironside and J. S. Roberts, "Monolithic colliding pulse modelocked semicoductor lasers," *IEEE J. Quantum Elec.*, volume 31, pp. 1168–1179, 2003.

[72] D. J. Jones, L. M. Zhang, J. E. Carroll and D. D. Marcenac, "Dynamics of Monolithic Passively Mode-locked Semiconductor Lasers," *IEEE J. Quantum Elec.*, volume 31, pp. 1051–1058, 1995.

[73] S. F. Yu, "Dynamic behaviour of vertical cavity surface emitting lasers," *IEEE J. Quantum Elec.*, volume 32, pp. 1168–1179, 1995.

[74] W. Bogaerts, *Nanophotonic Waveguides and Photonic Crystals in Silicon-on-Insulator*, Ph.D. thesis, University of Ghent, 2004.

[75] A. F. Koenderink and W. L. Vos, "Optical properties of real photonic crystals: anomalous diffuse transmission," *J. Opt. Soc. Amer. B*, volume 22, pp. 1075–1084, 2005.

[76] M. Notomi, A. Shinya, S. Mitsugi, E. Kuramochi and H.-Y. Ryu, "Waveguides, resonators and their coupled elements in photonic crytstal slabs," *Opt. Exp.*, volume 12, pp. 1551–1561, 2004.

[77] M. V. Kotlyar, T. J. Karle, M. D. Settle, L. O'Faolain and T. F. Krauss, "Low loss Photonic Crystal defect waveguides in InP," *Appl. Phys. Lett.*, volume 84, pp. 3588–3590, 2004.

[78] L. Raffaele, R. M. D. L. Rue and T. F. Krauss, "Ultrashort in-plane semiconductor microlasers with high-reflectivity microstructured mirrors," *Opt. Quant. Electron.*, volume 34, pp. 101–111, 2002.

[79] R. H. Stuelen and D. W. Sweeney, "Extreme Ultraviolet Lithography," *IEEE J. Quantum Elec.*, volume 35, pp. 694–699, 1999.

[80] W. Bogaerts, P. Bientsman, D. Taillaert, R. Baets and D. D. Zutter, "Out-of-plane scattering in Photonic crystal slabs," *IEEE Photon. Tech Lett.*, volume 13, pp. 565–567, 2001.

[81] H. Benisty, D. Labailloy, C. Weisbuch, C. J. M. Smith, T. F. Krauss, D. Cassagne, A. Beraud and C. Jouanin, "Radiation losses of waveguide based two-dimensional photonic crystals: Positive role of the substrate," *Appl. Phys. Lett.*, volume 76, pp. 532–534, 2000.

[82] R. Ferrini, D. Leuenberger, M. Mulot, M. Qui, J. Moosburger, M. Kamp, A. Forchel, S. Anand and R. Houdre, "Optical study of two-dimensional InP-based Photonic Crystals by internal light source technique," *IEEE J. Quantum Elec.*, volume 38, pp. 786–799, 2002.

[83] B. P. V. der Gaag and A. Sherer, "Microfabrication below 10nm," *Appl. Phys. Lett.*, volume 56, p. 481, 1990.

[84] P. Rai-Choudhury, *The SPIE handbook of Microlithography, Micromachining and Microfabrication*, chapter 2, SPIE-International Society for Optical Engineering, 1997.

[85] K. A. Lister, B. G. Casey, P. S. Dobson, S. Thoms, D. S. Macintyre, C. D. W. Wilkinson and J. M. R. Weaver, "Pattern Transfer of a 23nm-period grating and sub-15nm dots into CVD diamond," *Micro. Eng.*, volume 73-74, pp. 319–322, 2004.

[86] L. Stevens, R. Jonckheere, E. Froyen, S. Decoutere and D. Lanneer, "Determination of Proximity Correction parameters using the doughnut method," *Micro. Eng.*, volume 5, pp. 141–150, 1986.

[87] M. V. Kotlyar, L. O'Faolain, R. Wilson and T. F. Krauss, "High Aspect Ratio Chemically Assisted Ion Beam Etching (CAIBE) for Photonic Crystals using a High Beam Voltage-Current Ratio," *J. Vac. Sci. B*, volume 22, pp. 1788–1791, 2004.

[88] R. J. Schul and S. J. Pearton, *Handbook of Advanced Plasma Processing Technniques*, chapter 12, Springer-Verlag, Berlin, Germany, 2000.

[89] M. Qiu, "Effective index method for heterostructure-slab-waveguide-based two dimensional photonic crystals," *Appl. Phys. Lett.*, volume 81, pp. 1163–1165, 2002.

[90] D. Yanson, *Generation of Terahertz-modulated optical signals using AlGaAs/GaAs laser diodes*, Ph.D. thesis, Univesity of Glasgow, 2004.

[91] M. V. Kotlyar, L. O'Faolain, A. Krysa and T. F. Krauss, "Electrically tunable multiquantum well InGaAsP-InGaAsP Microphotonic filter," .

[92] A. Vasdekis, "First year report," Technical report, University of St Andrews, 2004.

[93] J. H. Kim, D. H. Lim, K. S. Kim, G. M. Yang, K. Y. Lim and H. J. Lee, "Lateral oxidation of AlxGa1-xAs-GaAs depending on its structure," *Appl. Phys. Lett.*, volume 69, pp. 3357–3359, 1996.

[94] R. Ferrini, B. Lombardet, B. Wild, R. Houdre and G. H. Duan, "Hole depth- and shape induced radiation losses in two-dimensional photonic crystals," *Appl. Phys. Lett.*, volume 82, pp. 1009–1011, 2003.

[95] K. Frojdh, S. Marcinkevicius, U. Olin, C. Silfvenius, B. Stalnacke and G. Landgren, "Interwell carrier transport in multiple quantum well laser structures," *Appl. Phys. Lett.*, volume 69, pp. 3395–3697, 1996.

[96] A. Kurobe, H. Furuyama, S. Naritsuka, Y. Kokubun and N. Nakamura, "Effects of well number, cavity length and facet reflectivity on the reduction of threshold current of GaAs/AlGaAs multiquantum well lasers," *IEEE J. Quantum Elec.*, volume 24, pp. 635–639, 1988.

[97] T. F. Krauss, *Semiconductor Ring Lasers*, Ph.D. thesis, Univesity of Glasgow, 1992.

[98] D. H. Brown, M. B. Flynn, L. O'Faolain and T. F. Krauss, "Coupled Cavity Tunable Semiconductor Diode Lasers Incorporating Multi-Layer Mirrors," .

[99] S. Cran-Mcgreehin, K. Dolakia and T. F. Krauss, "Integrated optical tweezing with Semiconductor lasers," .

[100] This was observed by a colleague, Lijun Wu. In order to remove silica from a sample after CAIBE, RIE had to be used for a much longer time than expected.

[101] J. Daleiden, R. Keifer, S. Klussmann, M. Kunzer, C. Manz, M. Wailher, J. Braunstein and G. Weimann, "Chemically-assisted ion-beam-etching of (AlGa)As/GaAs: Lattice damage and removal by in-situ Cl2 treatment," *Micro. Eng.*, volume 45, pp. 9–14, 1999.

[102] M. V. Kotlyar, *Photonic Crystal waveguides and Tunable filters in InP*, Ph.D. thesis, University of St Andrews, 2005.

[103] K. Djordjev, S. Choi, S. Choi and P. D. Dapkus, "Microdisk tunable resonant filters and switches," *IEEE Photon. Tech Lett.*, volume 14, pp. 828–830, 2002.

[104] P. Sermon, K. Beekman and S. McClatchie, "Low-K dielectrics for future IC fabrication," *Semiconductor Fabtech*, volume 11, p. 247, 1999.

[105] D. P. Mancini, K. A. Gehoski, E. Ainley, K. J. Nordquist, D. J. Resnick, T. C. Bailey, S. V. Sreenivasan, J. G. Ekerdt and C. G. Wilson, "Hydrogen silsesquioxane for direct electron-beam patterning of step and flash imprint lithography templates," *J. Vac. Sci. B*, volume 20, p. 2896, 2002.

[106] M. J. Word, I. Adesida and P. R. Berger, "Nanometer-Period Gratings in Hydrogen Silsequixoane fabricated by electron beam lithography," *J. Vac. Sci. B*, volume 21, p. L12, 2003.

[107] M. J. Loboda and G. A. Toskey, "Understanding hydrogen silsesquioxane-based dielectric film processing," *Solid State Technol.*, volume 41, p. 99, 1998.

[108] H. Liou and J. Pretzer, "Effect of curing temperature on the mechanical properties of hydrogen silsesquioxane thin films," *Thin Solid Films*, volume 335, p. 186, 1998.

[109] C.-C. Yang and W.-C. Chen, "The structures and properties of hydrogen silsequioxane (HSQ) films produced by thermal curing," *J. Mater. Chem.*, volume 12, p. 1138, 2002.

[110] A. V. Andreev, A. V. Balakin, I. A. Ozheredov, A. P. Shkurinov, P. Masselin, G. Mouret and D. Boucher, "Compression of femtosecond laser pulses in thin one-dimensional photonic crystals," *Phys. Rev. E*, volume 63, pp. 016602–1, 2000.

[111] C. Schuller, F. Klopf, J. P. Reithmaier, M. Kamp and A. Forchel, "Tunable photonic crystals fabricated in III-V semiconductor slab waveguides using infiltrated liquid crystals," *Appl. Phys. Lett.*, volume 82, pp. 2767–2769, 2003.

[112] Q. Chen, E. H. Sargent, N. Leclerc and A.-J. Attias, "Ultrafast nonresonant third-order optical nonlinearity of a conjugated 3,3'-bipyridine derivative from 1150 to 1600 nm," *Appl. Phys. Lett.*, volume 82, pp. 4420–4423, 2003.

[113] S. Sanders, L. Eng, J. Paslaski and A. Yariv, "108 GHz passive mode locking of a multiple quantum well semiconductor laser with an intracavity absorber," *Appl. Phys. Lett.*, volume 56, pp. 310–312, 1989.

[114] R. Paschotta and U. Keller, "Passive Modelocking with slow saturable absorbers," *App. Phys. B*, volume 73, pp. 653–662, 2001.

[115] P. N. Kean, *Generation and Nonlinear Propagation of Ultrashort Near Infrared Pulses, chap 3*, Ph.D. thesis, University of St Andrews, 1989.

[116] R. A. Salvatore and A. Yariv, "Demonstration of Down-Chirped and Chirp-Free Pulses from High-Repetition Rate Passively Mode-Locked Lasers," *IEEE Photon. Tech Lett.*, volume 7, pp. 1151–1153, 1995.

[117] D. O. Brien, *Sensitivity of Quantum Dot lasers to optical feedback*, Ph.D. thesis, University College Cork, 2004.

[118] P. Pottier and R. M. D. L. Rue, "One dimensional photonic crystals in rib waveguide structures for pulse compression," in "Quantum Electronics and Photonics 15, Glasgow," 2001.

[119] F. Gires and P. Tournois, "An interferometer useful for pulse compression of a frequency modulated light pulse," *C. R. Acad. Sci.*, volume 258, pp. 6112–6115, 1964.

[120] L. Orsila, *Interferometric Dielectric Reflectors for Dispersion Compensation in Fibre Lasers*, Master's thesis, Tampere University of Technology, 2003.

[121] P. Tournois, "Negative Group Delay Times in Frustrated GiresTournois and FabryPerot Interferometers," *IEEE J. Quantum Elec.*, volume 33, pp. 519–526, 1997.

[122] J. L. Shen, C. Y. Chang, P. N. Chen, W. C. Chou, Y. F. Chen and M. C. Wu, "Optical absorption studies in absorbing Bragg reflectors," *Opt. Comm.*, volume 19, pp. 155–159, 2001.

[123] D. J. Derickson, R. J. Helkey, A. Mar, J. R. Karin, J. G. Wasserbauer and J. E. Bowers, "Short Pulse Generation Using Multisegment Mode-Locked Semiconductor Lasers," *IEEE J. Quantum Elec.*, volume 28, pp. 2186–2202, 1992.

[124] I. G. Cormack, *Rapid Techniques for ultrashort optical pulse characteristion*, Ph.D. thesis, University of St Andrews, 2001.

[125] K. A. Williams, M. G. Thompson and I. H. White, "Long-wavelength monolithic mode-locked diode lasers," *New Journal of Physics*, volume 6, p. 179, 2004.

[126] Conversations with Mark Thompson.

[127] P. Tian and W. S. Warren, "Ultrafast measurement of two-photon absorption by loss modulation,," *Opt. Lett.*, volume 27, pp. 1634–1636, 2002.

[128] L. A. Coldren and S. W. Corzine, *Diode Lasers and Photonic Integrated Circuits*, chapter 4, John Wiley and Sons, Inc., New York, 1995.

[129] T. F. Krauss, M. V. Kotlyar, L. O'Faolain, R. Wilson, M. Settle, T. Karle, A. Bristow, M. Fox and M. Skolnick, "Functional photonic crystal waveguides and lattices," in "PECS," volume 5, 2004.

[130] L. Pang, W. Nakagawa and Y. hu Fainman, "Fabricatin of optical structures using SU-8 photresist and chemically assisted ion beam etching," *Opt. Eng.*, volume 42, pp. 2912–2917, 2003.

[131] P. Bientsman, S. Assera, S. G. Johnson, J. D. Joannapoulos, G. S. Petrich and L. A. Kolodziejski, "Taper Structures for coupling into photonic crystal slab waveguides," *J. Opt. Soc. Amer. B*, volume 20, pp. 1817–1821, 2003.

[132] D. Ouyang, N. N. Ledentsov, D. Bimberg, A. R. Kovsh, A. E. Zhukov, S. S. Mikhrin and V. M. Ustinov, "High Performance narrow stripe quantum-dot lasers with etched waveguide," *Semicond. Sci. Technol.*, volume 18, pp. L53–L54, 2003.

[133] S. Moore, L. O'Faolain, M. A. Cataluna, M. V. Kotlyar and T. F. Krauss, "Sidewall recombination in Quantum dot lasers," .

[134] M. Kuntz, G. Fiol, M. Lammlin, D. Bimberg, M. G. Thompson, K. T. Tan, C. Marinelli, R. V. Penty, I. H. White, V. M. Ustinov, A. E. Zhukov, Y. M. Shernyakov and A. R. Kovsh, "35 GHz mode-locking of 1.3μm quantum dot lasers," *Appl. Phys. Lett.*, volume 85, pp. 843–846, 2004.

[135] T. J. Karle, D. H. Brown, M. Steer and T. F. Krauss, "Planar Photonic Crystal Coupled Cavity Waveguides," *IEEE J. Select. Topics Quantum Electron.*, volume 8, pp. 909–918, 2002.

[136] S. K. Sharma, Goel, S. A. Rezan, V. N. Miska and K. N. Tripathi, "Third order nonlinear polymer material for photonics," *J. Mat. Sci. Lett.*, volume 22, pp. 737–738, 2003.

[137] B. I. Greene, J. Orenstein, R. R. Millard and L. R. Williams, "Nonlinear Optical Response of Excitons confined to One Dimension,," *Phys. Rev. Lett.*, volume 58, p. 2750, 1987.

[138] M. B. Marques, G. Assanto, G. I. Stegeman, G. R. Mohlmannn, E. W. P. Erdhuisen and W. H. G. Horsthuis, "Large nonresont intensity dependent refractive index of 4-dialkylamino-4'-nitro-diphenyl-polyene side chain polymers in waveguides," *Appl. Phys. Lett.*, volume 58, pp. 2613–2615, 1991.

[139] A. Galvan-Gonzalez, K. D. Belfeld, G. I. Stegeman, M. Canva, S. Marder, S. Thayumanavan, K. Staub, G. Levina and R. J. Twieg, "Photodegradation of selected $\pi-$conjugated electro-optic chromophores," *J. App. Phys.*, volume 94, pp. 756–763, 2003.

[140] D. Feldman, "Polymer Weathering: Photo-Oxidation," *J. Polym. Environ.*, volume 10, pp. 163–172, 2002.

[141] M. J. Weber, *Handbook of Optical materials*, CRC Press LLC, 2003.

[142] D. Nikogsyan, *Handbook of Nonlinear optical crystals*, Springer-Verlag, New York, 1999.

[143] M. Scalora, R. J. Flynn, S. B. Reinhardt, R. L. Fork, M. J. Bloemer, M. D. Tocci, C. M. Bowden, H. S. Ledbetter and J. M. Bendickson, "Ultrashort propagation at the photonic band edge: Large tunable delay with minimal distortion and loss,," *Phys. Rev. E*, volume 54, pp. R1078–1081, 1996.

[144] D. Y. Jeong, Y. H. Ye and Q. M. Zhang, "Effective optical properties associated with wave propagation in photonic crystals of finite length along the propagation direction," *IEEE J. Quantum Elec.*, volume 92, pp. 4194–4200, 2002.

[145] J. L. Shen, T. Jung, S. Murthy, T. Chau, M. C. Wu, D. T. K. Tong, Y. H. Lo, C. L. Chua and Z. H. Zhu, "Modelocking of external-cavity semiconductor lasers with saturable Bragg reflectors," *J. Opt. Soc. Amer. B*, volume 16, pp. 1064–1067, 1999.